NASA
Technical
Paper
2326

September 1984

NASA-TP-2326 19840024324

Minimum-Fuel, Three-Dimensional Flightpath Guidance of Transport Jets

F. Neuman and
E. Kreindler

NASA

NASA Technical Paper 2326

1984

Minimum-Fuel, Three-Dimensional Flightpath Guidance of Transport Jets

F. Neuman
Ames Research Center
Moffett Field, California

E. Kreindler
Israel Institute of Technology
Haifa, Israel

National Aeronautics and Space Administration

Scientific and Technical Information Branch

TABLE OF CONTENTS

SYMBOLS

Since partial derivatives are used for many functions, the functional dependence on state and control variables is indicated in parentheses.

The mathematical notation for division "/" follows FORTRAN convention. Unless "/" is followed by "(" only the next term is the divisor. In the equations, angles are in radians. For ease of reading, angles are given in degrees in the figures.

$A_X,\ldots,H_X(h,v)$	coefficients for simplifying the expression for λ_v and λ_ψ
$A_H,\ldots,Q_H(h,v)$	coefficients for simplifying the expression for γ
$A(h,v)$	coefficient for simplifying the expression for η
C	cruise cost = fuel/unit distance at optimal cruise speed and altitude
$C_j(h,v)$, C_k	coefficients to calculate fuel flow rate, j = 0, 2, k = 1, 12
$D(h,v,u)$	aircraft drag, lb
$D_1(h,v)$	drag for nonturning flight, lb
$D_2(h,v)$	Bank angle induced drag, lb
$F(h,v)$	fuel flow rate, lb/sec
F_T	total fuel used, lb
F_v, D_u, H_T	$\partial H/\partial T$, etc.; subscripts v, u, T, etc. denote partial derivatives of the Hamiltonian, fuel flow, and drag, with respect to the variable in the subscript
$f(t)$	derivative of the state vector $f^T = [\dot{x},\dot{y},\dot{h},\dot{\psi},\dot{v}]$
g	gravitational constant, ft/sec^2
h	vertical Cartesian coordinate, altitude above sea level, ft
$H(h,v,u,T,\gamma)$	Hamiltonian
$J(F,t)$	performance index
k_j	coefficients to calculate drag j = 1, 6
L	lift, lb
M	mixed state variable and control constraint
P	integrant of the performance index
q	constant needed to convert indicated to true airspeed in $v = v_I(1 + qh)$, 1/ft

R	total flightpath length (see fig. 1)
$R_{CRUISE}, R_{CLIMB}, R_{DESCENT}$	flightpath distances above 10,000-ft altitude, ft
S	distance along the horizontal projection of the flightpath
S	state variable constraint
T	thrust (control variable), lb
t_j	integration times $j = 1, 2, 3, 4$
$U(t)$	control vector
u	$\tan \phi$ = tangent of the bank angle (control variable)
v	true airspeed, also ground speed in no wind condition, ft/sec
v_I	indicated airspeed, ft/sec
W	aircraft weight, assumed constant for each subproblem, lb
$X(t)$	state variable vector
x,y	horizontal Cartesian coordinates of the flightpath, ft
γ	flightpath angle (control variable), rad
Δ	difference between two quantities
η	influence factor to append state constraint to the Hamiltonian
$[\lambda_x, \lambda_y, \lambda_h, \lambda_\psi, \lambda_v]$	row vector of adjoint variables consisting of individual adjoint variables
μ	influence factor to append mixed control and state constraint to the Hamiltonian
$\nu(h,v,\lambda_\psi,\lambda_v)$	extremal u when not at maximum or minimum bank angle
$\tau(h,v,\lambda_v)$	extremal thrust when not maximum or minimum
ϕ	bank angle, rad
ψ	heading measured from x-axis, rad
$(\dot{})$	time derivative of ( )
$(\ddot{})$	second time derivative of ( )
$( )^T$	transpose of a vector or matrix

Subscripts:

max	maximum value
min	minimum value

Superscript:

$( )^*$	optimal value; also denotes new expression used in section 3 when derived from an expression given in section 2

MINIMUM-FUEL, THREE-DIMENSIONAL FLIGHTPATH GUIDANCE OF JET TRANSPORTS

F. Neuman and E. Kreindler*

Ames Research Center

SUMMARY

This is a report on minimum-fuel, three-dimensional flightpaths for commercial jet aircraft. The theoretical development is divided into two sections. In both sections, the necessary conditions of optimal control, including singular arcs and state constraints, are used. One section treats the initial and final portions (below 10,000 ft) of long optimal flightpaths. Here all possible paths can be derived by generating fields of extremals. Another section treats the complete intermediate-length, three-dimensional terminal-area flightpaths. Here only representative sample flightpaths can be computed. The report provides sufficient detail to give the student of optimal control a complex example of a useful application of optimal control theory.

1. INTRODUCTION

Rising fuel costs have focused increasing attention on the problem of minimizing fuel consumption of commercial aircraft, and recent work in aircraft guidance demonstrates that on-board optimization of aircraft trajectories offers an efficient way of conserving fuel.

Minimum-fuel aircraft trajectory problems can be divided into two classes: en route problems with trajectory lengths of 50 n. mi. and longer, and terminal-area problems with trajectory lengths of 5 to 50 n. mi. For the en route problem, an on-board algorithm for optimum climb-cruise-descent has been developed for the vertical plane only, since horizontal maneuvers are not a significant feature of en route flight. The general class of terminal-area trajectory problems is more difficult to solve, because vertical and horizontal maneuvers involving speed, altitude, and heading changes, which are of comparable significance in influencing fuel consumption, occur simultaneously.

In section 2 we study the subclass of terminal-area climb-out and descent trajectories that are part of an overall optimal trajectory that includes an en route nonturning optimal cruise segment. The trajectories complete the optimal trajectory problem of reference 1 for longer flightpaths between airports by including the initial and final turns from and to runway headings. For this subclass of problems, essentially all possible extremals can be found, and the problem of global optimality (ref. 2) encountered in the general class of terminal-area turning flightpaths can be avoided.

The results presented for the problem in section 2 show that for fuel-efficient turning climb-out and descent guidance, the altitude-speed profile is nearly the

---

*Department of Electrical Engineering, Israel Institute of Technology, Haifa, Israel.

same as that generated for nonturning flightpaths (i.e., flightpaths confined to the vertical plane). In the special case of nonturning flightpaths, the results presented in this paper are in agreement with those presented in reference 1. The material presented in section 2 of this report was previously published as an informal NASA technical memorandum (ref. 3) (printed locally) and was summarized in reference 4; however, many editorial corrections and changes have since been made and are incorporated here.

Section 3 focuses on the second subclass of problems, namely, 15-50 n. mi.-long terminal-area flightpaths, which are called optimal capture trajectories. These are trajectories that end by aligning the aircraft with the Instrument Landing System (ILS) localizer at a specific point, heading, and speed; they begin at any other point heading and speed. These trajectories arise between airports in metropolitan areas and in the descent phase when the aircraft does not arrive in the terminal area at the proper state to complete the optimal approach or, for air-traffic control reasons, is not permitted to complete the optimal maneuver. The approach in previous studies has been to synthesize and sometimes optimize vertical (ref. 1) and horizontal trajectories (refs. 5-8) separately and then combine them heuristically (refs. 9-11). In this research we generate extremals to study samples of optimal three-dimensional capture trajectories, which include speed changes, and thus verify and refine existing heuristic solutions. The material in section 3 has not been published elsewhere.

We will briefly describe the approach taken for both sections 2 and 3. The first choice to be made was the set of differential equations, to describe the aircraft motion. Point-mass equations of motion were chosen, and a set of controls was selected that is not directly identified with physical aircraft controls. The controls are bank angle, thrust, and flightpath angle, instead of the elevator, rudder, and throttle lever position. In addition, one of the controls, thrust, is difficult to measure in flight. However, we could fly the computed speed-altitude profile, while selecting the speed by an autothrottle, which would result in the proper thrust setting. In addition to the autothrottle, the guidance system needs a flightpath-angle control system and an attitude control system. A more detailed system description would require a more complicated theory.

The aircraft drag as a function of speed and altitude appears in the equations of motion. For meaningful results, the drag must be modeled accurately as a polynomial in altitude, speed, and bank angle. The derivation of this polynomial is given in appendix A.

The performance criterion (minimum fuel) depends on the fuel flow, which must also be modeled accurately for significant results. The fuel flow has been modeled as a function of altitude, speed, and thrust and is also given in appendix A.

The approach for finding optimal flightpaths is as follows. We use the necessary conditions of conventional optimal control theory, which involve the Hamiltonian, adjoint variables, and optimal controls (which are functions of the state and adjoint variables). Extremal paths, which are candidates for optimal paths since they satisfy the necessary conditions, are found by integrating the equations of motion, and the equations for the adjoint variables, while using the optimal controls. Correctness of the computations is verified by checking the Hamiltonian for the problem, which must be zero. The mathematical development is given in sufficient detail so that only knowledge of partial differentiation and algebraic manipulation is needed to derive the equations from the fundamental equations of optimality. However, not all the intermediate steps are shown, and a substantial amount of algebra is often

needed to derive the equations. It is assumed that the reader understands the fundamental equations, such as the necessary conditions of optimality.

The simplified equations of motion contain the flightpath angle control as a linear variable, which results in an optimum flightpath angle; the flightpath angle is either at maximum or minimum. Intermediate values of a linear control may be optimal; the control is then called a singular control in the theory of optimal control (ref. 12). The singular control, the flightpath angle in our case, is found by setting the partial derivative of the Hamiltonian with respect to the control equal to zero, and by setting all the time-derivatives of that partial derivative equal to zero also. The resulting extremal is called a singular arc, and the flightpath-angle control on this arc is smoothly varying with the exception of a few steps. In addition, for the singular-arc solution, the values of the adjoint variables are severely restricted. Only one adjoint variable can be chosen, and it determines the amount of turning of the flightpath. Therefore, if we start an extremal on the singular arc, integrate forward and backward in time, and get off the singular arc at both ends to continue with the ordinary optimal control solution, we can obtain useful sample trajectories.

It will be noted that we can generate useful sample trajectories, but that we do not solve two-point boundary-value problems. Therefore, we cannot use this method in flight, but we can generate a large set of representative flightpaths, and we can compare the resulting fuel used with that of an equivalent suboptimal flightpath, generated by an algorithm that does solve the two-point boundary-value problem. This gives a measure of the penalty for flying with a suboptimal algorithm. Such comparison is the major advantage of the approach taken in the present report. By writing suboptimal algorithms of various complexity and comparing their performance with the optimal, we can determine which features of the optimal trajectories contribute most to fuel savings. A suboptimal algorithm is described in appendix B. It was developed by abstracting the essential features from the optimal trajectory samples found by the methods described in this report.

In general, extremals are only candidates for optimality. The question of global optimality has been avoided by taking advantage of knowledge gained in our earlier work, reported in references 2 and 8. Only medium-length and long-distance trajectories were investigated, where, for global optimality, turns are limited to 180°. Although we cannot prove that our extremal trajectories are globally optimal, our experience leads us to believe that they are.

2. MINIMUM-FUEL TURNING CLIMB-OUT AND DESCENT

Problem Statement

The problem is to minimize fuel consumption F_T over the complete flightpath from takeoff to touchdown. In order to solve this problem, the equations of motion for the vehicle are needed and the performance index must be formulated.

The state equations are the point-mass equations of motion for an aircraft in zero wind condition. The assumptions are as follows: lift = weight/cos ϕ; small flightpath angle; constant mass; and coordinated turns. The equations are a set of nonlinear differential equations of the form $\dot{x} = f(X(t),U(t),t)$, where $X(t)$ is a

column vector of the five states, and U(t) is a column vector of the three controls (ref. 12, p. 48):

$$\dot{x} = v \cos \psi \tag{1}$$

$$\dot{y} = v \sin \psi \tag{2}$$

$$\dot{h} = v\gamma \tag{3}$$

$$\dot{\psi} = -gu/v \tag{4}$$

$$\dot{v} = g(T - D - W\gamma)/W \tag{5}$$

Here the states X(t) are x and y the coordinates in the horizontal plane, h the vertical coordinate, ψ the heading angle measured counterclockwise from the x-axis, and v the speed; g is the gravitational constant, W is the weight, and D is the drag. The controls U(t) are the thrust T, flightpath angle γ, and the tangent of the bank angle u.

The thrust T, where thrust is constrained to be between idle and maximum allowable thrust is

$$T_{idle} \leq T \leq T_{max}$$

where $T_{idle} = 0$ and $T_{max} = 23{,}000$ lb.

The flightpath angle γ, which is constrained in accordance with present commercial airline practice, is

$$\gamma_{min} \leq \gamma \leq \gamma_{max}$$

$$\gamma_{min} = 0°, \ \gamma_{max} = 5° \quad \text{for climb-out}$$

$$\gamma_{min} = -4°, \ \gamma_{max} = 0° \quad \text{for descent}$$

The 0° bounds are imposed to eliminate optimal climb-out and descent flightpaths that dip below h = 2,000 ft. The 5° bounds are imposed to eliminate flightpaths that decelerate during climb at maximum thrust, and the -4° bounds are imposed to eliminate flightpaths that accelerate during descent. The altitude limit of 2,000 ft allows for obstacle clearance in climb-outs and glide-slope alignment on descent.

The tangent of the bank angle u, which is constrained in accordance with present practice for commercial autopilots, is

$$-u_m \leq u \leq u_m \qquad u_m = \tan \phi_{max}, \ \phi_{max} = 30°$$

The only state constraint that was applied was on airspeed. FAA regulations state that the indicated airspeed in the terminal area must not exceed $v_I = 250$ knots (422 ft/sec); when converted into true airspeed (which is equal to the ground speed in the assumed no-wind condition) this translates into a state-variable constraint for the speed v:

$$S = v - v_I(1 + qh) \leq 0 \; ; \qquad v_I = 422 \text{ ft/sec} \; ; \qquad q = 0.162 \times 10^{-4} \text{ ft}^{-1} \qquad (6)$$

For our altitude range from 2,000 to 10,000 ft this corresponds to a true airspeed range from 258.1 to 290.5 knots, respectively.

The next problem is to develop the performance index for the low-altitude turning segment. This requires some preliminary discussion of various approximations. The intended procedure for the complete minimal-fuel turning flightpath is to connect the optimal solution for the straight-line flightpath from reference 1 (cut off below an altitude of 10,000 ft) with an optimal turning climb-out and descent (connected to the straight-line path at the 10,000-ft altitude). Clearly, any portion of an optimal trajectory is also optimal. However, the converse of piecing together portions of optimal trajectories will result in an optimal trajectory only under rather special conditions. But this piecing is precisely what we intend to do. Our experience leads us to believe, from the numerical results, that piecing together a nonturning, optimal, high-altitude trajectory with a turning, low-altitude trajectory will give a close approximation of a complete optimal flightpath.

The first approximation is that the high-altitude portion of a long-distance optimal flightpath has a straight line projection in the horizontal plane. In reference 8 it was shown that for optimal horizontal flightpaths that involve initial and final turns, the flightpath does not contain a mathematically straight-line portion. However, even for flightpaths as short as 20 n. mi. there is a center portion of the flightpath that is straight for all practical purposes. Then, for the much longer flightpaths considered here, the assumption of a straight-line horizontal projection of the center portion of the trajectory appears reasonable. If, in addition, the initial portion of the turning descent is also almost a straight line and the speeds and controls at the junction match, so that there is no discontinuity, then one can be reasonably assured that the joining of the path segments will result in a close approximation of a fuel-optimal flightpath.

To develop the performance index, J, it is convenient to refer to figure 1 in which the flightpath has been drawn to include a turning climb-out segment from t_1

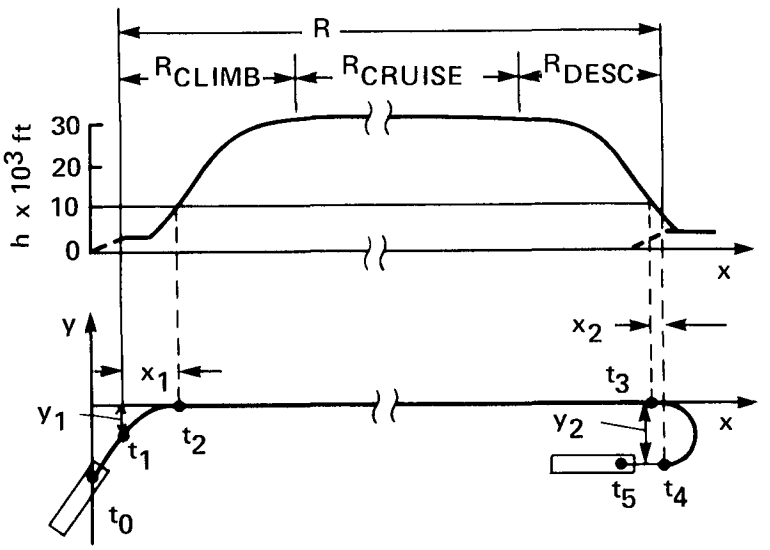

Figure 1.- Optimal flightpath. Note: t_0-t_1 and t_4-t_5 are not subject to optimization.

to 10,000-ft altitude at t_2, a straight-line climbing segment (R_{CLIMB}), from t_2 to cruise altitude, a straight-line cruise segment (R_{CRUISE}), a straight-line descending segment ($R_{DESCENT}$) from cruise altitude to 10,000-ft altitude (t_3), and a turning descent from 10,000-ft altitude to the final approach fix t_4. Therefore, we are concerned here only with optimization of the flightpath above 2,000-ft altitude. Below that altitude other considerations do not permit fuel optimization of the path. For a given range R, the optimal cruise altitude and speed change very little with minor changes in the length of the straight flightpath $R_{CRUISE} + R_{CLIMB} + R_{DESCENT}$ which may occur when considering alternative low-altitude climb-outs and descents. Any change is primarily reflected in the change of the cruise distance, and the high-altitude climb and descent strategies are not affected. This means that the optimal fuel consumed during the nonturning climb-out and descent segments is independent of the rest of the flightpath and can, therefore, be represented by a constant K_1 and the fuel consumed during the cruise segment is directly proportional to the range traveled at cruise altitude; then the total fuel consumed during the flight can be expressed by the equation

$$F_T = \int_{t_1}^{t_2} F\,dt + CR_{CRUISE} + \int_{t_3}^{t_4} F\,dt + K_1 \tag{7}$$

where F is fuel burn rate, C the cruise cost is the fuel per nautical mile expended at optimal cruise speed and altitude (ref. 1), K_1 is the fuel consumed during the optimal straight-line climb and descent segments of flight, and R_{CRUISE} is the distance traveled at cruise. From figure 1 it is seen that

$$R_{CRUISE} = R - R_{CLIMB} - R_{DESCENT} - x_1 - x_2$$

where R (the distance between the climb-out fix and final-approach fix), R_{CLIMB}, and $R_{DESCENT}$ are constants. (Referring to fig. 1, we realize that y_1 and y_2 have negligible effect on the length of the long-distance straight-line flightpath above an altitude of 10,000 ft.) We define x_1 and x_2 to be

$$x_1 = \int_{t_1}^{t_2} v\cos\psi\,dt\ ; \qquad x_2 = \int_{t_3}^{t_4} v\cos\psi\,dt$$

so that

$$F_T = \int_{t_1}^{t_2} (F - Cv\cos\psi)dt + \int_{t_3}^{t_4} (F - Cv\cos\psi)dt + K_1 + K_2$$

where

$$K_2 = C(R - R_{CLIMB} - R_{DESCENT})$$

and we define

$$J = \int_{t_s}^{t_f} (F - Cv\cos\psi)dt = \int_{t_s}^{t_f} P\,dt \tag{8}$$

where $P \triangleq F - Cv \cos \psi$, t_s is t_1 for the climb-out and t_3 for the descent, and t_f is t_2 for the climb-out and t_4 for the descent, and the upper limit of integration is free. The performance index J, applicable to the low-altitude climb/descent portions of the complete flightpath has two parts and equals the fuel expended in the ascent (descent) minus the fuel saved in shortening the cruising portion of the high-altitude flightpath. This, of course, is correct only if the overall flightpath is long enough to have a cruise segment.

The initial and final states for descent are

$$h_o = 10{,}000 \text{ ft}$$

$$\psi_o = 0$$

$$v(0) \leq 250 \text{ knots IAS}$$

$$h_f = 2{,}000 \text{ ft}$$

$$v_f = 180 \text{ knots IAS}$$

and ψ_f is specified between 0 and π. The values are reversed for climbout. The values for (x_1, y_1) and (x_2, y_2) of figure 1 are not specified. The terminal altitude h_f and speed v_f are chosen to permit a final straight-in landing approach along a specified glide slope. The initial speed $v(0)$ is either determined by the speed constraint or, if the speed constraint is not violated, by the speed dictated when flying the solution of the optimization problem. Numerical results show that the low-altitude terminal conditions at 10,000-ft altitude are the proper initial and final conditions for the straight high-altitude en route portion of the flightpath.

In order to solve the minimum-fuel climb-out and descent problems, it is necessary to model the drag, thrust, and fuel-flow rate for a specific aircraft. Choosing the Boeing 727-100 as an example, the drag D is modeled by

$$D = D_1 + D_2 u^2 \tag{9a}$$

where the drag for nonturning flight D_1 is given by

$$D_1 = k_1(1 + k_2 h) + k_3(1 + k_4 h)v^2 + k_5(1 + k_6 h)/v^2 \tag{9b}$$

and the bank-angle-induced drag D_2 is given by

$$D_2 = k_1(1 + k_2 h)/2 + k_5(1 + k_6 h)/v^2 \tag{9c}$$

This approximation for drag results in a minimum drag of 9,000 lb and includes sufficient flap deployment at the lower speeds such that an 8° angle of attack is not exceeded. In general, takeoff and landing weights differ from the nominal W = 150,000 lb. In this case, k_1 is multiplied by (W/150,000) and k_5 by $(W/150{,}000)^2$ to provide a reasonable approximation of the drag.

The thrust value T_{max} was chosen to be 23,000 lb and T_{idle} was set equal to zero. Actually, both the maximum and minimum or idle thrust values are altitude- and speed-dependent. However, the idle thrust is small enough to be negligible, and the maximum allowable thrust has been chosen, for simplicity, as the smallest maximum value allowable over the altitude range of 0 to 10,000 ft.

The fuel-flow rate for the B-727-100 is modeled by

$$F = C_0 + C_1 T + C_2 T^2 \tag{10}$$

where

$$C_j = c_{4j+1}(1 + c_{4j+2}h) + c_{4j+3}(1 + c_{4j+4}h)v \; ; \quad j = 0, 1, 2 \tag{11}$$

and the numerical values of the k's and c's are provided in appendix A.

The optimal cruise fuel used per nautical mile, C, was set equal to 17.5 lb/n. mi., which was obtained from reference 1. This particular C is for the example of a 200 n. mi. flight with a takeoff weight of 150,000 lb. This number will change for other weights and distances. We are interested here only in the character of the optimal turning climb and descent and, therefore, do not change C or W in our computations. However, if optimization of a specific path was required, one would first optimize the straight-line path between airports and obtain C, as well as takeoff and landing weights. This information would be accurate enough to compute the turning terminal-area paths without having to resort to iteration.

Necessary Conditions

The Hamiltonian for this state-variable-constrained problem is (ref. 13)

$$H = P + \lambda^T f + \eta S$$

where λ^T is a row vector of adjoint variables. In this optimal control problem, which only requires the capturing of a specific heading, the state variables x and y in equations (1) and (2) can be ignored (hence we do not have λ_x and λ_y in the Hamiltonian); they are required, of course, for the flight trajectories in the horizontal plane. In the above equation, P is obtained from equations (8) and (10), f from equations (3)-(5), D from equation (9a), and S from equation (6). Then

$$H = C_0 + C_1 T + C_2 T^2 - Cv \cos\psi + \lambda_h v\gamma - \lambda_\psi gu/v + \lambda_v g(T - D_1 - D_2 u^2 - W\gamma)/W + \eta[v - v_I(1 + qh)] \tag{12}$$

where a necessary condition for optimality is $\eta \geq 0$, $\eta[v - v_I(1 + qh)] \equiv 0$. The differential equations that must be integrated to obtain the costate variables are derived from the necessary condition (ref. 12, p. 48)

$$\dot{\lambda}^T = -(\partial H/\partial f)$$

$$\dot{\lambda}_h = -H_h = -C_{0_h} - C_{1_h} T - C_{2_h} T^2 + \lambda_v g(D_{1_h} + D_{2_h} u^2)/W + \eta v_I q \tag{13}$$

$$\dot{\lambda}_\psi = -H_\psi = -Cv \sin\psi \tag{14}$$

$$\dot{\lambda}_v = -H_v = -C_{0_v} - C_{1_v} T - C_{2_v} T^2 + C \cos\psi - \lambda_h \gamma - \lambda_\psi gu/v^2 + \lambda_v g(D_{1_v} + D_{2_v} u^2)/W - \eta \tag{15}$$

where $H_h = \partial H/\partial h$, $C_{0_h} = \partial C_0/\partial h$, etc. (see appendix C). The final time for the integration is not specified. The additional condition that determines the optimal final time t_f is (ref. 12, p. 75) that the Hamiltonian is zero at the final time, $H|_{t=t_f} = 0$. Also, since equation (12) is a Hamiltonian and not an expressed function of time ($H_t = 0$), we have

$$H \equiv 0, \text{ for all } t \in [0,t_f] \tag{16}$$

The necessary conditions for the optimal controls are given by Pontryagin's minimum principle (see ref. 12, p. 108), according to which H must be minimized over the set of all possible constrained controls. Since no cross products of the controls appear in the Hamiltonian, H can be minimized for each of the three controls separately as follows.

First, the extremal thrust T^* is found by finding the value of T that minimizes H, while using the permissible range of T, $T_{idle} \le T \le T_{max}$. That portion of H that is a function of T is denoted as H(T). Then from equation (12)

$$H(T) = C_1 T + C_2 T^2 + \lambda_v g T/W$$

where C_1 and C_2 are greater than zero and are functions of h and v. The function H(T) and the terms of H(T) are plotted in figure 2(a) for the example $\lambda_v < 0$, since otherwise the minimum of H(T) is at T = 0. The unconstrained minimum, if it exists, would occur at $T = \tau$ where $H_T = 0$ and $(H_T)_T > 0$. Two possible cases depending on the value of T_{max} are shown in figure 2(a). If $T_{max} = T_{1max}$ which is smaller than τ, then $T^* = T_{1max}$. If $T_{max} = T_{2max}$ which is larger than τ, then $T^* = \tau$. This is expressed in the following equations:

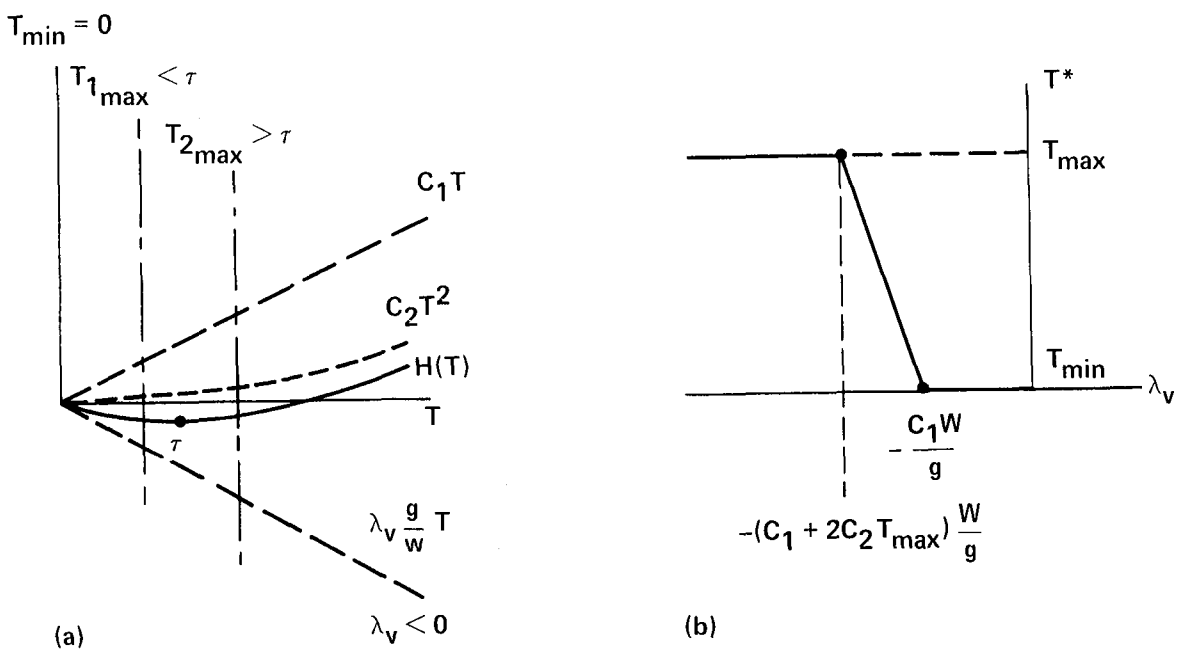

Figure 2.- Optimal thrust. (a) Finding T^* for a specific (h,v); (b) range of λ_v that results in intermediate thrust, T^*.

$$T^* = \begin{cases} T_{max} & \text{if } \tau \geq T_{max} \\ \tau & \text{if } T_{idle} < \tau < T_{max} \\ T_{idle} & \text{if } \tau \leq T_{idle} \end{cases} \tag{17}$$

where from $H_T = 0$

$$\tau = -(C_1 + \lambda_V g/W)/(2C_2) \tag{18}$$

Since minimization of H yields T^* uniquely, it can be seen (see ref. 11) that T^* and λ_V are continuous at junction times between velocity-constrained and the unconstrained arcs. Thus, thrust is seen to be a continuous function of λ_V and t. Solving equation (18) for λ_V and inserting $\tau = 0$ and $\tau = T_{max}$ gives the range of λ_V that results in an intermediate thrust; this is shown in figure 2(b). Since C_2 is small for all h and v, the range of λ_V for intermediate thrust is narrow and, as we shall see in the results section, intermediate thrust will not occur for the optimal turning climb-outs and descents.

Next, the extremal bank-angle control u^* is found by finding the value of u that minimizes H while using the permissible range of u, $-u_m \leq u \leq u_m$. First, however, we observe that equations (4) and (14) imply that

$$u = 0 \quad \text{if} \quad \lambda_\psi = 0 \quad \text{on an interval of time} \tag{19}$$

which results in straight-line flight in the horizontal plane.

That portion of H that is a function of u is denoted as $H(u)$. Then, from equation (12),

$$H(u) = -\lambda_\psi g u/v - \lambda_V g D_2 u^2/W$$

The function $H(u)$ and the terms of $H(u)$ are plotted in figure 3(a) for $\lambda_V < 0$ and $\lambda_\psi > 0$. The unconstrained minimum, $u = \nu$, will occur where $H_u = 0$ and $(H_u)_u > 0$,

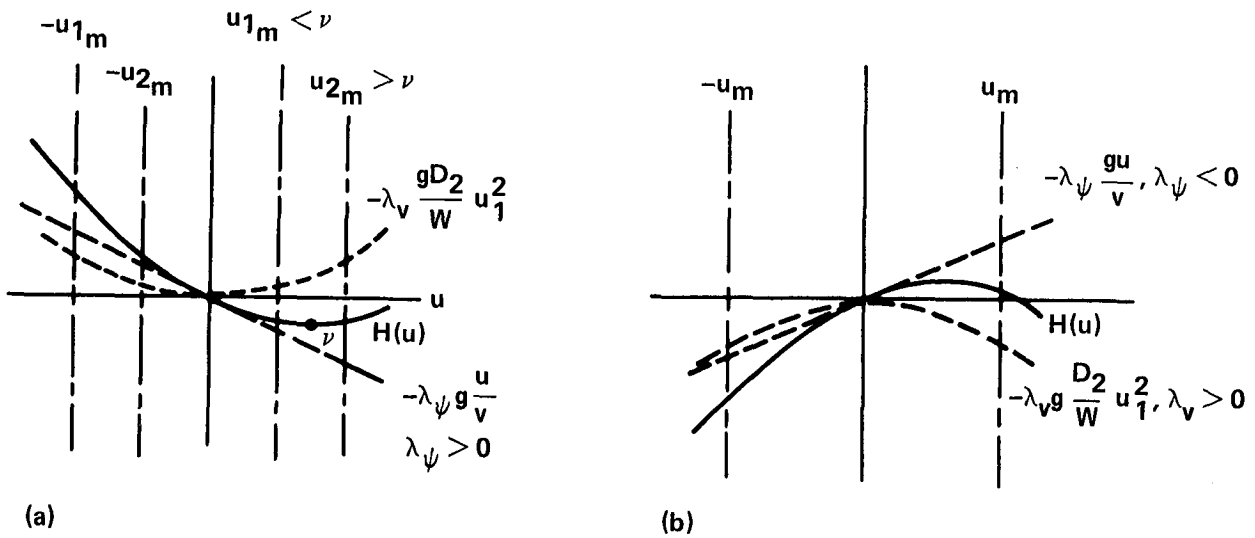

Figure 3.- Finding u^*. (a) $\lambda_V < 0$; (b) $\lambda_V > 0$.

if it exists. Two possible cases of u_m are shown in figure 3(a). In case 1, u_{1m} is smaller than ν, hence $u^* = u_{1m}$. In the second case, u_{2m} is larger than ν, hence $u^* = \nu$.

The case in which $\lambda_v > 0$ and $\lambda_\psi < 0$ is shown in figure 3(b). Here $(H_u)_u < 0$ at $H_u = 0$ for a maximum value, and the minimum value of $H(u)$ is at one of the limits of u, in this case $u^* = -u_m$. The two mirror symmetric cases (not shown $\lambda_v < 0$ and $\lambda_\psi < 0$, and $\lambda_v > 0$ and $\lambda_\psi > 0$, give similar results. In summary,

$$u^* = \left\{ \begin{array}{lll} u_m & \text{if} & \nu \geq u_m \\ \nu & \text{if} & -u_m < \nu < u_m \\ -u_m & \text{if} & \nu \leq -u_m \end{array} \right\} \lambda_v < 0 \tag{20}$$

where from $H_u = 0$

$$\nu = -(\lambda_\psi W)/(2\lambda_v D_2 v) \tag{21}$$

If $\lambda_v \geq 0$, minimization of H gives

$$u^* = u_m \operatorname{sgn} \lambda_\psi \; ; \qquad \lambda_v \geq 0 \quad \text{and} \quad \lambda_\psi \not\equiv 0 \tag{22}$$

We note that in equation (22), λ_ψ is not identically zero on an interval. For $\lambda_\psi \equiv 0$ and $\lambda_v > 0$, minimization of H with respect to u gives $u^* = \pm u_m$; however, this is not compatible with equation (19). This incompatibility results from the nonconvex velocity set (see fig. 30, appendix D). This incompatibility and the nonconvexity can be removed by allowing a so-called "relaxed control," that is, a chattering bank angle $u(t)$, oscillating at infinite frequency between $+u_m$ and $-u_m$. If the average of the chattering $u(t)$ is zero, then it is compatible with $\lambda_\psi \equiv 0$ and ψ = constant; that is, a nonturning flightpath. It is shown in appendix D how, by admitting a chattering control u, the velocity set is made convex. A chattering bank angle on a nonturning flightpath may be called for when maximum drag at zero thrust ($\lambda_v > 0$ implies, by equations (17) and (18), that $T = 0$) is needed for maximum deceleration. This makes no sense for the type of long flightpaths we computed; indeed, in our numerical work, λ_v was always negative and we never got near a chattering bank angle.

We further note that if λ_ψ vanishes on an interval of time ($u \equiv 0$) from equation (19) and λ_v crosses from negative to positive values, say at $t = t_2$, then u switches from $u(t) = 0$, $t < t_2$ to $u(t_2^+) = \pm u_m$, from equation (22) dependent on λ_ψ which is no longer zero. This is a transition from a straight-line flightpath to a curved one. Such discontinuous bank angle would have to occur at zero thrust (see fig. 2(b)); thus, it might occur (but actually did not occur) after initiation of the optimal descent.

Lastly, the extremal flightpath angle γ^* is found by finding the value of γ that minimizes H while using the permissible range of γ, $\gamma_{min} \leq \gamma \leq \gamma_{max}$. That portion of H that is a function of γ is denoted as $H(\gamma)$. Then, from equation (12)

$$H(\gamma) = \lambda_h v\gamma - \lambda_v g\gamma$$

Since $H(\gamma)$ is linear in γ (see fig. 4(a)), γ will be at one of its limits in order to minimize H,

$$\gamma^* = \begin{cases} \gamma_{max} & \text{if } H_\gamma < 0 \\ \gamma_{min} & \text{if } H_\gamma > 0 \end{cases} \tag{23}$$

where

$$H_\gamma = \lambda_h v - \lambda_v g$$

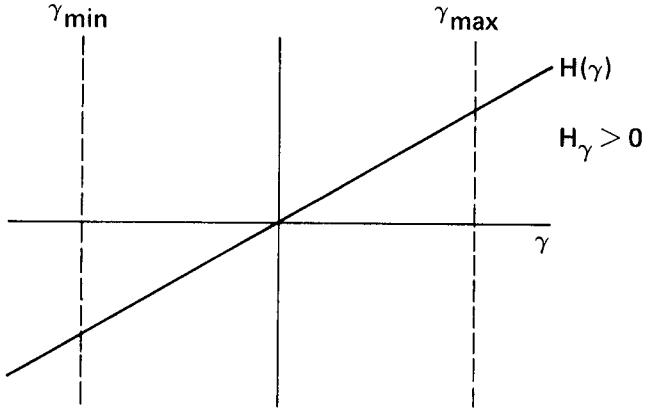

Figure 4.- Finding γ^*.

Since H is linear with respect to γ, a special optimal solution for γ exists, namely, when $H(\gamma) \equiv 0$ for an interval of time. In this case, the relation $H_\gamma = 0$ does not involve γ and, therefore, does not determine γ^*. However, it determines the relationship between λ_h, λ_v, and v:

$$H_\gamma = \lambda_h v - \lambda_v g = 0 \Rightarrow \lambda_h = \lambda_v g/v \quad \text{on a subinterval} \tag{24}$$

In the next section, this relationship, as well as others, will be used to determine a special optimal flightpath angle, which is called the singular solution.

Flightpath Guidance along a Singular Arc

When flying along a singular arc, equation (24) implies that all time-derivatives of H_γ vanish. We start with the first derivative,

$$(\dot{H}_\gamma) = \dot{\lambda}_h v + \lambda_h \dot{v} - \dot{\lambda}_v g = 0 \tag{25a}$$

Inserting the values for $\dot{\lambda}_h$ (eq. (13)), λ_h (eq. (24)), $\dot{v}$ (eq. (5)), and $\dot{\lambda}_v$ (eq. (15)) and simplifying equation (25a) results in

$$(\dot{H}_\gamma) = -F_h v + \lambda_v[D_h v + g(T - D)/v - gD_v]g/W + g(F_v - C\cos\psi + \lambda_\psi g u/v^2) \tag{25b}$$

Solution of the simultaneous equations for $H = 0$ (eq. (12)) and $(\dot{H}_\gamma) = 0$ will permit the calculation of the adjoint variables λ_v and λ_ψ; then λ_h follows from

equation (24). For simplicity, λ_v and λ_ψ will be calculated under the assumption (to be verified) that $T = T_{max}$ for optimal climb-out and $T = T_{idle}$ for optimal descent. There are three cases for u: $u = 0$, $|u| = u_m$ (maximum), and $|u| < u_m$ (intermediate). We then examine the equations numerically to check whether they are consistent with these assumptions (e.g., λ_v must be in the appropriate range for the assumed T, v must be in the speed range of interest, and the λ's must be real numbers).

The singular-arc λ's can now be found as follows. By using equation (24) in the equation for $H = 0$ (eq. (12)) the dependence of equation (12) on γ is eliminated. The additional (temporary) assumption is made that the solution is not bounded by the speed constraint, $\eta = 0$. In addition, by using $H = 0$ and $\dot{H}_\gamma = 0$, we have three equations with three unknowns u, λ_v, and λ_ψ:

$$\left.\begin{aligned} 2H/v &= \lambda_v(A_x + B_x u^2) - \lambda_\psi C_x u + D_x = 0 \\ \dot{H}_\gamma/g - H/v &= \lambda_v(E_x + P_x u^2) + \lambda_\psi C_x u + G_x = 0 \\ u &= H_x \lambda_\psi/\lambda_v \big|_{|u|<u_m} \end{aligned}\right\} \tag{26a}$$

with the following coefficients

$$\left.\begin{aligned} A_x &= 2g(T - D_1)/(vW) \\ B_x &= -2gD_2/(vW) \\ C_x &= 2g/v^2 \\ D_x &= 2F/v - 2C\cos\psi \\ E_x &= D_{1_h} v/W - gD_{1_v}/W \\ P_x &= D_{2_h} v/W - D_{2_v} g/W \\ G_x &= -F/v - F_h v/g + F_v \\ H_x &= -W/(2D_2 v) \end{aligned}\right\} \tag{26b}$$

First case: $-u_m < u < u_m$. Solving equations (26) for λ_v and λ_ψ

$$\lambda_v = [D_x(P_x H_x + C_x) - G_x(B_x H_x - C_x)]/[E_x(B_x H_x - C_x) - A_x(P_x H_x + C_x)] \tag{27}$$

$$\lambda_\psi = \lambda_v \left((G_x A_x - D_x E_x)/\{H_x[D_x(P_x H_x + C_x) - G_x(B_x H_x - C_x)]\}\right)^{1/2} \tag{28}$$

and λ_h follows from equation (24).

Second case: $u = 0$. From equation (19),

$$\lambda_\psi = 0 \tag{29}$$

and equation (26a) becomes

$$\lambda_v A_x + D_x = 0 \tag{30a}$$

$$\lambda_v E_x + G_x = 0 \tag{30b}$$

For (30a) and (30b) to be consistent requires

$$G_x A_x - D_x E_x = 0 \tag{31}$$

This is consistent with equation (28) for $\lambda_\psi = 0$. The variables G_x, A_x, D_x, and E_x are functions of altitude and speed so that we can expect a single altitude-versus-speed profile. If we attempt to obtain an explicit expression for h versus v by expanding equation (31), we encounter an extremely long polynomial in the seventh power of v and second power of h, which is not very illuminating. We therefore shall be satisfied with a numerical solution of equation (31) which is described later. In this case, the altitude-speed profile is the state trajectory and we do not need to solve $\ddot{H}_\gamma = 0$ to determine γ. Instead, by replacing $\dot{h}$ with $\Delta h/\Delta t$ in equation (3) and $\dot{v}$ with $\Delta v/\Delta t$ in equation (5), and by dividing equation (3) by equation (5) and solving for γ, we obtain γ directly

$$\gamma = [(T - D)/W][(\Delta h/\Delta v)/(\Delta h/\Delta v + v/g)] \tag{32}$$

where $\Delta h/\Delta v$ can be determined from the altitude-speed profile.

Third case: $|u| = u_m$. Solving equation (26) for λ_v and λ_ψ with $|u| = u_m$ results in

$$\lambda_v = -(D_x + G_x)/[(A_x + B_x u_m^2) + (E_x + P_x u_m^2)] \tag{33}$$

and

$$\lambda_\psi = [\lambda_v(A_x + B_x u_m^2) + D_x]/(C_x u_m) \tag{34}$$

and λ_h follows from equation (24). This last case is of little interest for optimum ascents and descents, since $u = u_m$ on the singular arc did not occur in our numerical investigation.

It should be noted that for all cases — even though λ_v and λ_ψ can be computed directly from the above equations all along the singular-γ arc — it is computationally simpler to use the above equations to compute initial values only and to integrate equations (15) to obtain λ_v and (14) to obtain λ_ψ, and to use equation (24) to obtain λ_h. This can be done also across junctions of speed-constrained and unconstrained arcs as it is shown in the next subsection that λ_v and λ_ψ are continuous at such junctions.

We now must check whether all constraints and the assumptions on u and T are satisfied so that the singular-arcs are candidates for optimal paths. These checks are made at $h = 10{,}000$ ft, which is used for the start of forward integration in descent and backward integration in climb. At that altitude, the case $u \approx 0$ is of primary interest, since most of the turn is executed at low altitude. From the numerical solution of equation (31), which applies to $u = 0$, λ_v is obtained from equation (30a) or (30b). When this λ_v is substituted into equation (18), it is consistent with $T = T_{max}$ for climb and $T = 0$ for descent. For descent, the solution of equation (31) gives an indicated airspeed below 250 knots, which means that

the speed limit will be inactive. During the climbout, the speed profile along the singular arc is, however, above the speed limit. Thus, climbout on the singular-γ arc violates the speed constraint. Nevertheless this case is investigated, since the speed limit in the terminal area may be relaxed by ATC.

Being assured that the singular-γ case satisfies the constraints and assumptions at high altitude for $u \approx 0$, the singular-arc flightpath angle for intermediate u is now determined. The complete flightpath is determined by the choice of one parameter, e.g., λ_ψ (see p. 18) and the v-h profile can be obtained by a numerical procedure similar to that given for the nonturning flightpath. Then γ can be calculated from the v-h profile via equation (32), and the three-dimensional path can be determined in one additional step. However, we prefer to calculate γ directly from the condition $(\ddot{H}_\gamma) = 0$ which, it turns out, contains γ explicitly. We differentiate (25b) to obtain

$$
\begin{aligned}
0 = (\ddot{H}_\gamma) &= \partial(\dot{H}_\gamma)/\partial t = \partial/\partial t\{-F_h v + \lambda_v[D_h v + g(T - D)/v - gD_v]g/W \\
&\quad + g(F_v - C\cos\psi + \lambda_\psi g u/v^2)\} \\
&= -F_h\dot{v} - \dot{F}_h v + \dot{\lambda}_v[D_h v + g(T - D)/v - gD_v]g/W + \lambda_v[\dot{D}_h v + D_h\dot{v} - g(T - D)\dot{v}/v^2 \\
&\quad - g(D_u\dot{u} + D_h\dot{h} + D_v\dot{v})/v - g\dot{D}_v]g/W + g(\dot{F}_v + C\sin\psi\dot{\psi} + \dot{\lambda}_\psi g u/v^2 \\
&\quad - 2\lambda_\psi g u\dot{v}/v^3 + \lambda_\psi g\dot{u}/v^2)
\end{aligned}
\tag{35}
$$

When the equations for the time-derivatives are inserted in equation (35), γ appears linearly.

Solving equation (35) for γ is straightforward but tedious and will only be sketched out. First, all terms with identical time-derivatives — $\dot{v}$, $\dot{h}$, $\dot{\psi}$, $\dot{\lambda}_v$, $\dot{\lambda}_\psi$, $\dot{u}$, $\dot{F}_v$, $\dot{F}_h$, $\dot{D}_v$, and $\dot{D}_h$ — are combined. Second, the last five time-derivatives are eliminated with expressions (C17), (C3), (C5), (C13), and (C15) from appendix C. This results in the following equation for $(\ddot{H}_\gamma)$:

$$
(\ddot{H}_\gamma) = A_H\dot{v} + B_H\dot{h} + C_H\dot{\psi} + D_H\dot{\lambda}_v + E_H\dot{\lambda}_\psi \tag{36}
$$

where the coefficients have the following values:

$$
\left.
\begin{aligned}
A_H &= -F_h + gD_h\lambda_v/W - g^2\lambda_v(T - D)/(Wv^2) - 2g^2\lambda_\psi u/v^3 - g^2\lambda_v D_v/(Wv) \\
&\quad + Q_H[1 - k_1(1 + k_2 h)/D_2]/v - vF_{vh} + 2gk_3k_4v^2\lambda_v/W - 2gk_5k_6(1 + u^2)\lambda_v/(Wv^2) \\
&\quad - 2g^2k_3(1 + k_4 h)\lambda_v/W - 6\lambda_v g^2k_5(1 + k_6 h)(1 + u^2)/(v^4 W) \\
B_H &= -g^2\lambda_v D_h/(Wv) - Q_H D_{2_h}/D_2 + gF_{vh} - 2g^2k_3k_4v\lambda_v/W + 2g^2k_5k_6(1 + u^2)\lambda_v/(Wv^3) \\
C_H &= gC\sin\psi \\
D_H &= g[D_h v + g(T - D)/v - gD_v]/W - Q_H/\lambda_v
\end{aligned}
\right\} \tag{37}
$$

$$
\left.
\begin{aligned}
E_H &= g^2 u/v^2 + Q_H/\lambda_\psi \\
Q_H &= [g^2\lambda_\psi/v^2 - g^2\lambda_v D_u/(Wv) + (k_1 k_2 v + 2k_5 k_6/v) g\lambda_v u/W \\
&\quad + 4g^2 k_5(1 + k_6 h)u\lambda_v/(Wv^3)]u \ , \qquad |u| < u_m \\
Q_H &= 0 \ , \qquad |u| = u_m
\end{aligned}
\right\} \qquad (37) \text{ (cont.)}
$$

None of the coefficients (eq. (37)) involve γ. When the equations for the time-derivatives are inserted into equation (36), γ appears linearly and the solution for γ is

$$
\begin{aligned}
\gamma = [&A_H g(T - D)/W - C_H g u/v + D_H(-F_v + C\cos\psi - g\lambda_\psi u/v^2 + g\lambda_v D_v/W) \\
&+ E_H(-Cv\sin\psi)]/[A_H g - B_H v + D_H\lambda_h]
\end{aligned} \qquad (38)
$$

For equation (38) to be a candidate for an optimal solution, the generalized Legendre-Clebsch condition must hold:

$$
(-\ddot{H}_\gamma)_\gamma \geq 0 \rightarrow (-\ddot{H}_\gamma)_\gamma = A_H g - B_H v + D_H\lambda_h > 0 \qquad (39)
$$

This condition was verified numerically along all singular arcs. The case $(-\ddot{H}_\gamma)_\gamma = 0$ is not possible since equation (39) is also the denominator for equation (38), which would imply $\gamma \rightarrow \infty$.

On the speed-constraint arc, to be discussed next, $\gamma(t)$ is also intermediate and singular. But now $\eta(t) > 0$, so that an appropriate term with η and $\dot{\eta}$ should be added to $\ddot{H}_\gamma$ and to equation (38) for γ. There is no need to do this, however, since $\gamma(t)$ for the speed-constraint arc is determined by the speed constraint.

Flightpath Guidance along a Speed-Constraint Arc

Since the climb speed for the singular γ was above the speed constraint, we must now develop the equations for γ when flying at the speed-constraint v_I = constant, $\eta > 0$. On the speed constraint, inequality (6) converts to an equality and can be solved for v, and the derivative can be taken in order to express the relationships for v and $\dot{v}$ on the constraint which are needed for the computation of η and γ.

$$
v = v_I(1 + qh) \qquad (40a)
$$

then

$$
\dot{v} = v_I q\dot{h} \qquad (40b)
$$

But from equations (3) and (40a)

$$
\dot{h} = v_I(1 + qh)\gamma \qquad (40c)
$$

which with equation (40b) implies

$$\dot{v} = qv_I^2(1 + qh)\gamma \tag{41}$$

Substituting for $\dot{v}$ equation (5) and solving for γ results in the following expression, which must hold on the speed-constrained arc:

$$\gamma = [(T - D)/W]\{g/[g + v_I^2 q(1 + qh)]\} \tag{42}$$

Here the factor in braces varies only from 0.92 to 0.91 over the altitude range of 0 to 10,000 ft, respectively. It turns out that γ in (42) is intermediate and is the primary control to hold v at the speed-constraint; the thrust T, if it is intermediate, is tied to the speed-constraint via equation (18) and by the multiplier $\eta(t)$ in equation (15) for λ_v.

Since γ is intermediate on the speed-constraint, it is singular. For convenience of designation we differentiate between the "singular arc" where γ is intermediate and the speed constraint is inactive or is ignored, and a portion of the flightpath where the speed constraint is active, which is called a "speed-constraint arc," even though γ is singular.

At a junction time with a speed-constraint arc, the singular $\gamma(t)$ undergoes a jump; this corresponds to the necessary conditions given in reference 14. Also, according to reference 14, there is no jump in the adjoint variables at the junction time. This can be shown in our case as follows. According to reference 13, at the junction time t_i the costates must satisfy the jump condition

$$\Delta\lambda_h(t_i) = -\lambda_h(t_i^+) - \lambda_h(t_i^-) = -\nu_i S_h = \nu_i v_I q$$

$$\Delta\lambda_v(t_i) = \lambda_v(t_i^+) - \lambda_v(t_i^-) = -\nu_i S_v = -\nu_i , \qquad \nu_i \geq 0$$

whence

$$\Delta\lambda_h(t_i)/\Delta\lambda_v(t_i) = -v_I q \tag{43}$$

But since $\gamma(t)$ is singular across t_i we have from equation (24)

$$\frac{\lambda_h(t_i^+)}{\lambda_v(t_i^+)} = \frac{\lambda_h(t_i^-)}{\lambda_v(t_i^-)} = \frac{v}{g}$$

from which it follows that

$$\Delta\lambda_h(t_i)/\Delta\lambda_v(t_i) = v/g$$

which contradicts (43). Hence $\nu_i = 0$ and the λ's are continuous across the junction.

The condition $\eta(t) \geq 0$ must be checked along the speed constraint arc. Furthermore $\eta(t)$ is needed for the computation of λ_h and λ_v in (13) and (15), recpectively. Since γ is singular on the speed-constraint arc, equation (24) must hold. Differentiating (24) gives

$$\dot{\lambda}_h = g(v\dot{\lambda}_v - \lambda_v\dot{v})/v^2 \tag{44}$$

By combining equation (43) with equations (13) and (15), we can obtain an expression for η which is not dependent on $\dot{\lambda}_h$ or $\dot{\lambda}_v$:

$$\eta = \begin{cases} [C_{0_h} + C_{1_h}T + C_{2_h}T^2 - \lambda_v g D_h/W - g(vA_\eta + \lambda_v\dot{v})/v^2]/(v_I q + g/v) \geq 0 \\ 0 \end{cases} \begin{matrix} \} \text{ on the constraint} \\ \} \text{ off the constraint} \end{matrix} \tag{45a}$$

where

$$A_\eta \triangleq C_{0_v} + C_{1_v}T + C_{2_v}T^2 - C\cos\psi + \lambda_h\gamma + \lambda_\psi gu/v^2 - \lambda_v g D_v/W \tag{45b}$$

and where v and $\dot{v}$ are given by equations (40a) and (41), respectively.

Computation of Extremals

The extremals are computed by numerical integration of the state and adjoint equations (1)-(5) and (13)-(15) with the control T given by equations (17) and (18), the control u given by equations (19)-(22), and the control γ given by equation (23) when we are neither on the singular arc nor on the speed constraint; and γ is given by equation (38) on the singular arc or by equation (40) on the speed-constraint arc. On the singular arc, the costate variables λ_v and λ_ψ are obtained by integrating equations (13)-(15) instead of finding them directly from equations (27) and (28); we find λ_h directly from equation (24) for both singular and speed-constrained arcs.

In the climbout and descent cases discussed in section 2, a heading capture with specified altitudes and speeds, the starting values for integration of the adjoint variables can be treated as parameters in such a manner that families of extremals will sweep out all desired headings at the final altitude and speed. To achieve this, forward time-integration is used for descent and reverse time-integration for ascent. This technique permits the path integration to be started at 10,000 ft on a speed-constrained- or a singular-arc portion of the path, which limits the freedom of choice for the initial values of the adjoint variables and makes it easier to pick them. For convenience of integration, the (x,y) coordinates at the 10,000-ft altitude were chosen (0,0). When starting on a singular-arc portion of the path, the optimal path leaves the singular arc when required by the 2,000-ft end altitude conditions, provided the solution is not previously forced off by failing to meet the speed constraint (eq. (6)) or the generalized Legendre-Clebsch condition (39)). When starting on a speed-constrained portion of the path, the optimal solution will leave the constraint boundary as required by the 2,000-ft end altitude conditions, provided the solution is not forced off by failing to meet $\eta > 0$. If in the singular-arc descent the speed constraint is violated before reaching the reference altitude of 2,000 ft, the guidance switches to the speed-constrained arc at this point. The singular case and the speed-limited case starting values are discussed separately.

Starting values for the singular arc— To calculate an extremal, we must know the starting values of all states and adjoint variables, x, y, h, ψ, v, λ_h, λ_ψ, and λ_v, which when known also define the controls. As stated before, the first four starting

states for integration are given as $x = 0$, $y = 0$, $h = 10{,}000$, $\psi = 0$, but v is unknown. To find v, we make use of the fact that the control u must be close to zero at the 10,000-ft level, where the nonturning, high-altitude path begins. Therefore, we choose v iteratively to solve equation (31), which is the condition for singular γ when $u = 0$. Small variation from the speed thus found will permit us to find λ_v and λ_ψ from equations (27) and (28) and λ_h from equation (24) which when used to obtain extremals, cover the range of end-heading $0 < \psi < 180°$. Changes in v to cover the range of headings were so slight (of the order of 10^{-19} knots) that double-precision calculations were required. Once this was known, for practical purposes, we used a fixed starting v as determined from equation (31) and λ_v from equation (30a), and then selected λ_ψ over a small range close to zero to cover all turns (0°-180°). This starting speed was 331 knots for the climb and 275 knots for the descent. For the climb, this is above the speed constraint of 290 knots (250 knots IAS); thus, backward integration of the climb can start either on the singular arc, if we allow speeds above the speed constraint, or on the speed-constraint arc. For the descent it follows that the forward integration cannot start on the speed-constraint arc.

Starting values for the speed-constraint arc— In the speed-limited case, we know all initial states, even $v = v_I$. We must, therefore, only determine the starting adjoint variables λ_v, λ_h, and λ_ψ. Using equation (16) with λ_h given by equation (24), the unsaturated u by equation (21), and γ by equation (42), we obtain

$$\lambda_\psi = \pm 2v\{-[C_0 + C_1T + C_2T^2 - Cv + \lambda_v g(T - D_1)/W]\lambda_v D_2/(gW)\}^{1/2}, \qquad |u| < u_m \tag{46}$$

Here, λ_v is a parameter and, thus the choice of one adjoint variable, λ_v, determines the other two, once the thrust is chosen ($T = 0$ or $T = T_{max}$). As before, initially u, and hence λ_ψ, must be extremely close to zero. Hence, from equation (46), λ_v must be close to

$$\lambda_v\big|_{\lambda_\psi = 0} = -(C_0 + C_1T + C_2T^2 - Cv)W/[g(T - D_1)] \tag{47}$$

Now, from equations (18) and (20), we get the lower and upper bounds of λ_v, respectively; thus λ_v must be in the range

$$-WC_1/g \le \lambda_v \le 0 \quad \text{for} \quad T = 0 \tag{48}$$

and from equation (18),

$$\lambda_v \le -(C_1 + 2C_2T_{max})W/g \quad \text{for} \quad T = T_{max} \tag{49}$$

The above considerations limit the possible values of λ_v that can be considered when starting on the speed constraint, and equation (47) must fall within these limits.

Numerical solutions of equations (47)-(49) confirm that at 10,000 ft, starting the forward or backward integration at the speed constraint is optimal for climb-out but not for descent. When we insert the values from equation (26b) for A_x and D_x and solve for λ_v, we obtain an expression identical to equation (47) for the speed-limited case. We note, therefore, that at the transition from the singular arc to the speed-limited arc, λ_v and λ_h are continuous. Therefore, after the starting value is known, λ_v can be computed in both cases by integrating equation (15).

3. MINIMUM-FUEL CAPTURE FLIGHTPATHS IN THE TERMINAL AREA

Problem Statement and Necessary Conditions

The problem is to find minimum-fuel, intermediate-length capture flightpaths after arrival in the terminal area. Intermediate-length capture flightpaths are those flightpaths that start from an arbitrary position, altitude, and heading in the terminal area, that have a central essentially nonturning segment, and that end on the centerline extension of the approach runway with the proper final heading, altitude, and speed (see fig. 5). This would mean that we would have to solve a two-point boundary-value problem. However, in accordance with the methods established in reference 8, we do not seek to solve the two-point boundary-value problem. We only generate a set of representative samples, from which we can deduce the essential features for suboptimal approximations. More complex, highly turning, short distance paths can easily be generated from the equations, but they were not studied, since operationally they do not occur frequently. However, it has been shown in reference 8 that short, suboptimal paths that meet the two-point boundary-value problem can always be generated, but at a cost substantially above optimal.

The equations of motion are the same as in section 2 (eqs. (1)-(5)). Also, the controls and the limits on the controls are the same. In section 3 the speed constraint equation (6) is also considered, even though the speed-constrained flightpaths have a very narrow range of speeds. Most of the results are, therefore, given for unconstrained paths. The performance index is the integral of the fuel-flow rate

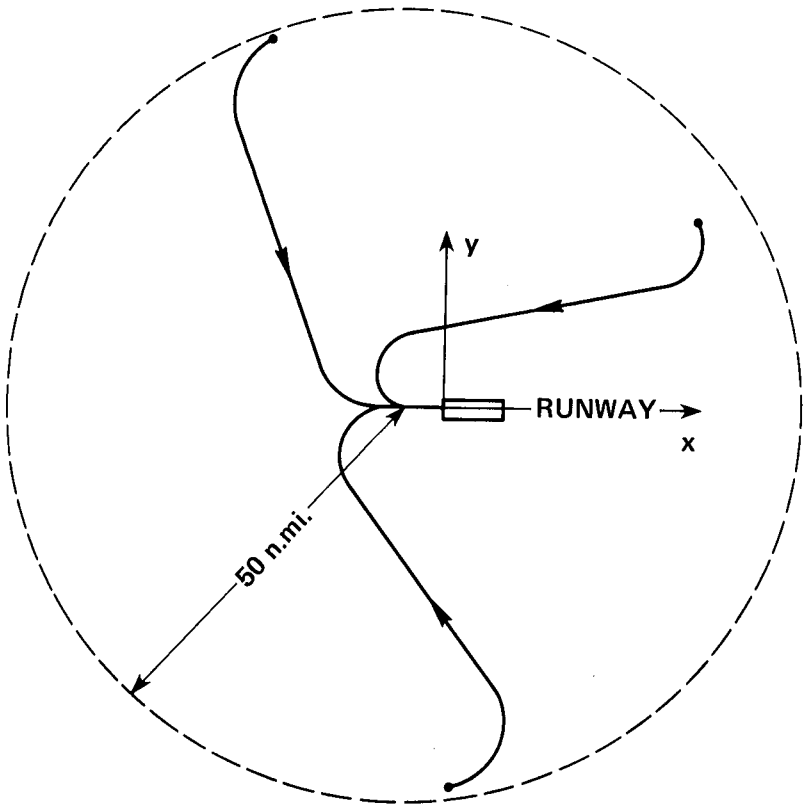

Figure 5.- x-y plot of sample capture flightpaths.

and does not contain the term $-Cv \cos \psi$ as the performance index (eq. (8)) of section 1:

$$J = \int F \, dt \tag{50}$$

The end conditions on the state variables are $h_o = h_f = 2{,}000$ ft, $v_o = 250$ knots IAS, $v_f = 180$ knots IAS, $0 \leq \psi_o \leq 180°$, and $0 \leq \psi_f \leq 180°$. For convenience, when generating extremals we usually choose as origin $x = 0$, $y = 0$, and $\psi = 0$ at the point of the trajectory where thrust is equal to drag. To move the flightpaths to the actual required terminal conditions is then a simple task of coordinate transformation.

The same drag and fuel flow models hold as in section 2 (eqs. (9)-(11)). The assumptions are also the same as in section 2. The Hamiltonian for the capture problem is

$$H = C_0 + C_1 T + C_2 T^2 + \lambda_x v \cos \psi + \lambda_y v \sin \psi + \lambda_h v\gamma - \lambda_\psi gu/v$$
$$+ \lambda_v g(T - D_1 - D_2 u^2 - W\gamma)/W + \eta[v - v_I(1 + qh)] \tag{51}$$

We observe that by setting $\lambda_y = 0$ and $\lambda_x = -C$, the Hamiltonian becomes identical to that of equation (12). Thus, the problem discussed in section 2 can be treated as a special case of the problem in this section. Furthermore, this observation ties our work to that of reference 1 where λ is the only adjoint variable (corresponding to the energy as the only state variable) and it turns out there that λ = constant = $-C$.

Comparing this with equation (12) we note that here λ_x and λ_y are not zero, but that $C = 0$. As before, the adjoint variables are defined by

$$\dot{\lambda}_x = -\frac{\partial H}{\partial x} = 0 \; ; \qquad \lambda_x = \text{constant} \tag{52}$$

$$\dot{\lambda}_y = -\frac{\partial H}{\partial y} = 0 \; ; \qquad \lambda_y = \text{constant} \tag{53}$$

$$\dot{\lambda}_h = -\frac{\partial H}{\partial h} = -C_{0_h} - C_{1_h} T - C_{2_h} T^2 + \lambda_v g(D_{1_h} + D_{2_h} u^2)/W + \eta v_I q \tag{54}$$

$$\dot{\lambda}_\psi = -\frac{\partial H}{\partial \psi} = \lambda_x v \sin \psi - \lambda_y v \cos \psi \tag{55}$$

$$\dot{\lambda}_v = -\frac{\partial H}{\partial v} = -C_{0_v} - C_{1_v} T - C_{2_v} T^2 - \lambda_x \cos \psi - \lambda_y \sin \psi - \lambda_h \gamma - \lambda_\psi gu/v^2$$
$$+ \lambda_v g(D_{1_v} + D_{2_v} u^2)/W - \eta \tag{56}$$

The differences between equations (12) and (51) are minor. When the minimum principle is applied, it is found that the controls are given by identical expressions, equations (17) and (18) for the thrust, (20) and (21) for the bank angle, and (23) and (24) for the flightpath angle, but, of course, the expressions from which the lambdas are integrated differ.

Flightpath Guidance along a Singular Arc

Again, when flying along a singular arc, equation (24) implies that all time-derivatives of H_γ must vanish. Inserting the value for $\dot{\lambda}_h$ (eq. (54)), $\dot{v}$ (eq. (5)), and $\dot{\lambda}_v$ (eq. (56)) into equation (25) and simplifying, the following equation for $\dot{H}_\gamma$ is obtained.

$$\dot{H}_\gamma = -F_h v + \lambda_v[vD_h + g(T - D)/v - gD_v]g/W + g(F_v + \lambda_x \cos\psi + \lambda_y \sin\psi + \lambda_\psi gu/v^2) \tag{57a}$$

Nonturning flight— Solution of the simultaneous equations $H = 0$ and $\dot{H}_\gamma = 0$ will permit the calculation of λ_x and λ_v for a nonturning flightpath because then $u = 0$, $\psi = 0$, $\lambda_y = 0$, $\lambda_\psi = 0$, and λ_h is given by equation (24). The additional assumption is made that the solution is not bounded by the speed constraint, $\eta = 0$. With $u = \psi = \lambda_y = 0$, the equations for H (eq. (51)) and $\dot{H}_\gamma$ (eq. (57a)) simplify to permit the construction of nonturning optimal flightpaths by forward and backward integration, while starting somewhere on a portion of the flightpath where optimum thrust is intermediate, because at such a point there is only one possible λ_v.

$\dot{H}_\gamma = 0$ results in

$$\lambda_v g[D_{1_h} v - D_{1_v} g + (T - D_1)g/v]/W + gF_v - F_h v + g\lambda_x = 0 \tag{57b}$$

where equations (C10), (C12), and (C14) (appendix C) were used. $H = 0$ results in

$$\lambda_v g(T - D_1)/W + F + \lambda_x v = 0 \tag{58}$$

where F is defined in equation (C1). Equations (57b) and (58) are solved for λ_v and λ_x

$$\lambda_v = \frac{-W(F_v g - Fg/v - F_h v)}{g(D_{1_h} v - D_{1_v} g)} \tag{59}$$

$$\lambda_x = -F/v - \lambda_v g(T - D_1)/(vW) \tag{60}$$

Setting $\lambda_x = -C$, equations (58) and (59) reduce to equations (30a) and (30b), respectively. Note that λ_v is a function of the unknown thrust via F, F_v, and F_h. When the thrust is intermediate, equation (18) must also hold, and can be solved for λ_v:

$$\lambda_v = -(2C_2 T + C_1)W/g \tag{61}$$

To find starting values for the states and adjoint variables, we can now equate equations (59) and (61). An intermediate thrust, for example, $T = D_1$, is chosen, and for a given altitude h, v is numerically changed until the equality between equations (59) and (61) has been achieved. Once one has a consistent v and h pair one can solve equation (60) for the numerical value of λ_x. For the example $T = D_1$ in equation (60), $-\lambda_x$ is simply F/v, the cruise fuel consumption in pounds per foot. As will be explained later, these initial values can also be used for the

turning flightpath or, as shown next, they can be used to calculate the speed-altitude profile of the variable-thrust portion of the singular-γ arc for a non-turning flightpath.

We will first describe how we calculated the altitude-speed profile for the non-turning flightpaths without first calculating γ directly. Such a calculation is a valuable check on the results for the general turning flightpath where γ must first be very laboriously computed. The altitude-speed profile is computed in the following manner. In equations (57b) and (58), one replaces λ_v from equation (61) and also replaces F, F_v, and F_h by the expressions (C1), (C2), and (C4) given in appendix C. The equation for $H = 0$ (eq. (58)) can then be solved for the thrust,

$$T = D_1 \pm [D_1^2 + (C_0 + C_1 D_1 + \lambda_x v)/C_2]^{1/2} \tag{62}$$

where it turns out that the positive sign is used for the higher-speed part of the variable thrust trajectory and the negative sign for the lower-speed part. Then, beginning with the consistent v,h pair, we change v slightly and calculate the value of T from equation (62) which is inserted into (61) to get λ_v, which is then put into (57b). Then h is iteratively adjusted in all three of the above equations ((62), (61), (57b)) until (57b) holds. Thus, a consistent set of v, h, and T is found. Then v is changed by a few knots and the process is repeated. This continues until $T = 0$ in one direction of the speed change and $T = T_{max}$ in the other direction of the speed change. We now must obtain the portions of the singular arc in which the thrust is limited to either T_{max} or T_{idle}. To do this, equation (58) is solved for λ_v. For $T = 0$, a speed v slightly smaller than the last speed obtained for $T = 0$ is chosen in equation (58), and a smaller h is also chosen. The resulting λ_v is inserted into equation (57b), and h is iteratively adjusted both in the equation for λ_v from equation (58) and in (57b) until the equality in (57b) holds true. Then a smaller v is chosen and the process is repeated, each time finding a new v,h pair to obtain the descent altitude-speed profile at $T = 0$. The same process holds true for $T = T_{max} = \text{constant}$, to obtain the climb altitude-speed profile. During these iterations we must check in equations (17) and (18) that the thrust remains at its respective limit.

We can now calculate complete altitude-speed profiles of nonturning terminal area flightpaths and the associated thrust. The bank angle, of course, is zero, and the flightpath angle γ can be calculated from equation (32). At the point $T = D_1$, $dh/dv = -v/g$ and equation (32) becomes indeterminate, (0/0). Since the thrust varies with time, this occurs only for an infinitesimal interval and is of no consequence. Also, if for some altitude-speed profile for $T = D$, $\gamma = 0$, the flightpath length would be infinite. As expected, this does not happen for our model, which is valid only over the range of 0-10,000 ft, since the minimum-fuel cruise altitude is above 30,000 ft.

In the results section it is shown that the climb and descent altitude-speed profiles differ, depending on the maximum altitude of the flightpath. To study this effect algebraically, for a given altitude h in equations (57b) and (58) all the variables are replaced by more fundamental quantities from appendix C until a single equation is obtained, which is a polynomial in v and has coefficients that are combinations of the thrust and drag coefficients and the altitude. The resulting polynomial for the constant thrust climb and descent profiles is of the form

$$v^7 + a_1 v^6 + a_2 v^5 + a_3 v^4 + a_4 v^3 + a_5 v^2 + a_6 v + a_7 + \lambda_x (a_8 v^7 + a_9 v^5 + a_{10} v) = 0 \tag{63}$$

This is a seventh-order polynomial in v, which depends on λ_x. Numerical results for intermediate thrust show that each different λ_x defines a portion of an altitude-speed profile which does not intersect with any other such altitude-speed profile. Since the polynomial (63) changes with change in λ_x associated with each λ_x is also a different climb and descent profile.

Turning flight— Just as in section 2, the equations for the λ's can be derived from $H = 0$ and from $\dot{H}_\gamma = 0$ for the different constrained and intermediate values that the controls T and u might take. For example, the case in which controls are intermediate, $u_{min} < u < u_{max}$ and $0 < T < T_{max}$, equations (51) and (57a) are solved in the same way as (12) and (25) were solved,

$$\lambda_v = \frac{b_1 - b_2}{2(b_3 - b_4)} \pm \left\{ \left[\frac{b_1 - b_2}{2(b_3 - b_4)} \right]^2 - \frac{b_5 - b_6}{b_3 - b_4} \right\}^{1/2} \tag{64}$$

$$\lambda_\psi = \pm \left[\lambda_v (b_3 \lambda_v^2 + b_1 \lambda_v + b_5) \right]^{1/2} \tag{65}$$

where the b coefficients are functions of g, v, h, ψ, λ_x, λ_y, and of the thrust and drag coefficients. Similar expressions hold for other cases of combinations of constrained and intermediate controls. For reasons similar to those given in section 2, equations (64) and (65) are not actually needed for the calculation of the singular arc; thus, the coefficients are not given. However, the structure of these equations tells us something about the solution. Since medium-length flightpaths are desired rather than short highly turning ones, equations (64) and (65) are appropriate for the portion of such flightpaths, which must have intermediate controls, especially small u's, which means small λ_ψ's. The choice of the plus or minus sign in front of the square root in the expression for λ_v is determined by that sign that makes the expression agree numerically with the initial value given by equation (59). The plus and minus signs in the expression for λ_ψ indicate that right or left turns may be chosen.

Now the flightpath angle γ can be obtained by a procedure identical to that described in section 2, equations (35)-(38). Taking the derivative of equation (57) gives

$$\begin{aligned} (\ddot{H}_\gamma) &= \partial \dot{H}_\gamma / \partial t \\ &= \partial / \partial t \{ -F_h v + \lambda_v [D_h v + g(T - D)/v - g D_v] g/W \\ &\quad + g(F_v + \lambda_x \cos\psi + \lambda_y \sin\psi + \lambda_\psi g u / v^2) \} \end{aligned} \tag{66}$$

Note that this expression differs from equation (35) only in the addition of the λ_x and λ_y terms and the absence of the $C \cos\psi$ term. Using the same mathematical procedure as before, we can write an equation analogous to equation (36),

$$(\ddot{H}_\gamma) = A_H^* \dot{v} + B_H^* \dot{h} + C_H^* \dot{\psi} + D_H^* \dot{\lambda}_v + E_H \dot{\lambda}_\psi \tag{67}$$

where E_H is as before in equation (37), and the other coefficients have the following values:

$$
\begin{aligned}
A_H^* &= A_H + g^2\lambda_v\tau_v/(Wv) + \tau_v(gF_{vT} - vF_{hT}) && 0 < T < T_{max} \\
&= A_H && T \equiv 0,\ T \equiv T_{max} \\
B_H^* &= B_H + g^2\lambda_v\tau_h/(Wv) + \tau_h(-vF_{hT} + gF_{vT}) && 0 < T < T_{max} \\
&= B_H && T \equiv 0,\ T \equiv T_{max} \\
C_H^* &= -g(\lambda_x \sin\psi - \lambda_y \cos\psi) \\
D_H^* &= D_H + \tau_{\lambda_v}(g^2\lambda_v/(Wv) - F_{hT}v + gF_{vT}) && 0 < T < T_{max} \\
&= D_H && T \equiv 0,\ T \equiv T_{max}
\end{aligned}
\tag{68}
$$

and the nonstarred coefficients are those of equation (37). The additional terms in the coefficients are due to the change in the thrust while on the portion of the flightpath where that happens. The partial derivatives of the thrust τ_v, τ_h, and τ_{λ_v} are defined in appendix C. When the thrust is constant in the climbout and descent τ_v, τ_h, and τ_{λ_v} are set to zero. We can now insert the values for the derivatives $\dot{v}$, $\dot{h}$, $\dot{\psi}$, $\dot{\lambda}_v$, and $\dot{\lambda}_\psi$ from equations (3), (4), (5), (55), and (56) into (67) and solve the resulting equation for γ:

$$
\begin{aligned}
\gamma = [&A_H^* g(T - D)/W - C_H^* gu/v + D_H^*(-F_v - \lambda_x \cos\psi - \lambda_y \sin\psi - \lambda_\psi gu/v^2 + \lambda_v gD_v/W) \\
&+ E_H(\lambda_x v \sin\psi - \lambda_y v \cos\psi)]/(A_H^* g - B_H^* v + D_H^* \lambda_h)
\end{aligned}
\tag{69}
$$

For equation (69) to be a candidate for an optimal solution, the generalized Legendre-Clebsch condition must hold:

$$
(-\ddot{H}_\gamma)_\gamma = A_H^* g - B_H^* v + D_H^* \lambda_h > 0 \tag{70}
$$

Equations (69) and (70) are similar to equations (38) and (39). This concludes the derivation of the singular γ.

Flightpath Guidance along a Speed-Constraint Arc

Since the state equations (1)-(5) in section 2 are applicable to this section as well, and, since there is only a small difference in the Hamiltonian (compare eqs. (12) with (51)), equations (40)-(45) apply. One change occurs in equation (45) where $-C \cos\psi$ is replaced by $\lambda_x \cos\psi + \lambda_y \sin\psi$. Then

$$
A_\eta = C_{0_v} + C_{1_v}T + C_{2_v}T^2 + \lambda_x \cos\psi + \lambda_y \sin\psi + \lambda_h\gamma + \lambda_\psi gu/v^2 - \lambda_v gD_v/W \tag{71}
$$

Conditions similar to those discussed in section 2 hold for the transition from the singular arc to the speed-limited arc. Recplacing C by $-\lambda_x$ in equation (47) gives the expression for λ_v on the speed-limited arc. The resulting expression is identical with equation (60) for the singular arc solved for λ_v. Again, this means that there is no jump in λ_v at the transition, and it can be computed on the whole path by integrating equation (56).

Computation of Extremals

The extremals are computed by numerical integration of the state and adjoint equations (1)-(5) and (54)-(56) with the thrust given by equations (17) and (18), u given by (19)-(22), and γ given by (69) on the singular arc or by (23) after getting off the singular arc at both ends of the flightpath. The adjoint variables λ_v and λ_ψ are obtained by integrating equations (55) and (56) but on the singular-γ arc, λ_h is found directly from equation (24); off the singular arc it is found from equation (54).

A representative set of capture flightpaths is obtained by restricting the initial and final altitudes and initial and final speeds to a specific set. Flightpaths of different lengths and with different magnitudes of initial and final turns are needed. This is achieved by using the following strategy. Nonturning flightpaths, which have the $T = D$ point at different altitudes and which, therefore, have different lengths, are generated. Starting from the initial states and adjoint variables obtained by the earlier described procedure involving equations (59)-(61), we integrate forward and backward in time. In this manner we obtain the altitude-speed profile for the nonturning path and we also obtain and store initial conditions (h, x, v, λ_h, λ_v, T, γ) along the path, which may later be used as initial conditions for the turning paths. Then, for turning paths, a point $u = 0$, $\lambda_\psi = 0$ is chosen anywhere along the arc where the initial conditions have been saved, and a λ_y is chosen by trial and error to achieve the desired turns as determined by forward and backward integration. The sign and magnitude of λ_y determine the magnitude and direction of the turns. By choosing the $\lambda_\psi = u = 0$ point closer to one endpoint or the other, we control which end of the flightpath will turn the most. The turn farthest away from the initial point will have the larger magnitude turn. In this manner we can generate sets of flightpaths with similar altitude speed profiles, which individually are distinguished by their initial and final turns.

A singular arc usually forms a portion of a complete speed-limited trajectory, because it has portions that are below the speed limit of 250 knots IAS. Since the singular arc has the most severe restrictions on the values of the costate variables, we always begin integration of an extremal on the singular arc. Once the speed limit has been reached, we transfer to the speed-limited arc by using equations (40)-(45a) and (71) and with present values of the λ's as initial values.

The portion of the singular arc that is below the speed limit is primarily the unpowered descent. Hence, by storing all states and adjoint variables at a point below the speed limit, while computing sets of complete singular-arc trajectories without speed limit, we can obtain initial conditions for speed-limited trajectories that have final turns that are identical with those of the nonspeed-limited set of trajectories. Hence, final turns for speed-limited trajectories need not be studied separately.

4. RESULTS FOR CLIMB-OUT AND DESCENT

Nonturning Flight

We will first discuss the special cases for ascent and descent whose ground tracks are a straight line ($\Delta\psi = 0$) and show that our results agree with those of reference 1. (We will call those flightpaths nonturning flightpaths for short.) This will be followed with results for optimal turning ascents and descents. For the following comparisons of the fuel efficiency of different flightpaths, it should be

noted that the flightpaths are not necessarily of the same lengths. However, the comparison is valid by having the term Cv cos ψ in the performance index (8). This term corrects for the effect of the length of the low-altitude path on the fuel consumption for the complete path.

Figure 6(a) is a plot of the altitude-versus-speed profiles for nonturning climb and descent. The thin line is representative of a figure from reference 1 for a 200-n. mi. altitude-speed profile, which we will use for comparison with our results. The singular-arc ascent profile, denoted by the number 1 in figure 6, is above the FAA terminal-area speed constraint. The altitude-versus-speed profile connects to the profile for the complete 200-n. mi. path (point A) at a speed somewhat less than the speed at which the ascent is resumed from the 10,000-ft altitude (point B). This is a result of a conservatively chosen T_{max} of 23,000 lb. By setting T_{max} at 25,000 lb, the 10,000-ft intercept shifts to 338.5 knots (point B), indicating that the following climb is the continuation of the singular arc. It is thought that this is closer to the effective T_{max} used in reference 1. The FAA often permits a climb-out faster than 250 knots IAS. In this case, the optimal (singular-arc) climb-out saves 36 lb of fuel for the complete 200-n. mi. path compared with the speed-limited climb-out, denoted by the 2 in figure 6, which is followed by an acceleration to the

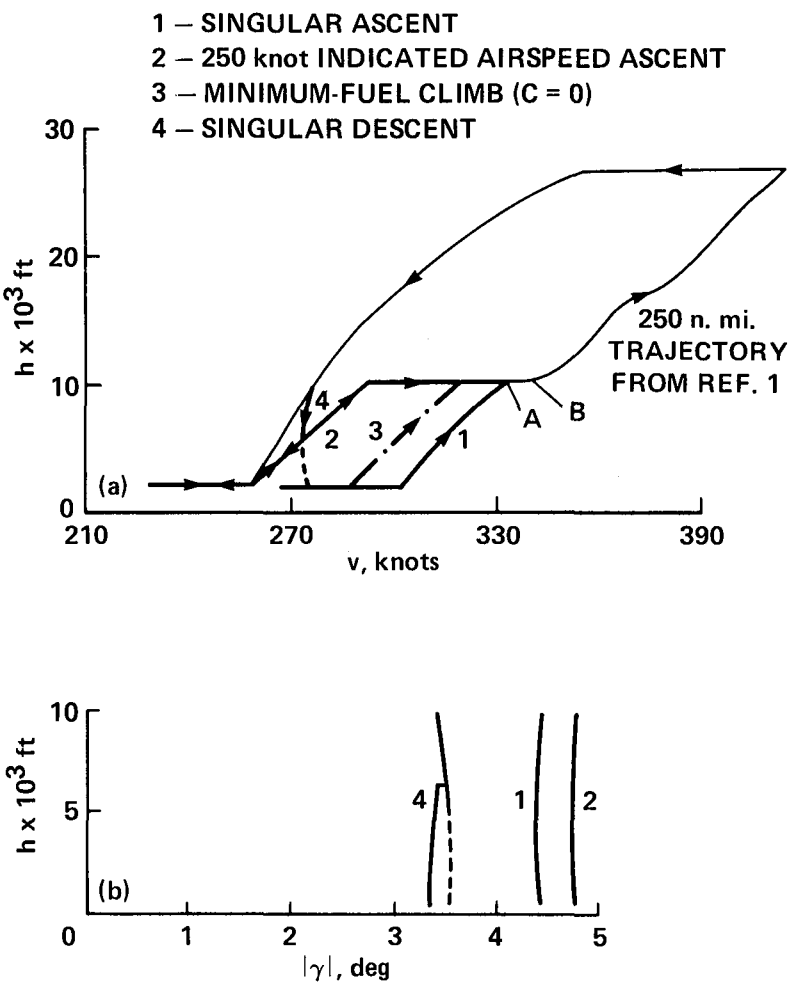

Figure 6.- Straight-line optimal flightpaths. (a) Altitude-speed profile; (b) flightpath angle command.

singular-arc speec at the 10,000-ft altitude (point B). Figure 6 also shows (dash-dot line 3) the singular-arc climb when $C = 0$ in equation (8), which would be the optimum climb profile if the cruise had not been considered. Then, an acceleration to the speed at point B (fig. 6) is required, and the total fuel consumption is higher than it is for the singular-arc climb with $C \neq 0$ in equation (8), but less than the fuel consumption for the speed-limited climb.

The start of the singular-arc optimal descent speed, on curve 4 in figure 6(a), is below the speed limit of 250 knots IAS, denoted by curve 2 in figure 6(a) and turns more sharply toward the speed constraint than the altitude-speed profile given in reference 1. Therefore, it meets the speed constraint at a higher altitude than the example in reference 1. From this point on, one can continue on the singular arc and violate the speed constraint (dashed line), or one can continue on the speed constraint (curve 2). This we shall call a mixed descent. The altitude-speed profiles are very sensitive with respect to small differences in the engine-idle fuel-flow model. For instance, when the modeled engine-idle flow is reduced to one third that of the present value, the singular descent altitude-speed profile will always remain below the 250-knot-IAS constraint. Once the model is fixed, the resulting fuel consumption is not very sensitive with respect to the altitude-speed profile. For instance, flying the mixed descent requires less than 1 lb more fuel than flying the pure singular-arc descent (dashed-line extension of 4). Figure 6(b) shows that for both climb and descent, the γ's remain almost constant with altitude, which makes flying these flightpaths relatively easy. With our results for nonturning climbout and descent agreeing well with those of reference 1, we shall first look at the data for turning-climbout flight and then at those for turning descents.

Turning Flight

Solutions to the optimization problem for the singular arc that include ascending turns result in altitude-speed profiles that are practically identical to those of the straight-line optimization problem (see fig. 7(a)). Most of the turn occurs in level flight before ascent from the minimum maneuvering altitude of 2,000 ft in this study (see fig. 7(b)). In general, the greater the permissible range of a control, the better will be the performance of a system. This idea was tested for our example by removing the restriction on the minimum altitude and defining $\gamma_{min} = -4°$ instead of 0°. The resulting extremals are shown in figure 7(c). The performance index versus total turn angle was plotted (not shown) for both types of climb-outs. The fuel consumption (as measured by the performance index, eq. (8)) was about 20 lb less for the flightpath with the increased range in permissible γ, independent of the turn. This is about 2% of the fuel for the climb-outs to 10,000 ft. For the only paths for which a direct comparison can be made, the nonturning flight, it was noted that the primary fuel savings were obtained by reducing the time it took to fly from the initial point at 2,000 ft altitude to the 2,000-ft altitude point on the singular arc. All turns in figure 7 are flown at maximum thrust (eq. (17)) and at γ_{min} (eq. (23)). To illustrate further the above statements, the numerical values for the key flightpath variables are summarized in table 1 as a function of the total heading change for both the singular arc of figure 7 and speed-constrained ascents (which are not shown graphically). We notice from table 1 that the speed at which ascent begins (column 3) depends on the type of ascent and not on the required total heading change (column 2). A similar statement is largely true for the initial flightpath angles, which vary only minimally (column 4). The bank angles experienced during both the entire turning singular arc and speed-constrained climb-outs are shown as functions of the heading change in figures 8(a) and 8(b), respectively. We

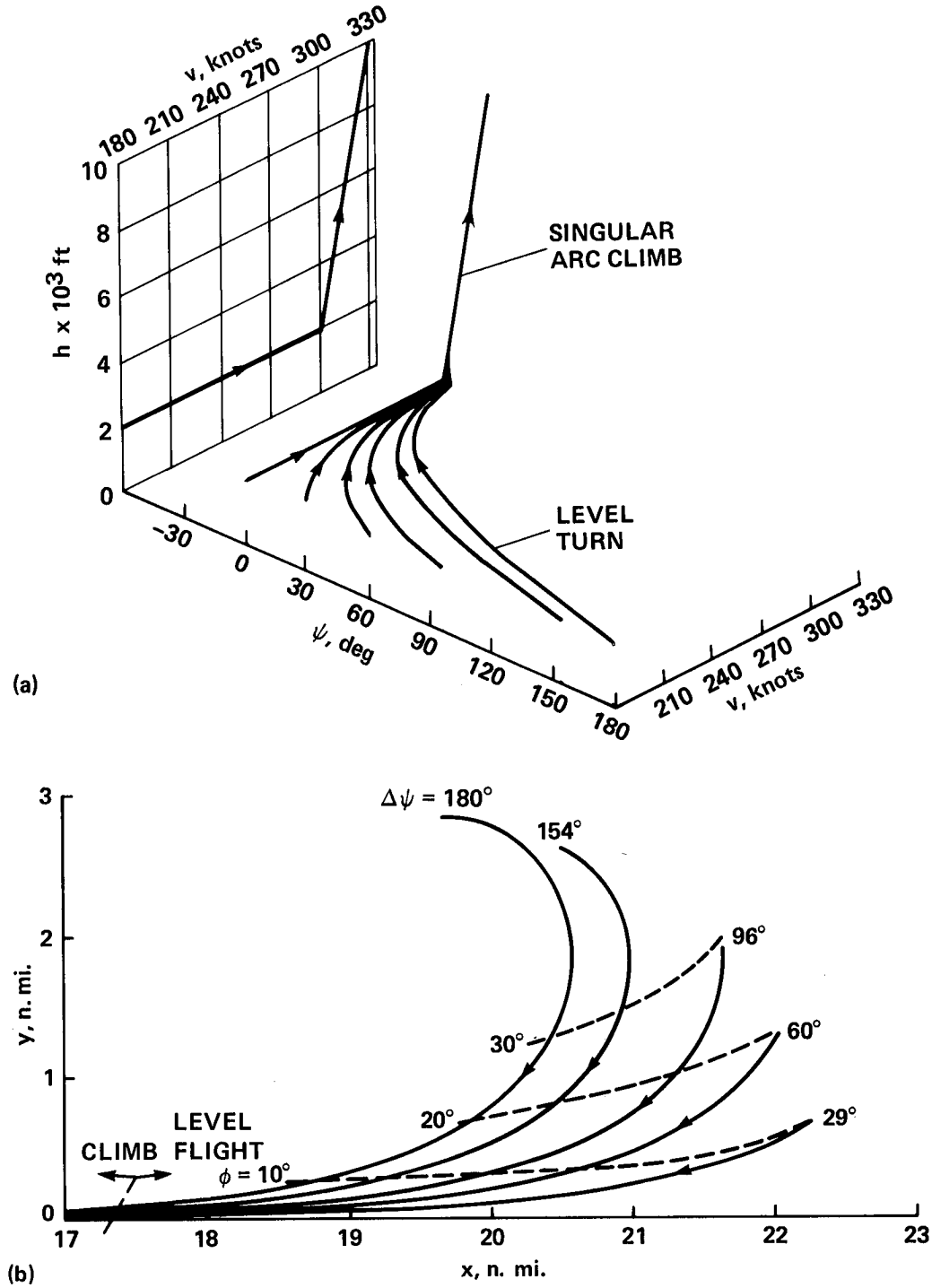

(a) Field of extremals and v-h diagram: $\gamma_{max} = 5°$, $\gamma_{min} = 0°$.

(b) x-y plot of the turns.

Figure 7.- Optimum turning climb-out on the singular-γ arc: final point x = 0, y = 0, h = 10,000 ft.

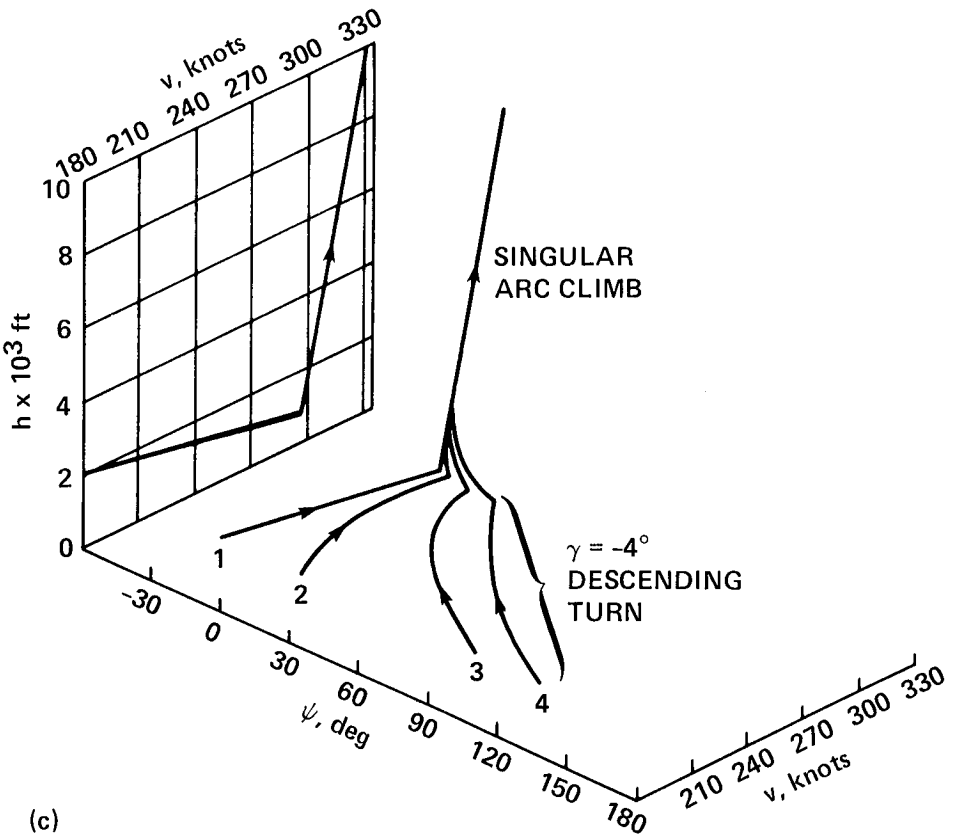

(c) Field of extremals and v-h diagram: $\gamma_{max} = 5°$, $\gamma_{min} = -4°$.

Figure 7.- Concluded.

TABLE 1.- NUMERICAL VALUES OF KEY FLIGHTPATH VARIABLES IMMEDIATELY AFTER SWITCH-OVER FROM LEVEL TURN TO CLIMB (for case $\gamma_{min} = 0°$)

Case (1)	$\Delta\psi_{total}$, deg (2)	v, knots (3)	γ, deg (4)	$\Delta\psi$ to go, deg (5)	ϕ, deg (6)	Type of ascent
I	0	301.7	4.356	0	0	Singular arc
II	90	301.7	4.355	1.6	1.7	Singular arc
III	180	301.7	4.353	5.2	5.2	Singular arc
IV	0	258.1	4.79	0	0	Speed constrained
V	90	258.1	4.76	9.2	7.2	Speed constrained
VI	180	258.1	4.65	30	17.8	Speed constrained

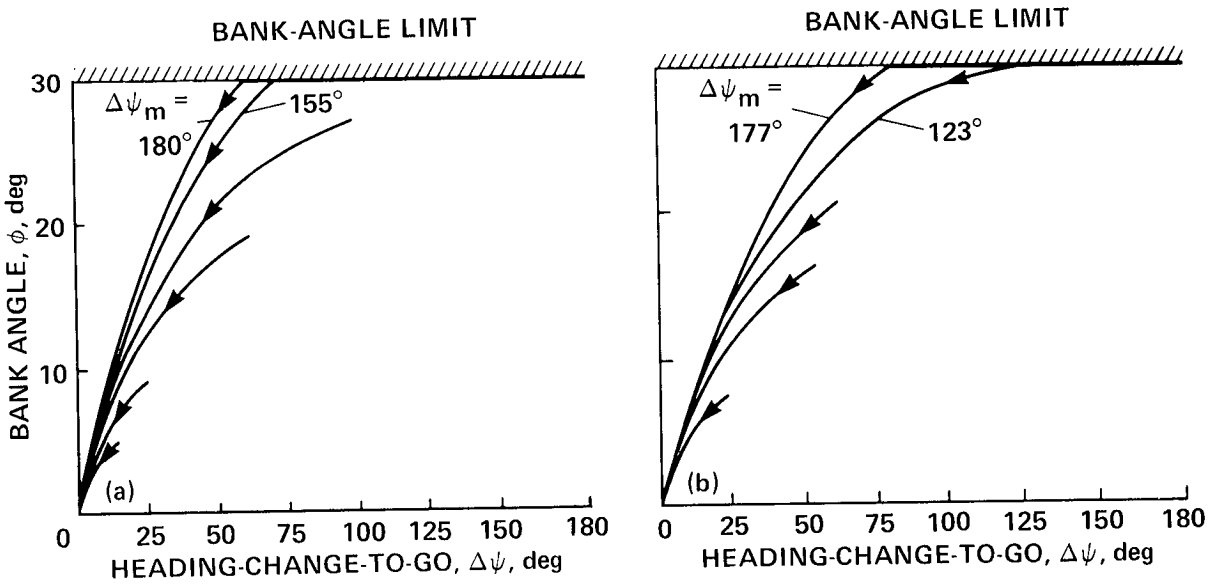

Figure 8.- Bank angle versus heading-change-to-go in optimal climb-out; $\Delta\psi_m$ = maximum heading change. (a) Singular γ-arc climb; (b) speed-constrained climb.

notice that the bank angles gradually go to zero as the desired heading ($\Delta\psi = 0$) is approached. As table 1 shows for case III, which is the 180° turn, the bank angle at the point of switching from level flight to climb is already as small as 5.2°, the early part of the turn is flown at or nearly at the maximum bank angle. Intuitively, this makes sense, because while flying away from the target we must turn as fast as possible. (This is true in spite of the opposite effect that maximum bank angle has on acceleration, which also must be maximized.) The penalty for observing the speed constraint is still 36 lb of fuel, independent of the amount of turn.

The altitude-speed profile for the singular-arc climb (fig. 7(a)), can be well approximated by a constant-IAS climb. If we set the speed constraint to a value that corresponds to the singular-arc speed at 10,000-ft altitude — 331.4 knots — the resulting performance is basically identical with the singular-arc performance.

In figure 9, we compared two minimum-fuel, speed-constrained climbs (both for a heading change of 68°): one that has the term $Cv \cos\psi$ in equation (8) and another with $C = 0$. The latter indeed takes 7 lb less fuel, but it climbs in an x-distance that is 2.93 n. mi. shorter, thus requiring an additional 52 lb of fuel for the longer cruise. The bank-angle histories, shown in figure 9(b), are quite different for the two cases.

For the optimum descent, only an extremal starting with a singular-arc descent is a candidate for optimality (fig. 10(a)). Figure 10 illustrates the more restricted but also more realistic case, in which we forced a level turn after leaving the descending arc by constraining the permissible γ to a narrow range by restricting γ_{min} to -0.001°. Since such a state-dependent control constraint has not been taken into account optimally, this is, strictly speaking, a suboptimal procedure. We note here that this turning descent has actually three phases: singular-arc, speed-constrained arc, and level-deceleration. Again, most of the turn occurs in level flight (fig. 10(b)) and the altitude-speed profiles are identical within the power of resolution of the graph (fig. 10(a)). Figure 11 shows the bank angles versus

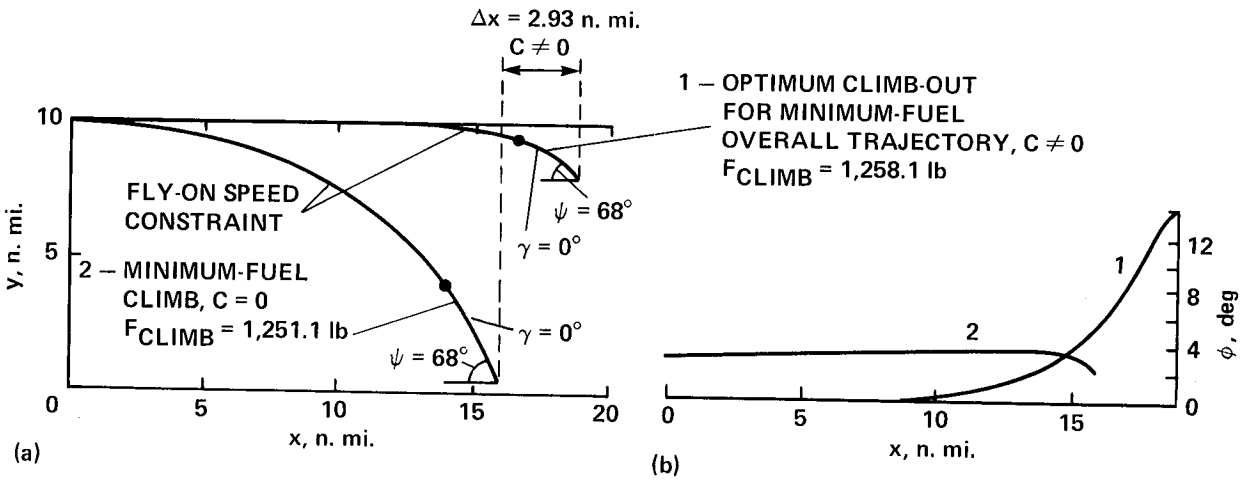

Figure 9.- Comparison of two types of speed-constrained optimal climb-outs. (a) Horizontal projection; (b) bank-angle histories.

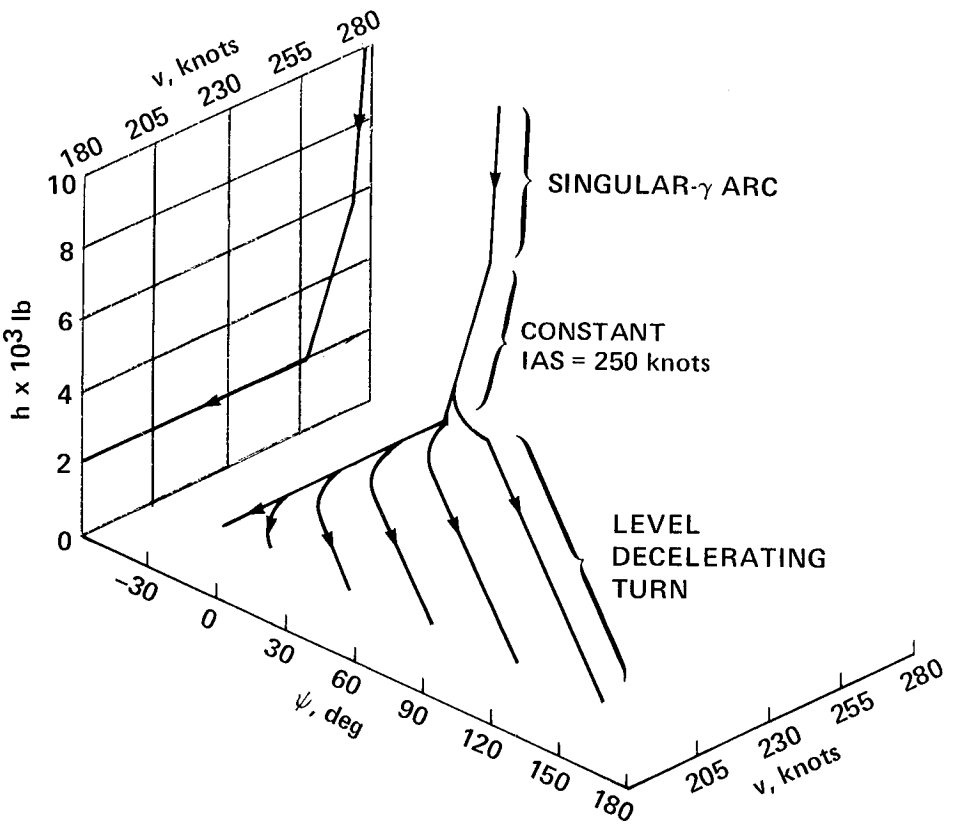

(a) Field of extremals and v-h diagram where $\gamma_{max} = 0°$, $\gamma_{min} = -0.001°$.

Figure 10.- Optimum turning descent with forced level turn: origin x = 0, y = 0, h = 10,000 ft.

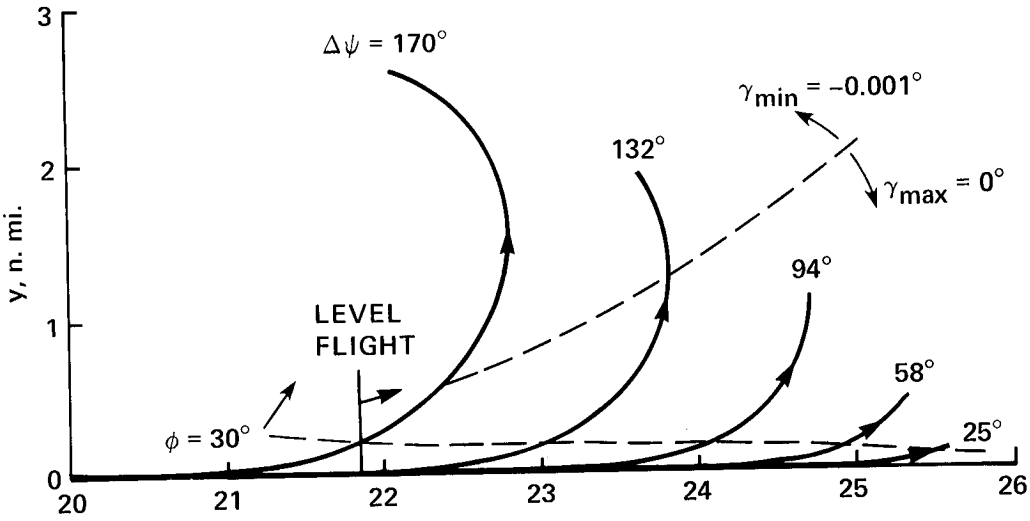

(b) x-y plot of the turns where $\gamma_{max} = 0°$, $\gamma_{min} = -0.001°$.

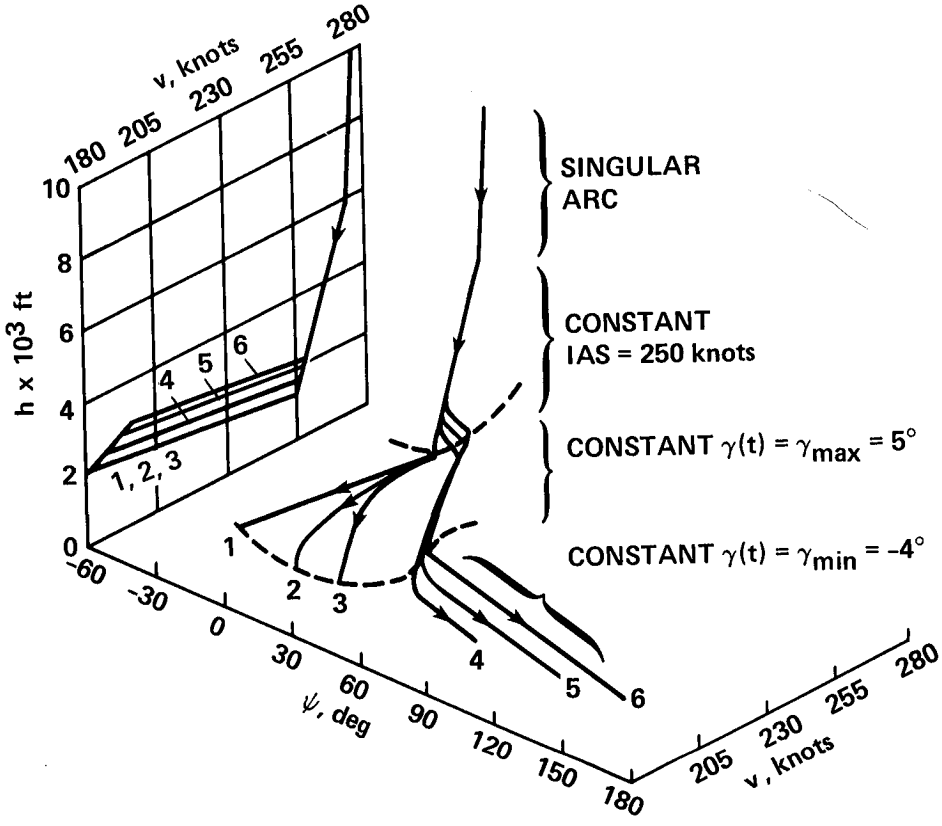

(c) Field of extremals and v-h diagram where $\gamma_{max} = 5°$, $\gamma_{min} = -4°$.

Figure 10.- Continued.

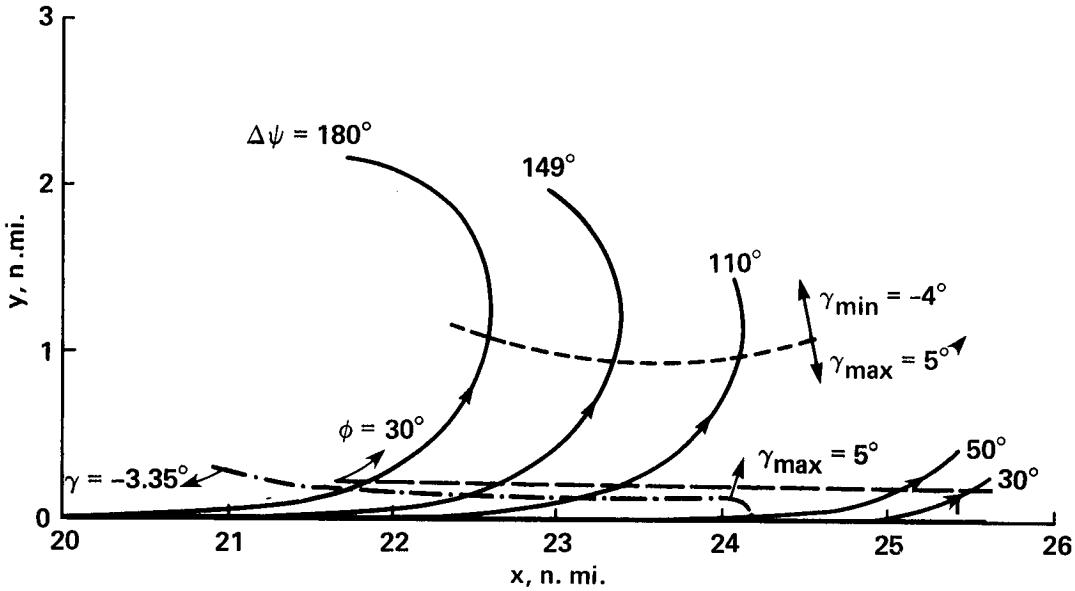

(d) x-y plot of the turns where $\gamma_{max} = 5°$, $\gamma_{min} = -4°$.

Figure 10.- Concluded.

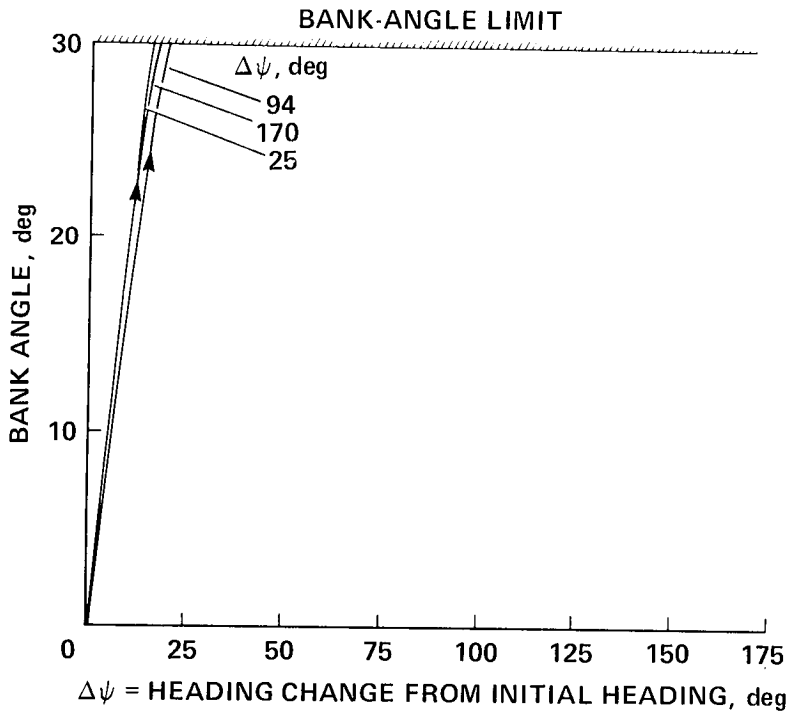

Figure 11.- Bank angles versus heading change for descent of figures 10a and 10b.

heading. The bank angles essentially follow the same curve, independent of the total heading change. This allows a simple approximation of the optimal descent in an on-board algorithm. Note that for this example the beginning of the turn is executed with gradually increasing bank angle until, for heading changes greater than 25°, the bank angle is at its maximum for all but the first part of the turn.

Again, for the descent, we removed the restriction on the minimum altitude and defined $\gamma_{max} = 5°$ and $\gamma_{min} = -4°$. The resulting extremals are shown in figure 10(c). The performance index was plotted (not shown) for both types of descents versus total turn angle. The fuel consumption (as measured by the performance index (eq. (8)) was about 2.5 lb less for the flightpaths with the increased range in permissible γ, independent of the turn. This is a saving of about 1.2% for the straight-line descent and of 1.6% for the 180° turning descent from 10,000 to 2,000 ft.

In the cases illustrated in table 2, the initial descent is completed on the singular arc, and the speed limit is disregarded. Table 2 summarizes the numerical values for the key flightpath variables as functions of the total heading change, $\Delta\psi$. The entries in table 2 are similar to those in table 1, except for the addition of colume 3, which indicates the altitude at which the system leaves the singular arc. The situation for descent is somewhat more complex than for the climbout; this will be explained by means of the six representative cases in table 2.

For small turn angles (see cases I and II, table 2), the singular descent to 2,000 ft is followed by a horizontal decelerating turn. As stated earlier, for large angles of turn the optimal path required a change in γ from γ_{max} (level flight) to γ_{min} part way in the final turn, after having left the singular arc (see cases III and IV, table 2). The changes in altitudes for γ-switching that are required would make an on-board algorithm quite complex. Therefore, the following test was made. Upon leaving the singular arc we forced the aircraft to stay at 2,000 ft by setting very narrow limits for maximum and minimum γ (see cases V and VI, table 2). We find that there is a negligible difference between performances for the optimal case with the γ-switching cases III and IV and the corresponding constant-altitude decelerating turn cases V and VI.

TABLE 2.- NUMERICAL VALUES OF KEY FLIGHTPATH VARIABLES IMMEDIATELY BEFORE SWITCH-OVER FROM SINGULAR ARC DESCENT TO LEVEL TURN

Case	$\Delta\psi_{total}$, deg	h switch to level turn	v, knots	γ, deg	$\Delta\psi$ during initial descent, deg	ϕ, deg	Comments
(1)	(2)	(3)	(4)	(5)	(6)	(7)	
I	0.4	2000	258.6	-3.35	0.0	0.0	$\gamma_{max} = 0°$, $\gamma_{min} = -4°$
II	58.1	2000	258.6	-3.35	0.0	.02	Aircraft optimally wants to stay at γ_{max}
III	109	2025	259.1	-3.28	3.6	3.6	$\gamma_{max} = 0°$, $\gamma_{min} = -4°$
IV	166	2591	257.1	-3.28	4.6	4.6	γ switches to γ_{min} after initial level turn
V	132	2000	258.6	-3.35	1.3	2.3	$\gamma_{max} = 0°$, $\gamma_{min} = -0.001°$
VI	170	2000	258.1	-3.78	20.0	30.0	System forced to level turn

It is not possible to extend the forced level turn case optimally to a full 180° turn. At the initial value for λ_ψ needed to turn $\Delta\psi = 170°$ the singular arc is left at the desired altitude of 2,000 ft just before the bank angle reaches $\phi_{max} = 30°$. If one increases λ_ψ to force a larger turn, ϕ_{max} is reached while still on the singular arc. As a consequence of $\dot{u} = 0$ in (38) the singular γ switches to a positive value for a quick decelerating turn. Since $\gamma_{max} = 0°$ is violated, we must get off the singular-γ arc as soon as u_{max} is reached. However, for purposes of a possible on-board algorithm, we studied a 180° turn singular-γ descent such that when u_{max} is reached before the 2,000-ft altitude, we hold $u = u_{max}$ and then continue nonoptimally at constant $\gamma_{min} = -4°$ to 2,000 ft, followed by $\gamma_{max} = 0°$ such that $v_{final} = 180$ knots is reached at the completion of the turn. Again, there is only a 3.2 lb increase in the fuel used for this case over that used in the optimal descent, which left the singular arc at a higher altitude (similar to cases III and IV in table 2).

The question of global optimality remains. We must find all extremal controls and choose one with the lowest fuel consumption. We have shown earlier that on the singular arc and on the speed limit we have single-parameter families of extremals. The variations of those parameters were very small in order to cover the range of final headings. For larger changes of the parameters we get descending or ascending turns that include a 360° loop. Such loops and turns above 180° are not likely to be optimal, since they could be replaced by smaller turns using less fuel. By restricting turns to 180° and less, we believe our extremals to be globally optimal, but we have no proof.

We conclude this discussion by noting that we did not explore extremals where γ is always on its maximum or minimum bound rather than including singular arcs. Although it is easy to generate such extremals, it is extremely hard to meet our desired end conditions.

Comparison with Suboptimal Procedures

The question is often asked how much fuel is saved by using the optimal procedure. Such questions are difficult to answer, since we must ask: "What should the optimal procedure be compared with?" To have a valid comparison of optimal and suboptimal paths, we have to match the end conditions: speed, altitude, and heading. However, we need not match the path length because the effect of different path lengths is taken into account by the term $Cv \cos\psi$ in the performance index (eq. (8)). We shall compare the suboptimal paths with those optimal ones that include a level turn.

We shall first compare optimal climb-outs with reasonable suboptimal climb-out procedures, which more and more closely mimic the optimal. In order to meet the terminal conditions we will fly at least the latter part of the climb-out at an approximation of the optimal altitude-speed profile. Such an approximation is a climb at maximum thrust at a flightpath angle that is the average of the singular-arc angles. We consider three procedures which begin with a maximum bank-angle turn at constant $\gamma = 0$, at $\gamma = 3°$, and at a constant rate of climb of 500 ft/min until the desired heading is reached. This is followed by a nonturning path (at the same γ or $\dot{h}$) until the approximation of the optimal h-v profile is reached, which is then followed. This is illustrated in figure 12(a). (The paths were found by backward integration and some search to obtain the correct initial altitude.)

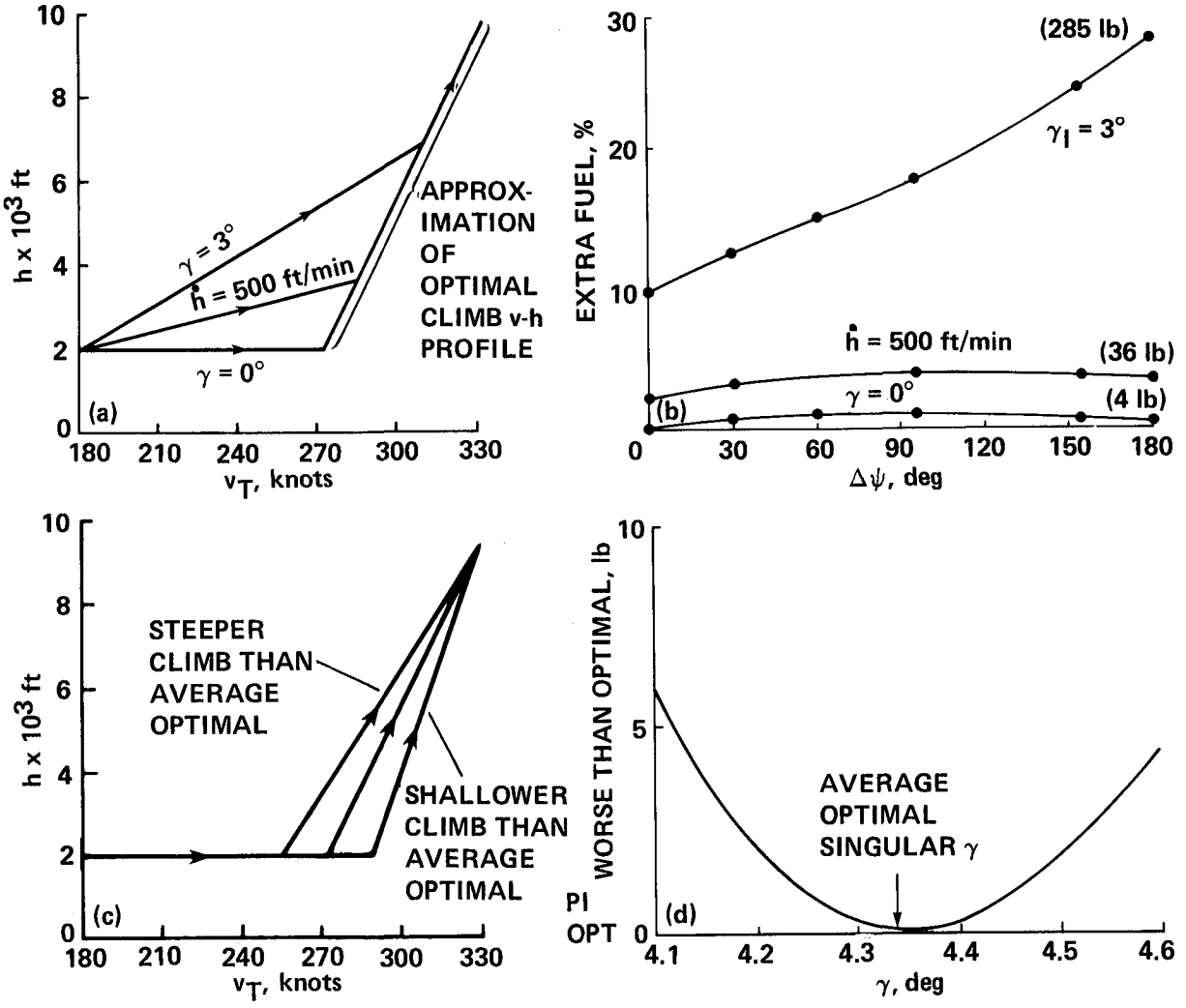

Figure 12.- Various suboptimal climb-out strategies compared with the optimal. (a) Sketch of speed-altitude profiles; (b) fuel expenditure above optimal; (c) sketch of speed-altitude profiles; (d) change in climb-out fuel cost for various climb-out angles on nonturning paths.

The results are shown in figure 12(b). Let us first consider an initial 3° climb. The additional fuel is between 10% and 28% over the optimum, which gives 285 lb of additional fuel for a 180° turn. If we climb at a slower rate of 500 ft/min, the extra fuel cost is about 4%, or 36 lb, for the 180° turn. The best approximation of an optimal turning climb-out is an initial horizontal flight. Here the additional fuel consumption is primarily a result of the incorrect bank-angle schedule rather than the incorrect climb angle, which is an approximation of the slightly varying singular γ. This is further illustrated in figures 12(c) and 12(d) for a nonturning flightpath, where we plot the additional fuel when we change the climb angle from the average singular γ. Over a range of 0.04° the fuel consumption deviates from the optimal by only 0.1 lb, and it is fairly insensitive for errors of ±0.15° from the singular γ. Considering these results, we can say that the most important fuel-saving features of the optimal climb-out are the initial horizontal turn and acceleration up to the singular speed, which are then followed by a climb at singular γ.

We can make a similar investigation of the turning descents. The h-v profiles considered are shown in figure 13(a). We descend on a flightpath angle that is the average singular-arc descent angle. At a certain altitude we reach a speed of 250 knots IAS. At this point we select the varying flightpath angle that will hold this airspeed. At a certain point we must change our flightpath angle to the final one, γ_f, and at a different point we must begin the turn at maximum bank angle in such a manner that the desired heading and final speed are reached simultaneously. To find these two critical points without trial and error, the path must be integrated backward from the final altitude and heading.

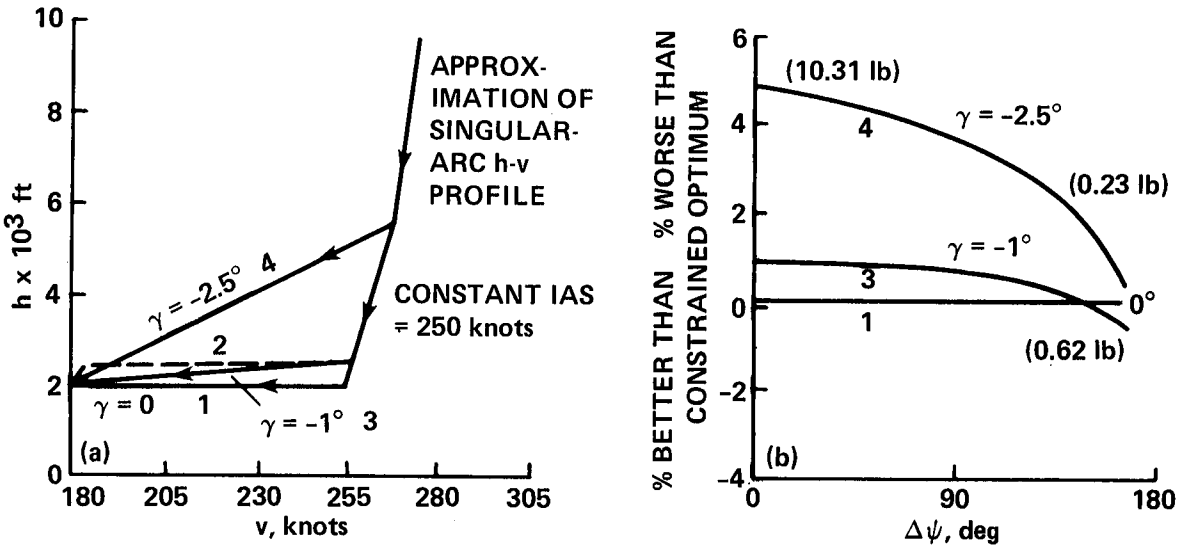

Figure 13.- Optimal versus suboptimal descents. (a) h-v profiles; (b) fuel comparison of suboptimal descents with optimal descents having level turns.

To interpret the results properly, it should be noticed that the optimal descent flightpaths with which we are making the comparison are those that have a level final turn (fig. 13(a), curve 1). We stated earlier that for large turns, in which γ was less constrained, to a 0° maximum and a -4° minimum, it was optimal to begin the level turn at a higher altitude than the final altitude and to finish the turn at -4° to reach the desired final altitude and speed (fig. 13(a), curve 2).

We will compare various suboptimal descents in which the only change is the flightpath angle of the final turn (see fig. 13(b)) with optimal descents that have a level final turn. For the descent that mimics the optimal descent constrained to a level turn most closely (curve 1 in figs. 13(a) and 13(b), final flightpath angle = 0°), the suboptimal performance is within 0.2% for all heading changes. A final descending turn (curves 3 and 4 in figs. 13(a) and 13(b)) will usually result in an increased fuel use. For large turns and a small descent angle γ_f (curve 3 in figs. 13(a) and 13(b)) the trend reverses, since this approximates better the optimal turn of curve 2 in figure 13(a).

5. RESULTS FOR CAPTURE FLIGHTPATHS

Nonturning flight without Speed Constraint

Figure 14 shows altitude-speed profile, flightpaths, and controls for flight on nonturning flightpaths, which consist of nothing but singular arcs. For completeness, these profiles are shown to zero altitude. Figure 15(a) shows the altitude-speed profiles for nonturning flight that are derived from the general singular-arc formulation by setting $\lambda_y = \lambda_\psi = 0$. For the purpose of cross-checking, these profiles were derived twice, once from the general formulation and once from the simpler formulation for nonturning flight. The first portion of the climb is performed at maximum thrust. The altitude-speed curves have a first corner when the thrust begins to decrease. During the entire varying-thrust portion of the flightpath, the thrust is slowly reduced, until it is zero. At this time, a second corner of the altitude-speed curves occurs and the almost constant-flightpath-angle descent at zero thrust begins.

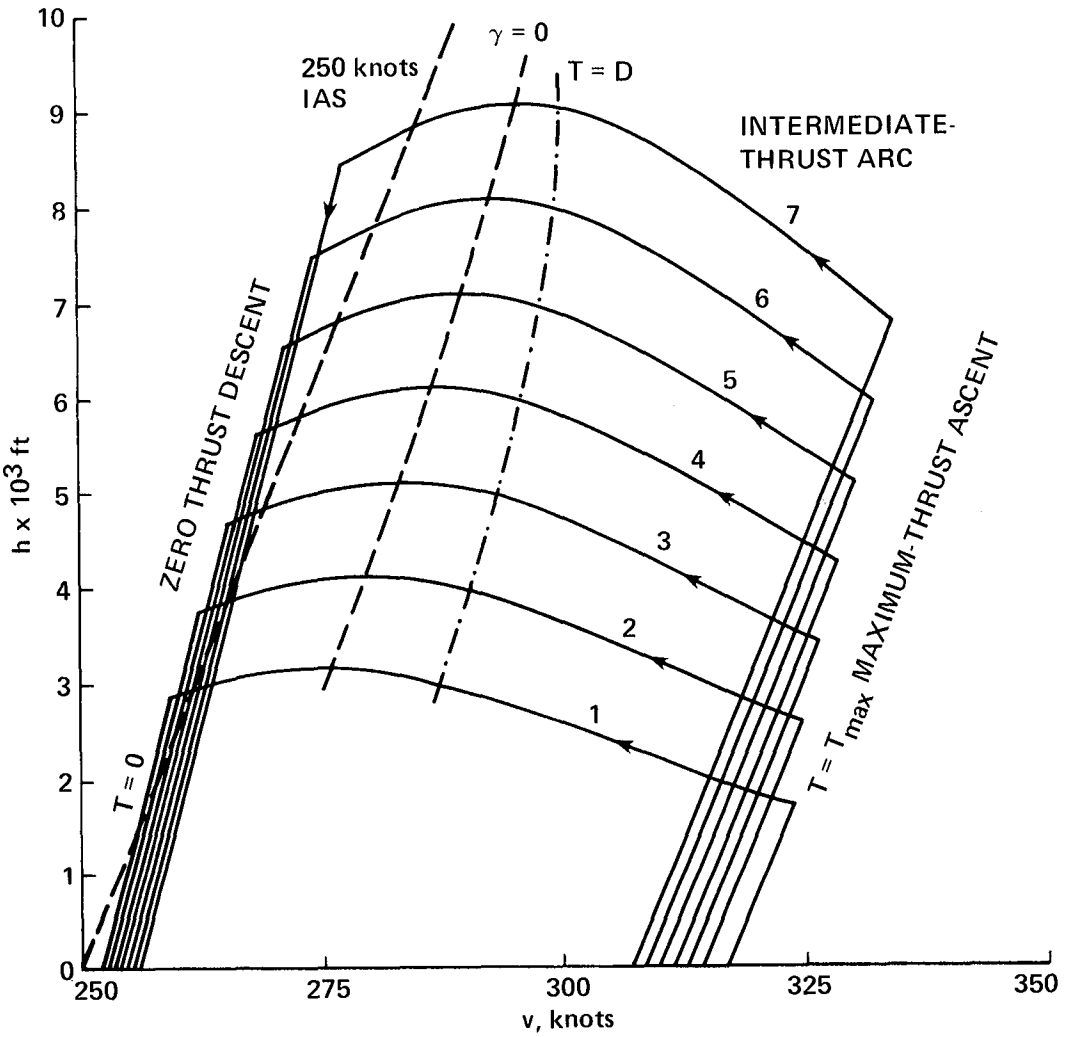

(a) Altitude-speed profile for flight on the singular-γ arc.

Figure 14.- Straight-line, singular-arc flightpath and controls.

The parametric curves of the $\gamma = 0$ condition and of the $T = D$ condition are also shown on the altitude-speed diagram. These two curves tend to converge at higher altitudes, but they do not intersect over the altitude range considered, which means that only finite-length flightpaths are generated.

The flightpath profiles and controls plotted against the horizontal path-length are shown in figures 14(b)-14(d). The origin of the x-axis corresponds to the $T = D$ point on the flightpath. The paths (fig. 14(b)) have nearly constant flightpath-angle ascents, followed by a steep climb, a variable-γ segment, and a nearly constant-γ descent. The thrust (fig. 14(c)) is at its maximum value for the initial almost constant-γ climb, which is followed on the variable-γ segment by a smoothly decreasing thrust. On the final descent the thrust is zero. The flightpath (fig. 14(d)) has an almost constant flightpath angle climb followed by a steep ascent to reduce speed. This "zoom climb" aspect of the flightpath is less pronounced for longer flightpaths. The steep ascent is followed by a gradual reduction in flightpath angle from climb to descent. When the thrust reaches zero, a small step reduction of flightpath angle occurs, which is followed by an almost constant-γ descent.

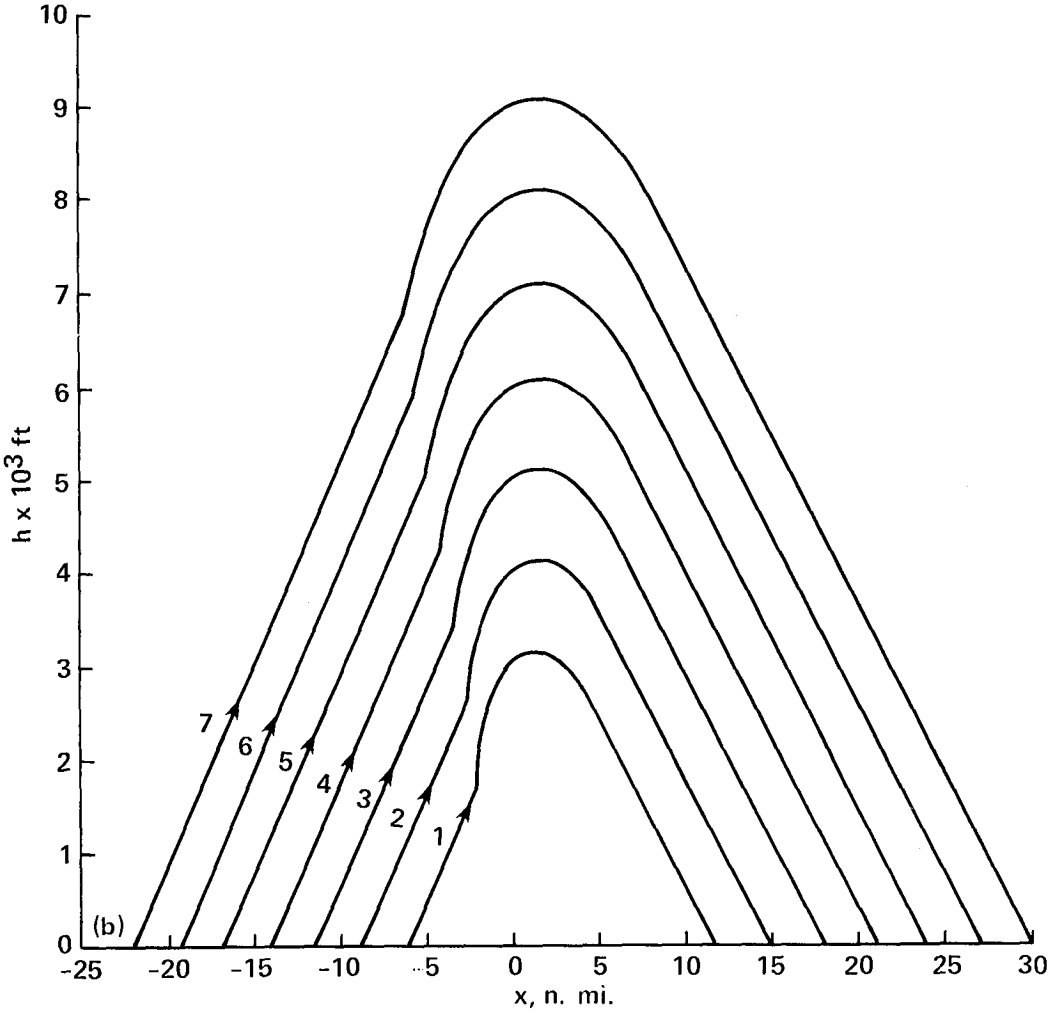

(b) The flightpath.

Figure 14.- Continued.

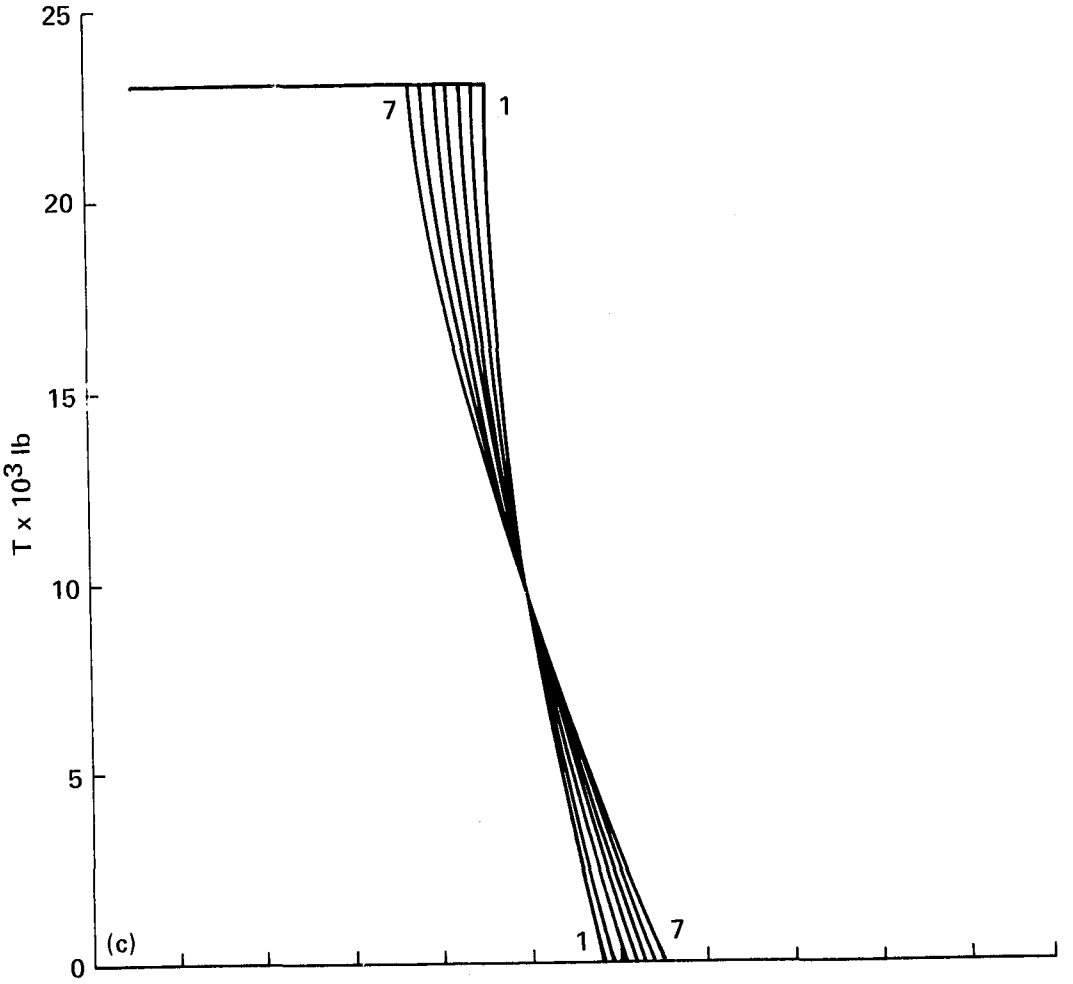

(c) Thrust.

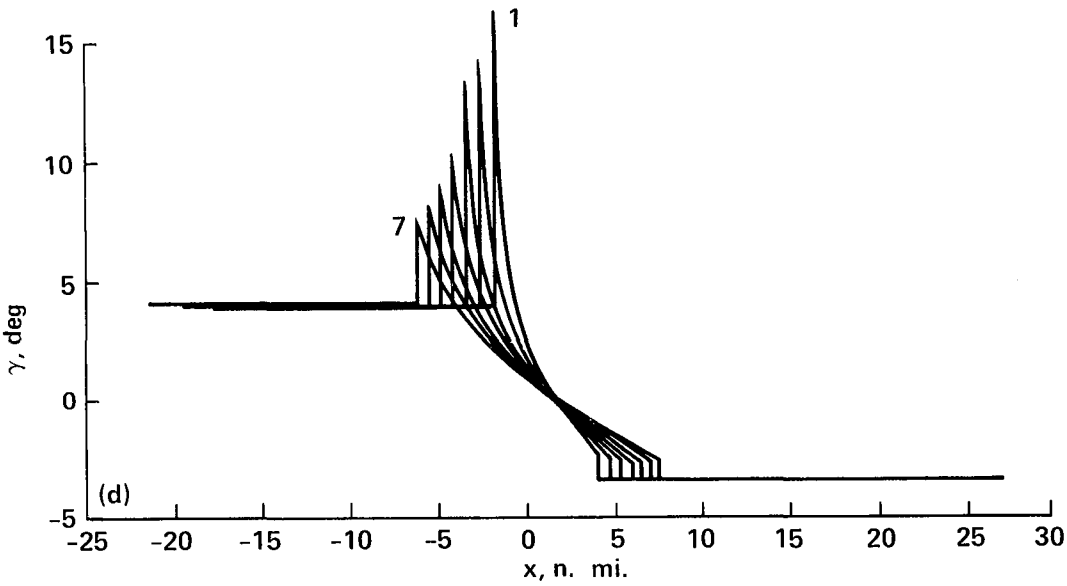

(d) Flightpath angle.

Figure 14.- Concluded.

Steps in the singular γ are caused by the discontinuity of terms containing T which appear in equation (69). In figure 14(d) the flightpath angle briefly exceeds the constraint of $\gamma_{max} = 5°$. This is allowed for computational convenience. From the principle "the fewer the constraints the better the optimal performance," it just means that the optimal system will have an advantage (of less than 0.2% as we shall see later) when compared with a suboptimal one in which the constraints are observed.

We will now discuss figure 15 and discuss the results for an optimal nonturning flightpath, which starts and ends at an altitude of 2,000 ft and at true airspeed of 250 knots. Figure 15(a) shows the altitude-speed profiles, figure 15(b) the altitude profile, and figure 15(c) the speed profile. The controls are shown in

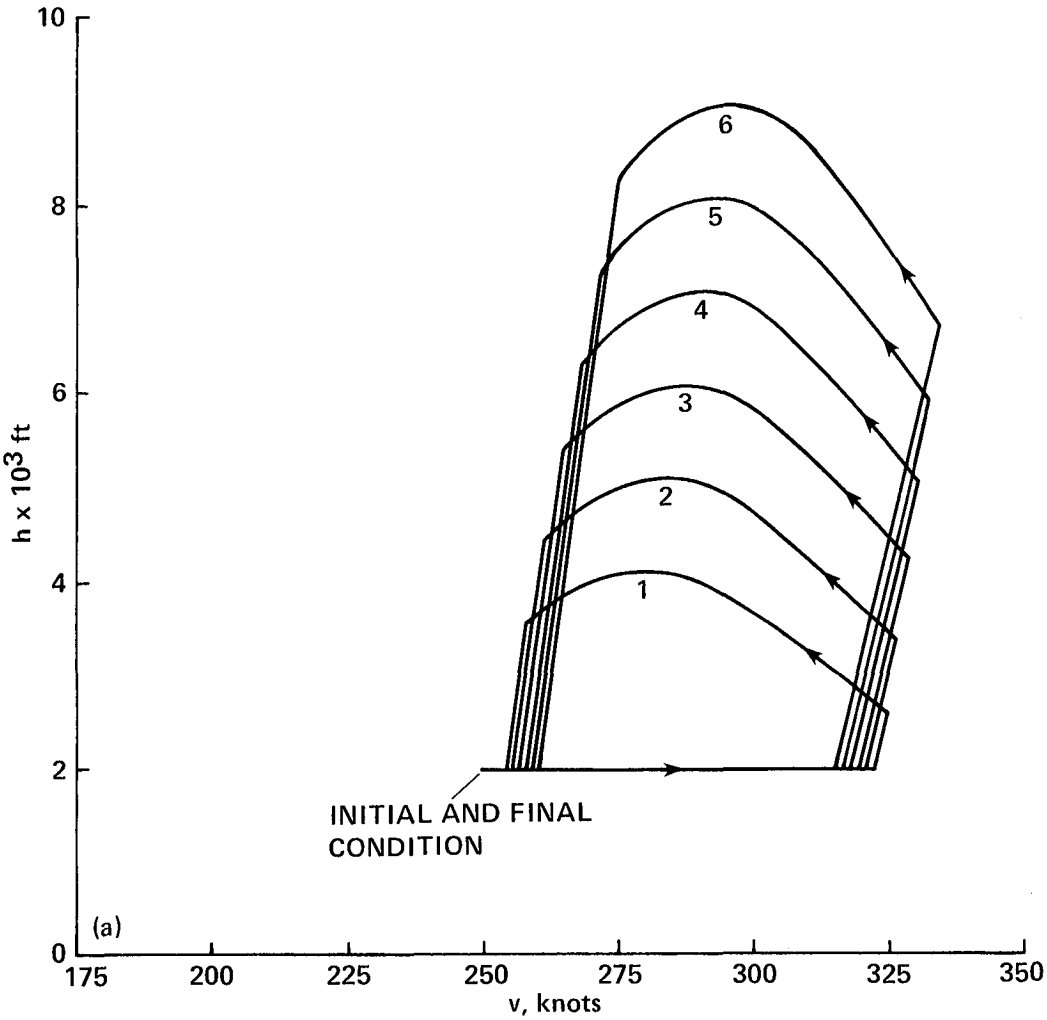

(a) Altitude-speed profiles.

Figure 15.- Minimum fuel nonturning flightpath.

figures 15(d) and 15(e). The singular arc is in all cases preceded by a horizontal accelerating path at maximum thrust and is followed by a brief horizontal decelerating path. A minor exception is the shortest path, No. 1, which has some thrust reduction in the horizontal accelerating portion of the flightpath (dashed line in fig. 15(d)).

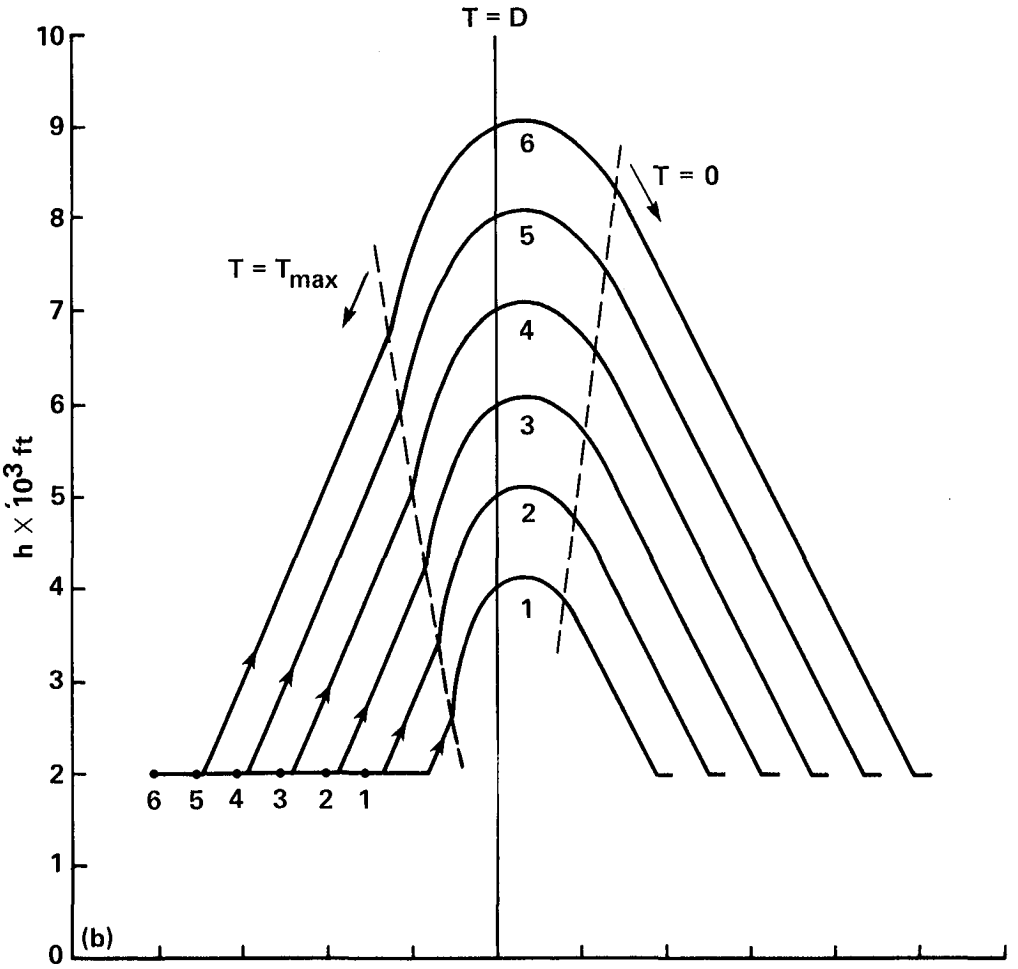

(b) Altitude profile.

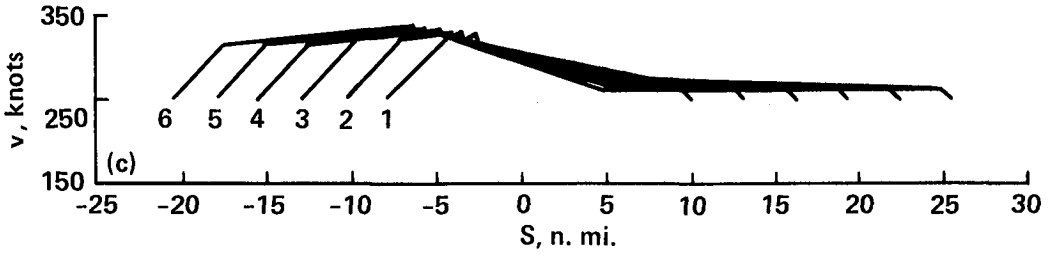

(c) Speed profile.

Figure 15.- Continued.

Strictly speaking, the flightpaths shown in figures 15(a)-15(e) are not optimal because of the restrictions on γ off the singular arc, which have not been introduced optimally. Figure 15(f) shows the altitude profiles of flightpaths that have specified $\gamma_{max} = 5°$ and $\gamma_{min} = -4°$ for both the initial and final portions of the flightpath. The only end condition different from those in figures 15(a)-15(e) is that the final speed is 180 knots, rather than 250 knots, to result in a longer final climb. The fuel consumed for these optimal flightpaths was plotted (not shown) versus distance and compared with a plot of identical flightpaths that have initial final horizontal segments. The purpose of such a plot instead of direct comparison was to avoid having to match the lengths of the flightpaths as well as the speeds and

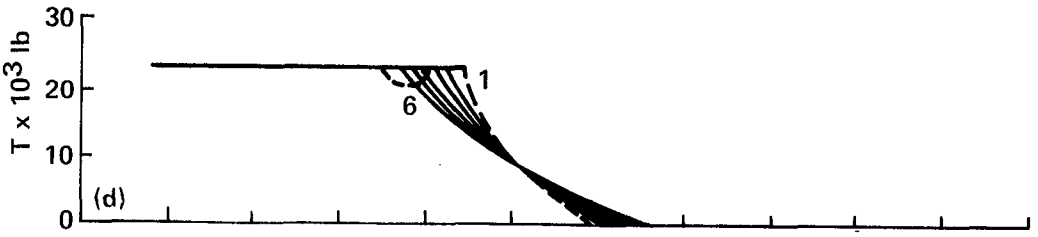

(d) Thrust control.

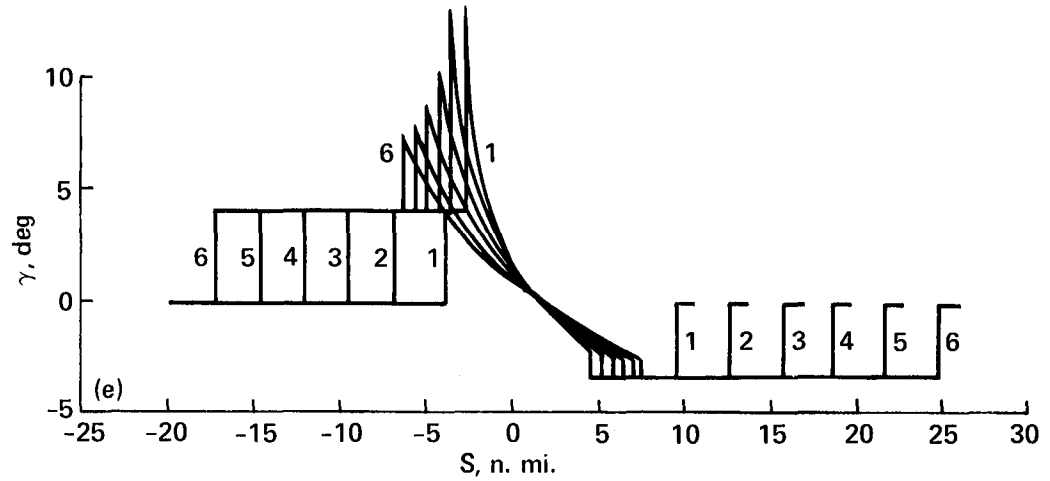

(e) Flightpath-angle control.

Figure 15.- Continued.

altitudes. It was found that the paths of figure 15(f) consume about 4 lb less fuel than the equivalent flightpaths with horizontal initial and final segments (which is 0.65% for the shortest and 0.28% for the longest path). We conclude that it would be of negligible benefit to introduce the restrictions optimally. When the maximum altitude and fuel consumption of the paths of figure 15(f) are plotted against the path length the relationships turn out to be nearly linear.

What is the effect of neglecting the change in weight? In section 2, we took care of the weight change during the long cruist (flight above 10,000 ft) by using a different but constant weight for ascent and descent. In this section we assumed that the weight did not change. This appears to be a reasonable approximation, since the actual weight change for the longest path considered was only 0.025%. A simple improvement of the results can be obtained by updating the weight-dependent drag for the fuel via equations (C2) and (C10) and updating W wherever it appears in the equations without, however, defining W as a new state variable. This includes changing k_1 and k_5 as a function of weight, as discussed below equation (9c). This method has been successfully used in reference 1, and its success is based on the slow change of W relative to all other state variables. To test our assumption that using constant weight has negligible effect on the results, we implemented the method of reference 1. The results for the example shown in figure 15(f) are the following. Starting with the same initial conditions and adjoint variables at the $T = D$ points the variable weight trajectories are slightly longer and take somewhat more fuel. The fuel used per nautical mile is on the average 0.016 lb/n. mi. more than for the W = constant flightpaths. This is expected, since we are beginning the computations at the $T = D$ point with W = 150,000 lb; the initial climb-out

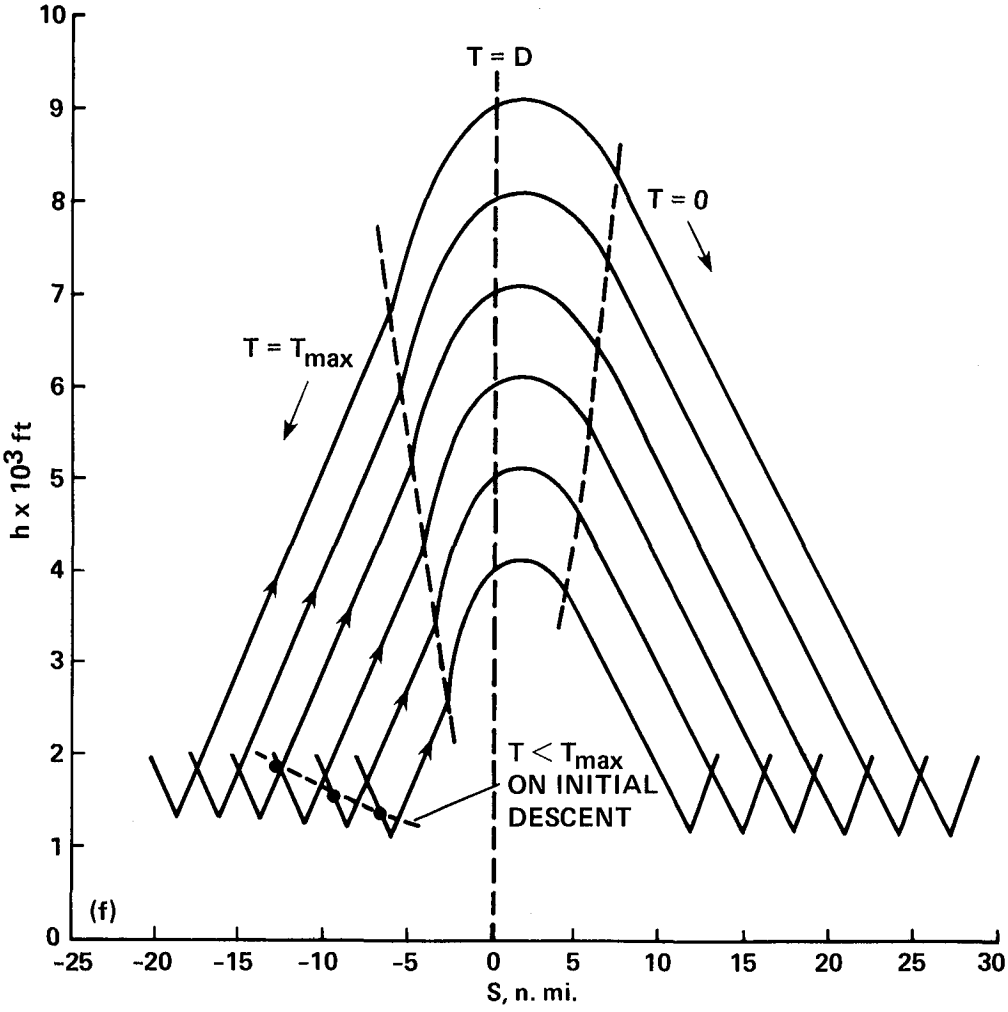

(f) Altitude profiles for special paths with $\gamma_{min} = -4°$, $\gamma_{max} = 5°$, $v_o = 250$ km, $v_f = 180$ km.

Figure 15.- Concluded.

weight is higher and it takes more fuel to get to the T = D point on the trajectory. The reduction in weight beyond the T = D point and the associated smaller amount of fuel used does not compensate for the larger amount used in climb-out, since most of the remaining flightpath is at idle thrust and the weight reduction is minimal. On the scale of our braphics, however, the flightpaths and controls are indistinguishable from the constant-W flightpaths and are not shown. As a check on the calculations we printed out the Hamiltonian; it should be zero, but it was not. For the correct formulation (W-constant) most of the error in the Hamiltonian was due to finite step size of the integration. In fact, as the integration-time interval Δt was reduced from 0.05 sec to 0.005 sec for a special test run, the Hamiltonian at ±40 sec from the start of the integration reduced by a factor of 10 without affecting the trajectory. (Reducing Δt and comparing H's was our usual check for programming errors). When the variable weight was introduced, however, the Hamiltonian was larger by a factor of 10 than for the W = constant formulation and it practically did not decrease for decreasing Δt. A general investigation of the effects and errors of such approximations may be an interesting research topic.

Figure 16 shows the comparison in fuel efficiency for the optimal nonturning capture flightpath of figures 15(a)-15(d) with various suboptimal procedures. The first comparison (curve a, fig. 16) is with a constant-speed (250-knot), constant altitude (2,000-ft) cruise. Here, the greatest amount of extra fuel is required for the longest flightpath. This is over 10% (or 155 lb of fuel) for a 45-n. mi. flightpath. The second comparison is with a constant altitude flightpath with a speed profile, which approximates that of an optimal constant-altitude flightpath (see ref. 15). Adding this speed profile to the constant-altitude path reduces the extra fuel consumption by about 4% over the range of distances considered (curve b). The third comparison (curve c), which will be discussed in the next paragraph, is with a simple suboptimal algorithm, which includes both speed and altitude changes. As can be seen, when both altitude and speed changes are considered, the performance becomes near optimal. The percentages between the curves indicate the costs of various simplifications. We notice that the cost incurred by not climbing increases with the length of the flightpath.

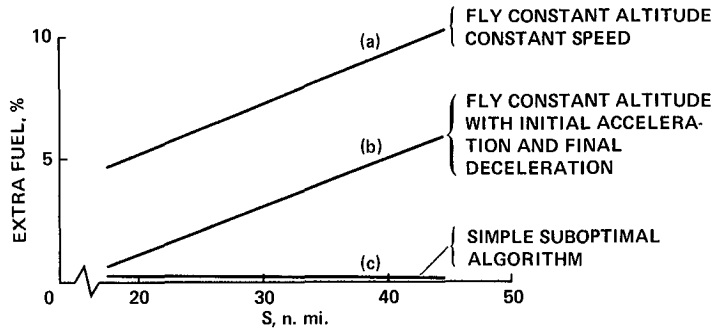

Figure 16.- Fuel efficiency comparison for nonturning flightpaths.

The next question that must be asked is how closely the optimal results can be approximated with an easily implemented on-board, suboptimal algorithm. The suboptimal algorithm is described in appendix B. Briefly, it uses characteristic features of the optimal flightpath. Two of the primary features are climb at maximum thrust at the average of the optimal climb angle and descent at zero thrust at the average of the optimal descent angle. The complete suboptimal command structure is schematically shown in figure 17. By comparison with figures 15(d) and 15(e) it can be seen that it is much simpler than the optimal command structure.

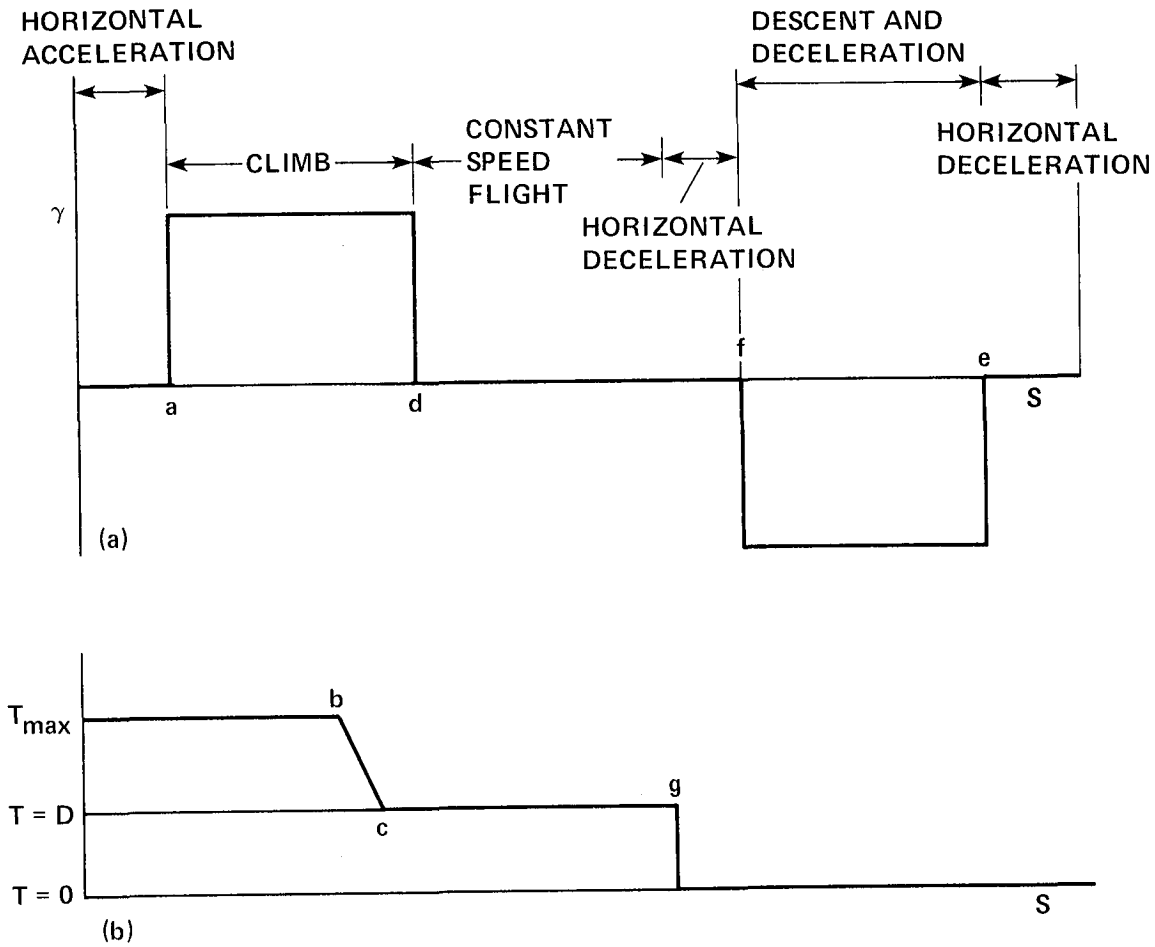

Figure 17.- Suboptimal command sequence for nonturning flight against distance along the path (see appendix B for details). (a) Flightpath angle; (b) thrust.

In figure 18 the heavy line gives the decrease in performance of the suboptimal algorithm, when compared with the optimum (also shown as curve c in fig. 16). The performance is within 0.2% of the optimum, with a slight improvement for the longer paths. Since only slightly more fuel is consumed when flying according to the suboptimal algorithm than according to the optimum, most of the improvement shown in figure 16 can be realized in a simple on-board system. Figure 18 also shows the slight additional fuel consumption when deviating from the average of the optimum climb angle and the average of the optimum descent angle, as identified by the pair of numbers opposite each curve that correspond to a nonturning capture path.

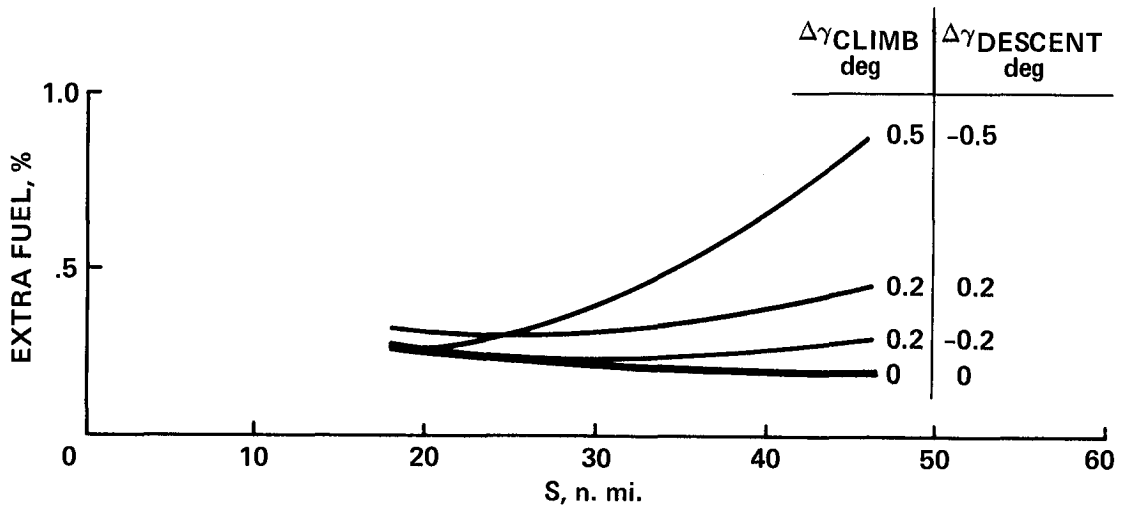

Figure 18.- Performance of suboptimal nonturning flight: $\Delta\gamma$ = change in γ from the average of the optimum climb or descent angle.

Nonturning Flight with Speed Constraint

Figure 19(a) shows the altitude-speed profile. It is the same profile as that shown in figure 15(a), with the high-speed portion cut off by the speed limit of 250 knots IAS. The flightpath profiles, speed profile, and controls plotted against the horizontal distances are shown in figures 19(b)-19(e). In this case, the thrust-equal-drag point is not at $S = 0$, but from equation (42) it is where $\gamma = 0$ at the peak of the altitude profile. We notice that thrust and flightpath angle change more gently than in the nonspeed-limited path of figure 15. The speed-limited paths were compared, with respect to maximum altitude and fuel consumption, with nonspeed-limited paths of the same lengths. This was done not by solving the two-point boundary-value problem, but by plotting curves of maximum altitude versus distance and total fuel consumed versus distance for both types of paths, and by interpolating between the curves (not shown). Over a range of 29 to 52 n. mi. the speed-limited paths achieved a maximum altitude about 1,000 ft lower than the nonspeed-limited paths. The speed-limited paths used between 20 and 50 lb more fuel than the nonspeed-limited paths of the same length. The increase in fuel used was linear with increased distance, but the percentage increase was approximately a constant 3.7%.

Turning Flight

Capture trajectories without speed constraint— Turning flight will now be discussed. Since a capture trajectory ideally captures the centers of the localizer and elevation beams of an Instrument Landing System, the final turn will include a speed reduction to 180 knots IAS, which is the landing speed with the flaps extended. Only the longest and the shortest flightpaths that have the turn-straight-turn characteristic will now be examined. The longest flightpaths have the $T = D$ point at the 7,000-ft altitude and the shortest ones have the $T = D$ point at 4,000-ft altitude. Paths that have various combinations of large and small turns at either end were computed. We will discuss four sets of flightpaths: long and short flightpaths with the full range of initial turns, and long and short flightpaths with the full range of final turns. The initial states and adjoint variables for each set were chosen such that some of the examples have turns on both ends and others do not. All

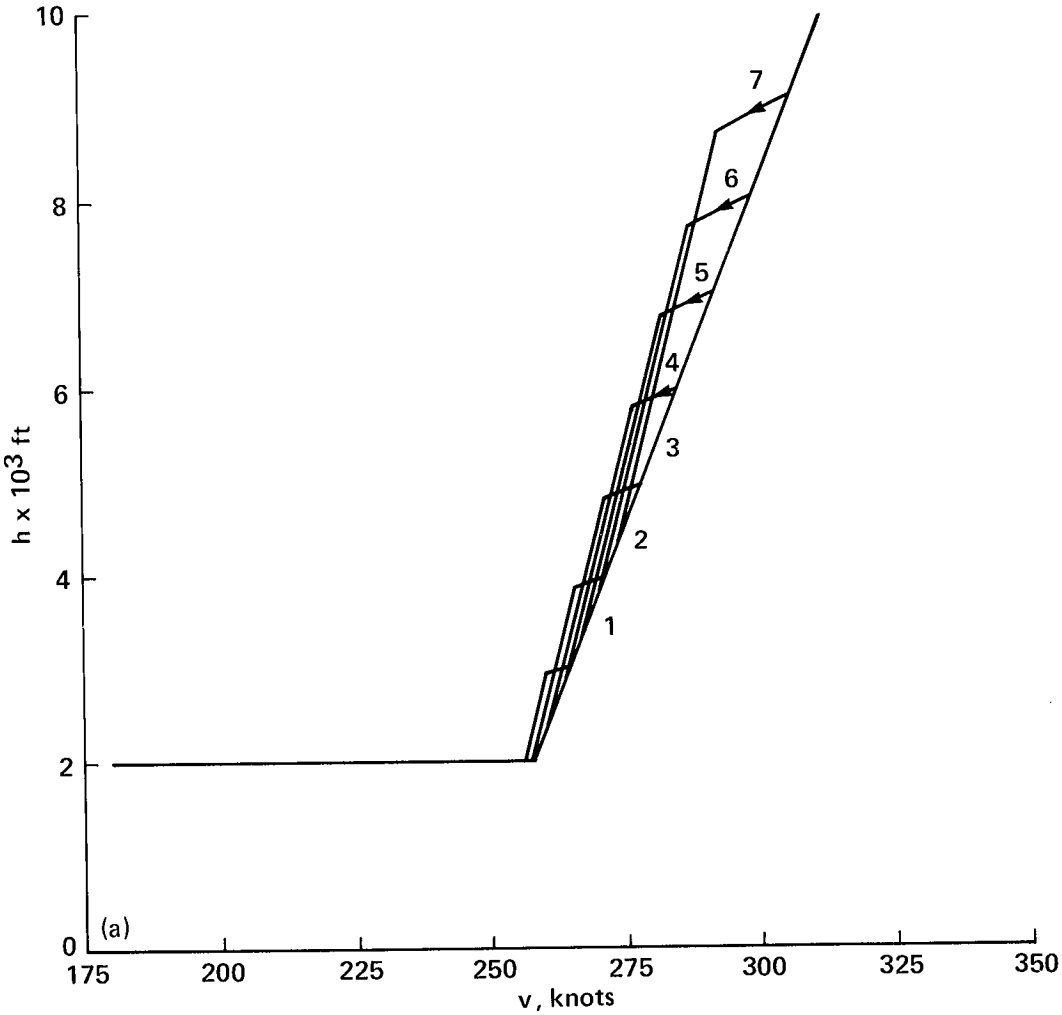

(a) Altitude-speed profile.

Figure 19.- Minimum-fuel, nonturning, speed-limited flightpaths.

flightpaths start at $h = 2{,}000$ ft and $v = 250$ knots IAS and end at $h = 2{,}000$ ft and $v = 180$ knots IAS. Unless noted otherwise, turns off the singular arc were forced to be level by restricting γ to be

$$\gamma_{max} = \begin{cases} 0.001^\circ & \text{for climb} \\ 0.0^\circ & \text{for descent} \end{cases} \qquad \gamma_{min} = \begin{cases} 0.0^\circ & \text{for climb} \\ -0.001^\circ & \text{for descent} \end{cases}$$

Long terminal-area flightpaths that have initial turns with heading changes between 0° and 180° and final turns between 11° and 67° will be discussed first (see fig. 20(a)). The individual paths are labeled 1 to 5 in figure 20(a). All initial turns are predominantly level turns, which are almost completed when the climb begins. The turns have similar characteristics that have been reported in reference 8 for level flightpaths. Small turns are made at maximum thrust (fig. 20(d)), with a bank angle that is slowly decreasing toward zero (fig. 20(c)). Large turns either start with zero or intermediate thrust, which builds up toward the maximum thrust as the

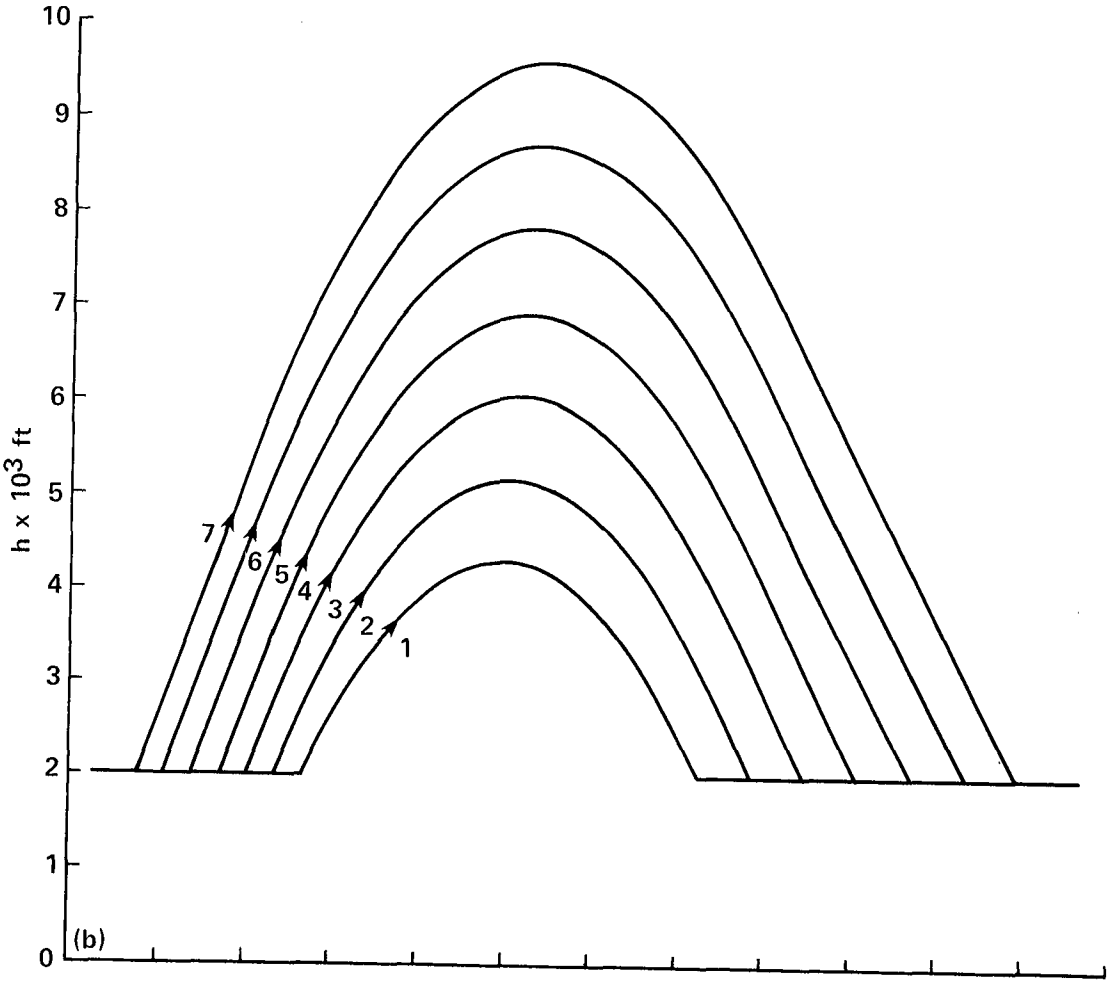

(b) Altitude profile.

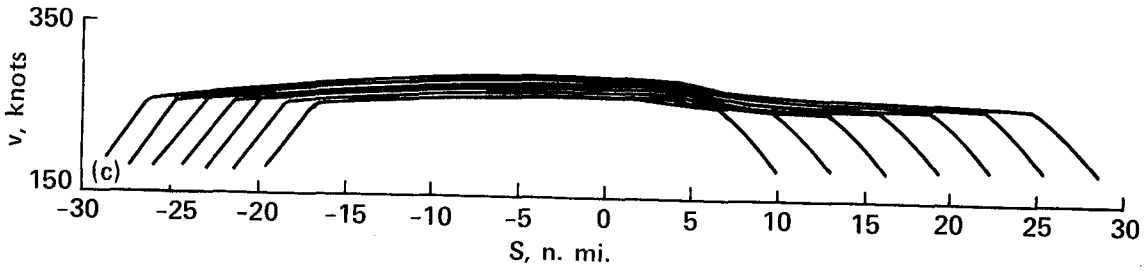

(c) Speed profile.

Figure 19.- Continued.

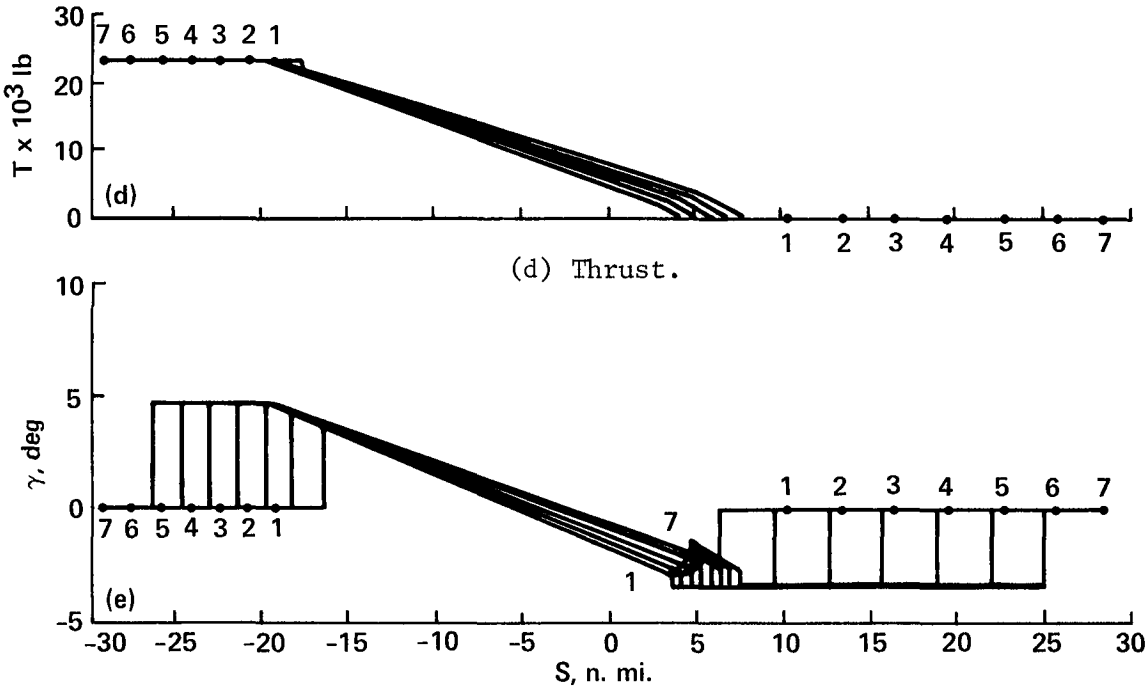

(d) Thrust.

(e) Flightpath angle.

Figure 19.- Concluded.

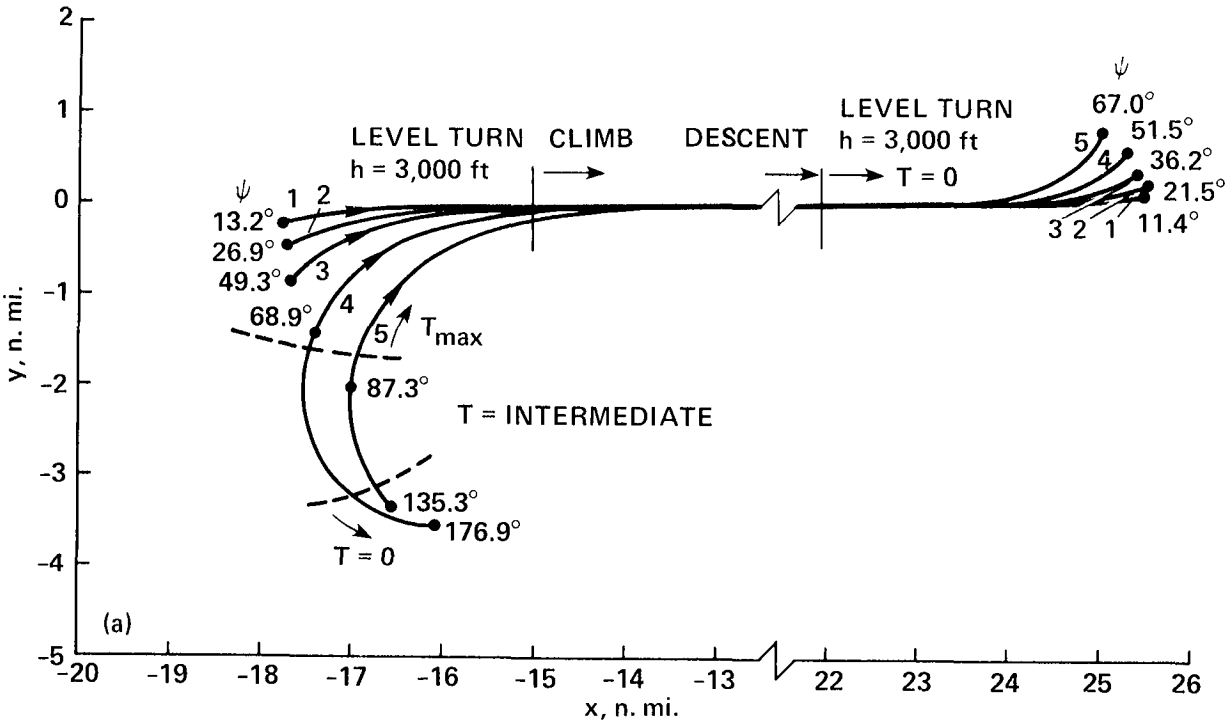

(a) Projection of the flightpaths on the x-y plane.

Figure 20.- Optimal long terminal area flightpaths with initial turns up to 180°.

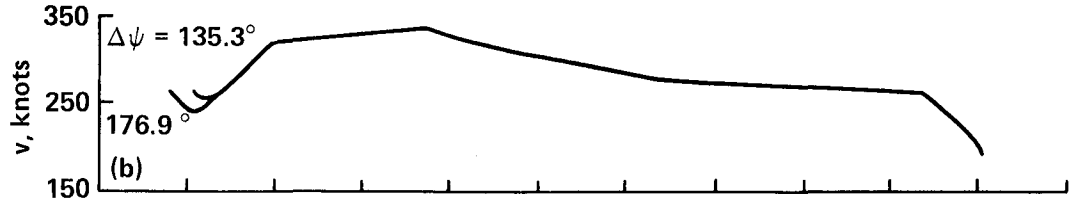

(b) Speed profile.

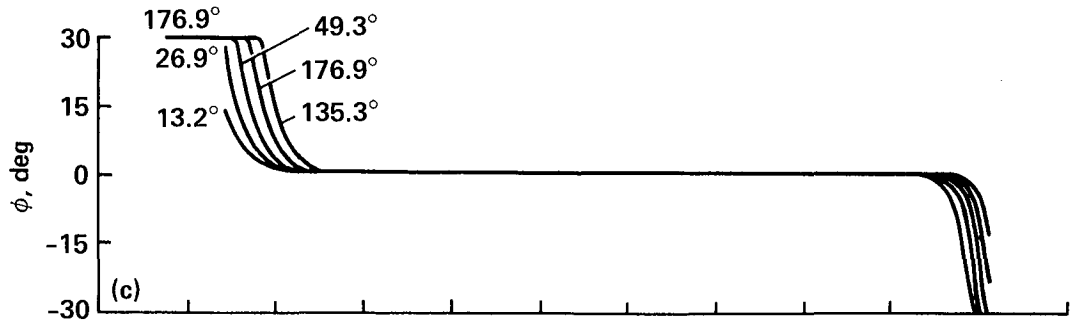

(c) Bank angle.

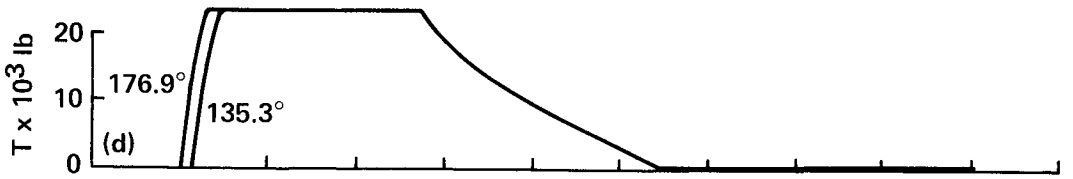

(d) Thrust.

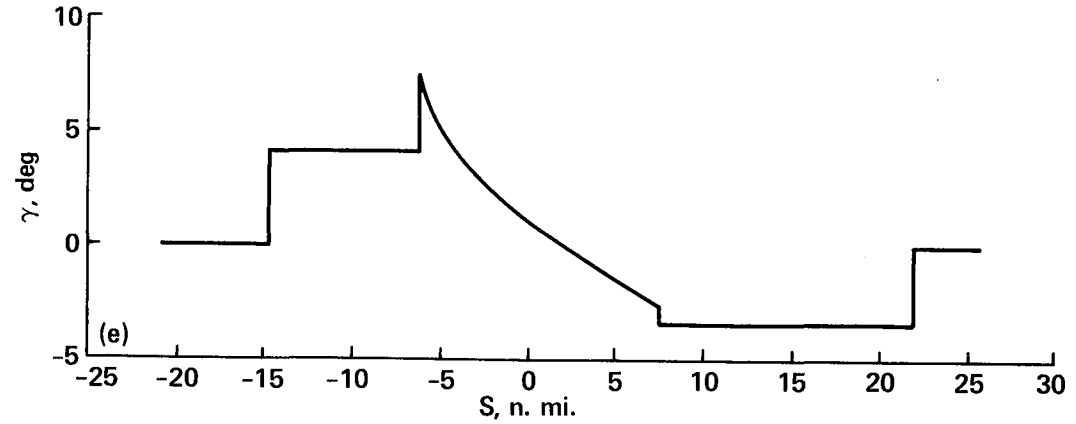

(e) Flightpath angle.

Figure 20.- Continued.

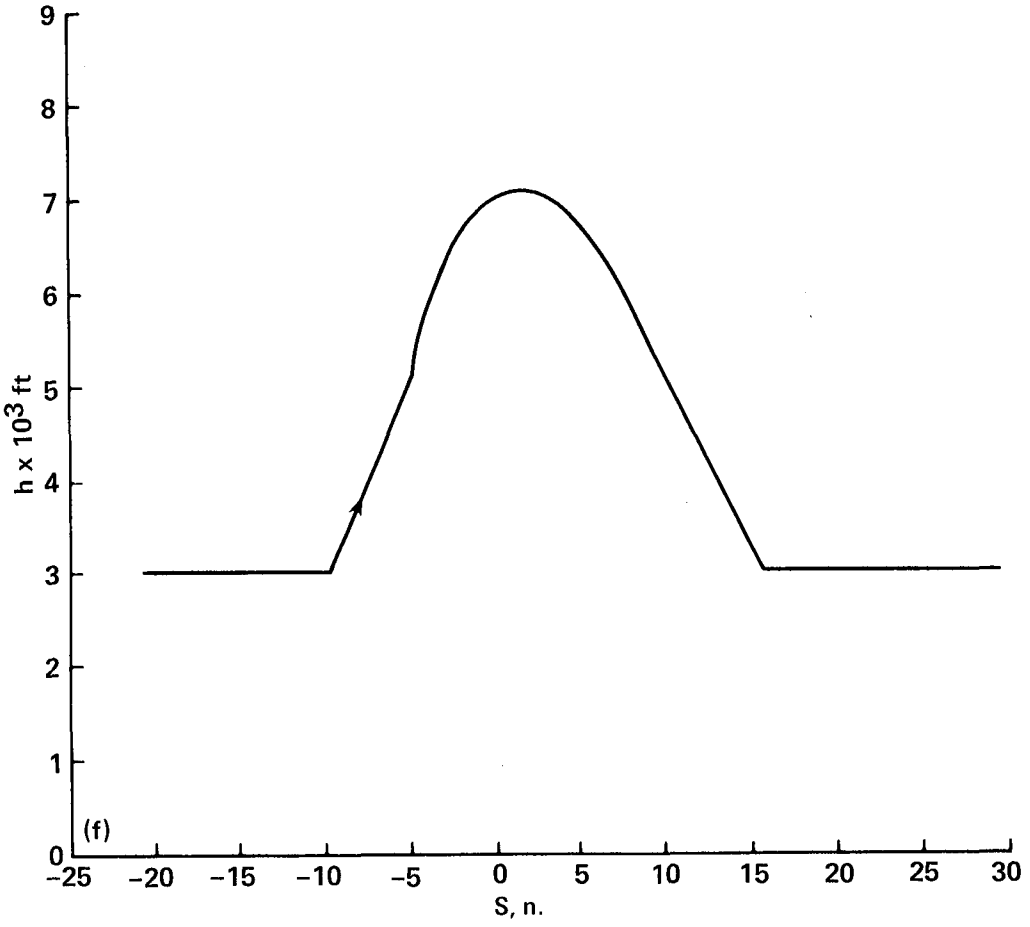

(f) Flightpath profile.

Figure 20.- Concluded.

remaining turn becomes less than 90° (fig. 20(d)). Depending on the terminal point chosen, the same extremal can either be a large turn (e.g., 176.9°) or a small turn (e.g., 68.9°), since the speed of 250 knots IAS is achieved at those two points (see the speed profile in fig. 20(b)). The singular flightpath angle is practically independent of the turns (fig. 20(e)), and the thrust is practically identical for most flightpaths, except for the initial low thrust for deceleration in the initial portion of large turns (fig. 20(d)). The flightpath profile (fig. 20(f)) is practically the same for all flightpaths, and, except for the starting and final altitudes, is the same as that in figure 15(b), curve 4, for the nonturning flightpath.

For short flightpaths, shown in figure 21, the initial turns look similar to the initial turns for long flightpaths (compare figs. 20(a) and 21(d)). In this example, there are no final turns. Most of the comments made for the initial turns of long flightpaths apply to the short ones also. The thrust schedule, however, is quite different and never reaches maximum thrust (fig. 21(d)). The importance of this difference will be explored when optimal and suboptimal flightpaths are compared. Here too, the flightpath profile (fig. 21(f)) is the same for all flightpaths, and, except for the starting and final altitudes, is the same as in figure 15(b), curve 1, for the nonturning flightpath.

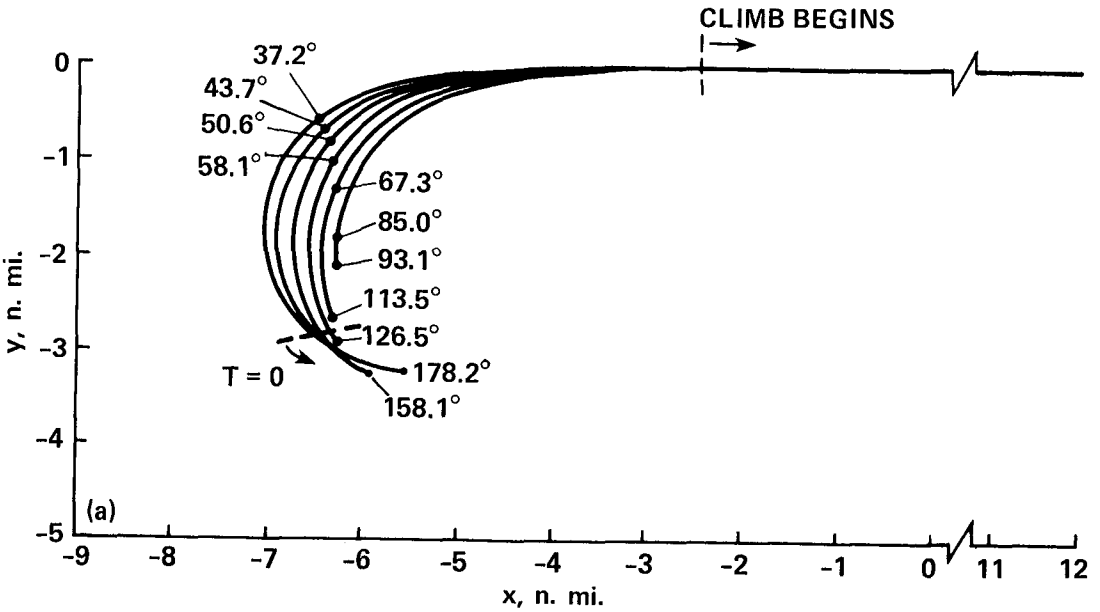

(a) Projection of the flightpaths on the x-y plane.

Figure 21.- Short terminal-area flightpaths with initial turns between 0° and 180° and initial speed 250 knots IAS.

Figure 22 shows the altitude profiles of flightpaths identical to those in figure 21, except that an initial climb was permitted, $\gamma_{max} = 4°$. Hence, the paths begin to deviate from those in figure 21 when (in the backward integration) the optimal control logic requires the flightpath angle to switch to $\gamma = \gamma_{max}$. Here we made no attempt, by adjusting the altitude where we leave the singular arc (point a), to match the initial altitude of 3,000 ft of figure 21. In any case, a comparison with the forced level-turn case of figure 21 cannot be made because we do not solve the two-point boundary-value problem. The largest initial climb is for the largest initial turn, and, even for the largest initial turn, the initial climb is fairly small. Therefore, to avoid complicating the algorithm, this initial climb will not be introduced in the suboptimal algorithm. Physically, the initial climb and resulting deceleration allows a tighter turn, thereby saving fuel.

The next flightpaths to be examined are long flightpaths that have the full range of turns at the end, but none at the start (see fig. 23). Here, a possible second descent was permitted during the final turn after getting off the singular arc by setting $\gamma_{max} = 0°$, $\gamma_{min} = -4°$. This was easier than not permitting it, because, just as in section 2 (discussion of table 2), large level turns could not be produced without running into the bank-angle limit on the singular arc with its associated sharply decelerating zoom climb. (In the suboptimal algorithm, the change in flightpath angle during the final turn will be avoided and the slight additional cost in fuel will be tolerated.) Only the results that are different from the nonturning flight are shown in figure 23. The $\psi = 119.2°$ turn begins its second descent after a level horizontal turn of 95°. The $\psi = 162.9°$ turn begins its second descent after a level turn of $\psi = 90°$. Initial turns are not shown, since

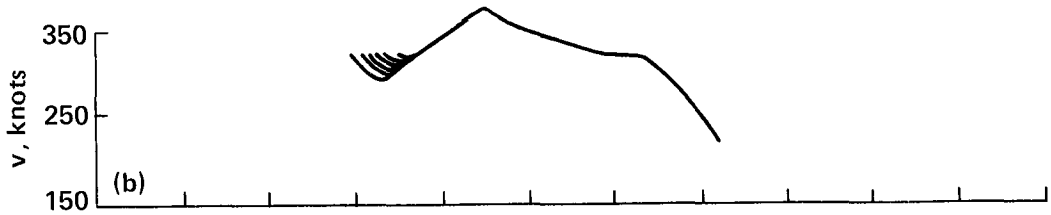

(b) Speed profile.

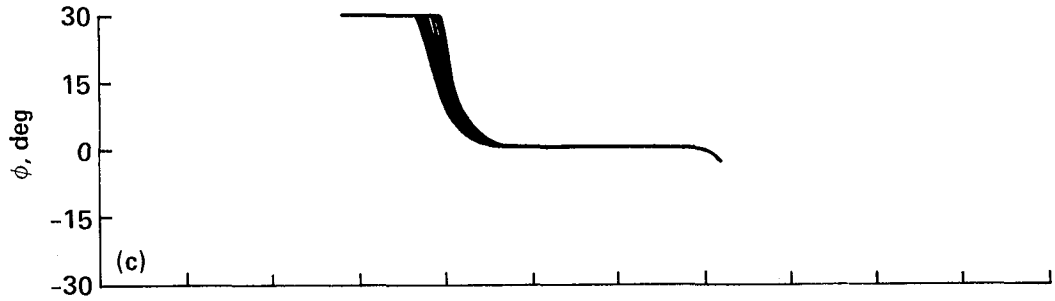

(c) Bank angle.

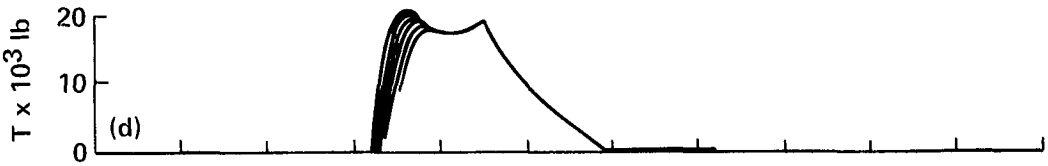

(d) thrust.

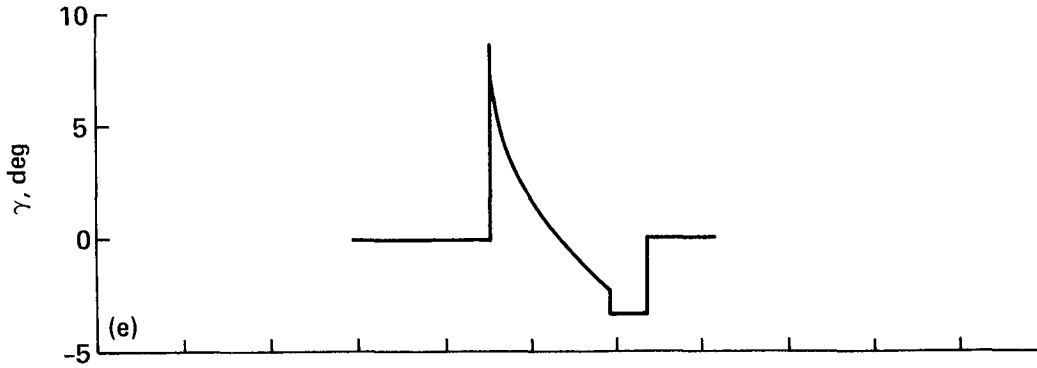

(e) Flightpath angle.

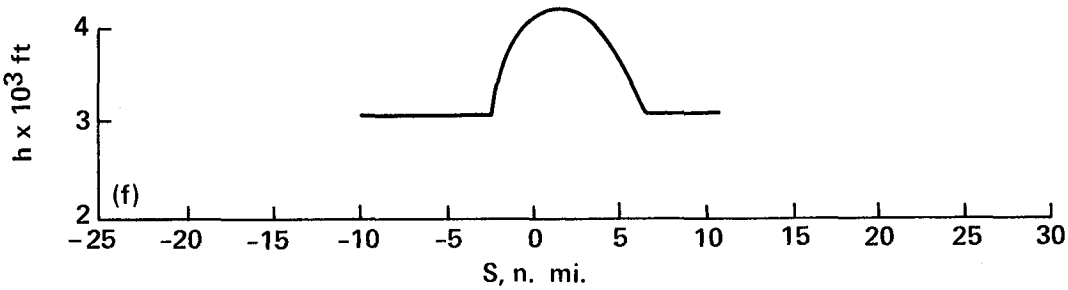

(f) Altitude profile.

Figure 21.- Concluded.

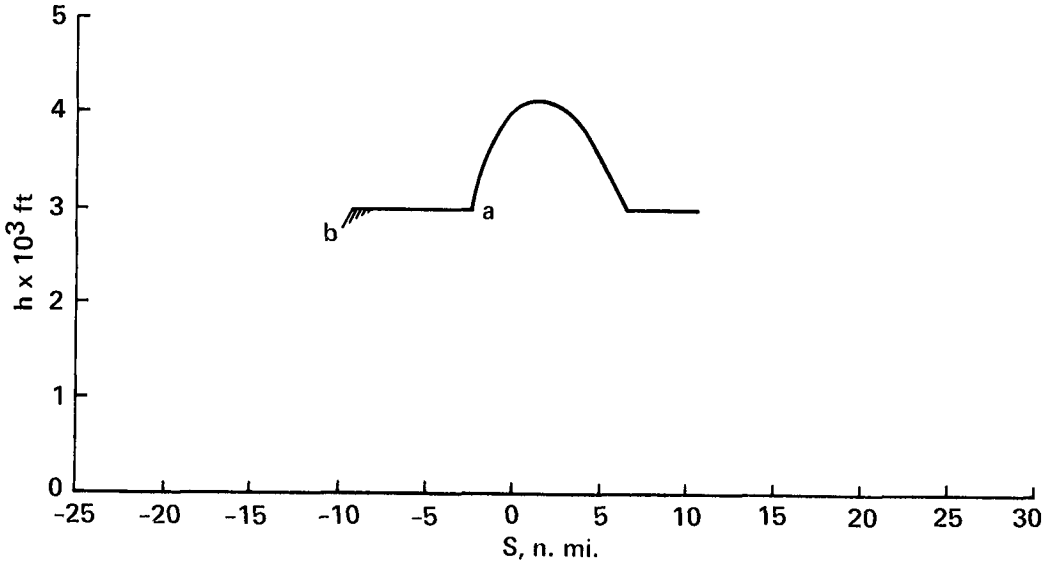

Figure 22.- Altitude profiles for short flightpaths that permit an initial climb at $\gamma = 4°$.

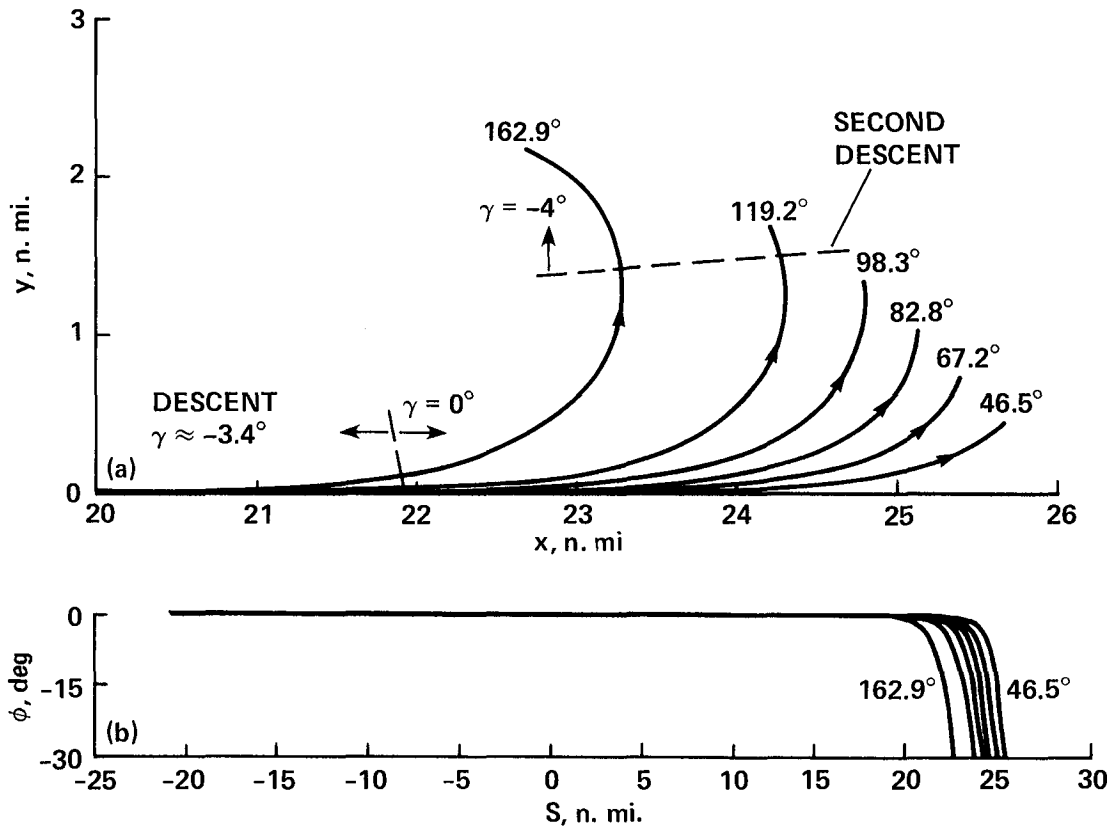

Figure 23.- Final turns for long terminal-area flightpaths: v_f = 180 knots (true). (a) x-y plots of final turns; (b) bank angle.

none occurred for the initial conditions that produced the final turns shown in figure 23. Only the bank angle is shown in figure 23(b), since other controls were essentially the same as that for nonturning flight.

Finally, similar information is given in figure 24 for finall turns of short flightpaths where again $\gamma_{max} = 0°$ and $\gamma_{min} = -4°$. Comparison of figures 23(a) and 24(a) shows that the final turns are quite similar for long and short flightpaths. In figure 24, the initial turns, which have an initial speed of 180 knots true airspeed, are also shown. In contrast to the turns presented in figure 21, which had an initial speed of 250 knots, the initial portions of even the large turns are flown at full thrust, and the thrust is reduced later in the almost nonturning portion of the flightpath (see fig. 24(d)). Here too, the altitude profile (fig. 24(f)) is the same for all flightpaths except for the final portion of the final turn. Also, except for the starting and final altitudes (3,000 versus 2,000 ft), the altitude profile is practically the same as in figure 15(b), curve 1, for the nonturning flightpath.

When observing the overall results for section 3, it is noticed that especially for short flightpaths, the thrust for an initial turn of a given magnitude changes noticeably as a function of the magnitude of the turn at the other end of the flightpath (compare figs. 21(d) and 24(d)). In other words, the turns are not decoupled. However, the bank angles that produce the turns are very similar, independent on the length of the flightpath (see figs. 20(c), 21(c), and 22(c)). Large initial turns start with maximum bank angle that, after a while, slowly get reduced to zero as the heading of the nonturning portion of the flightpath is approached. Small initial turns show the same trend except they begin with less than the maximum bank angle. All the final turns begin with a shallow bank angle, which gradually increases until the final heading or the maximum bank angle is reached. Also, turning and nonturning flightpaths essentially follow the same altitude-versus-distance profiles provided that they reach the same peak altitude.

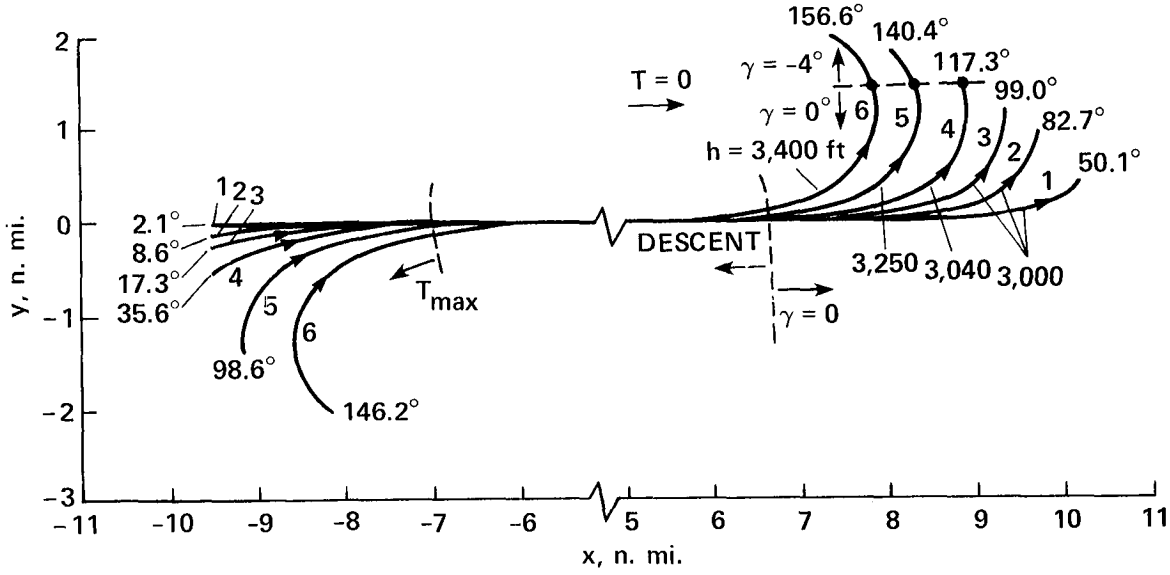

(a) Details of the turns (horizontal profiles).

Figure 24.- Turns for short terminal-area flightpaths: v_o = 180 knots (true), v_f = 180 knots (true).

(b) Speed profile.

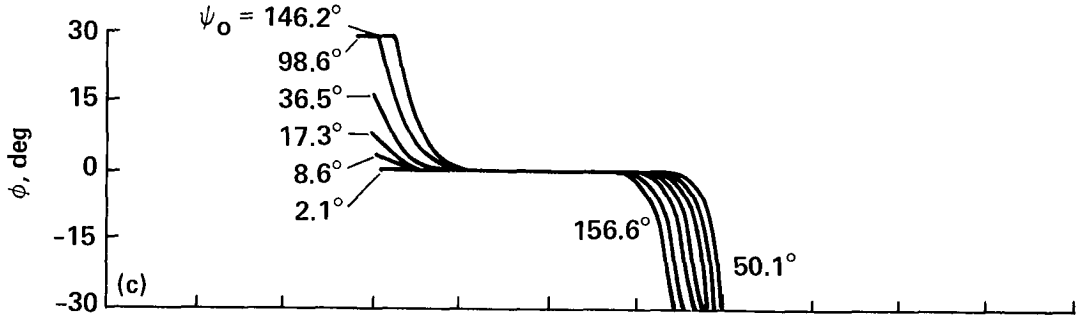

(c) Bank angle.

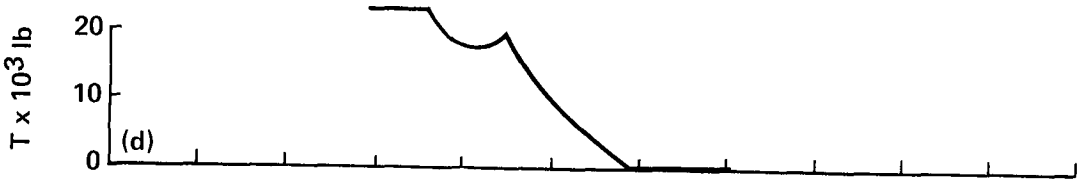

(d) Thrust.

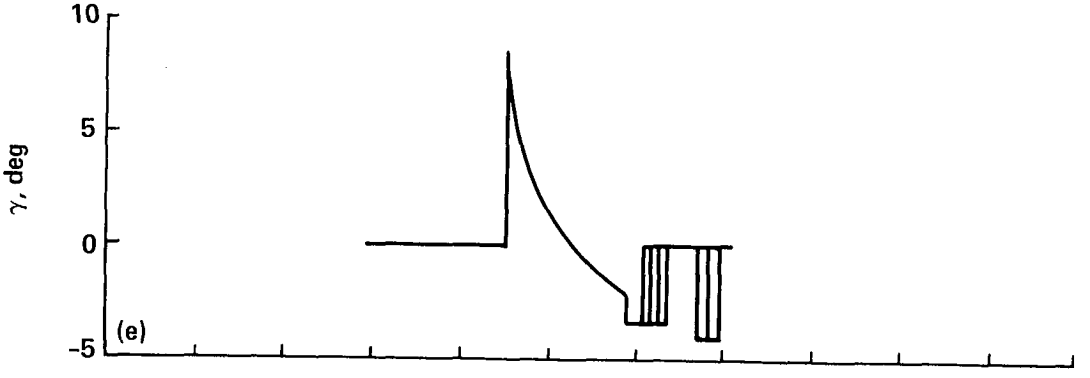

(e) Flightpath angle.

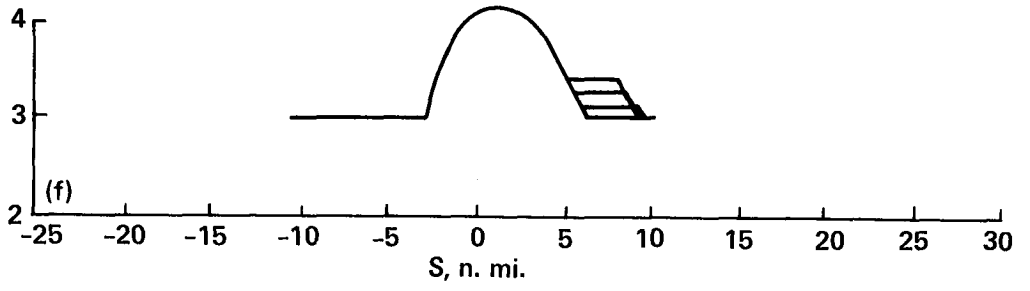

(f) Altitude profile.

Figure 24.- Concluded.

Again the question is asked how can the optimal results be approximated with a simple suboptimal algorithm. The suboptimal algorithms for turning and nonturning flight described in appendix B are identical except for the following additions. For large turns the beginning of the turn is flown at zero thrust until the remaining turn is less than 120°, at which time the thrust is commanded to maximum. Both initial and final turns are flown at maximum bank angle. Because these turns are quicker than the optimal turns there is always a straight-line segment following the initial and preceding the final turns. The turn computations described in appendix B are similar to the "more sophisticated algorithm" described in reference 15.

When compared with the optimal, the resulting performance of the suboptimal algorithm is as expected. For relatively long paths with small turns the performance of the suboptimal algorithm for turning flight is as good as that of the suboptimal algorithm for nonturning flight; for instance, the suboptimal path that matches the end conditions of the optimal turning flightpath, curve 1 of figure 20, is only 0.19% worse than optimal (1,024 lb versus 1,022 lb). The performance decreases slightly for large turns; for instance, the suboptimal path that matches the end conditions of the optimal flightpath with the largest turns, curve 4 of figure 20, is 0.37% worse than optimal (1,346 lb versus 1,340 lb).

For the short flightpath with the largest turning angles, shown in figure 24, which has an initial turn of 146.2° and a final turn of 156.6°, the performance is 2.17% worse than the optimal (738 lb versus 722 lb). This decrease in performance is quite understandable, since the suboptimal algorithm was an approximation of the control commands for longer paths, but the optimal controls of the shorter paths of figure 24 are quite different from those of longer paths. For instance, note that because of the initial altitude of 3,000 ft, and in contrast to figure 20, there is no approximately constant-γ climb portion. Also, in contrast to figure 20, the thrust is maximum in the early portion of the turn and decreases in the latter portion of the turn. The development of a suboptimal algorithm that is a close approximation of the optimal for all flight conditions might be quite complex, and quite possibly not worth the additional complexity.

Capture trajectories with speed constraint— Initial turns for speed-limited flight are shown in figure 25. Final turns are at or below the speed limit and therefore are identical with nonspeed-limited turns; therefore, they will not be discussed here. Figure 25(a) shows the details of the horizontal profiles of the initial turns. The dashed line in figure 25(a) shows where the horizontal turn ends and where the climb begins. As figure 25(b) shows, the larger forced horizontal turns decrease in speed to below the speed limit for the initial portion of the turn. All flightpaths are at the speed limit for the complete climb and for part of the descent. The thrust is zero for the early part of the larger turns (see fig. 25(d)). The maximum-thrust limit is never reached, but where the thrust peaks for the individual paths is indicated in figure 25(a) by a dotted line labeled T_m. The bank angle has the same shape for all the initial turns (fig. 25(c)). Furthermore, this shape is the same as for nonspeed-limited turns (fig. 19(c)). As figure 25(a) shows, the bank angle begins to decrease when the remaining heading change is less than about 33°. As figures 25(d)-25(f) show, the thrust, flightpath angle, and altitude are different only during the turns. A suboptimal algorithm was not developed for this case. However, in general, the more constrained an optimal path is, the easier it would be to write a suboptimal algorithm that approaches the optimal performance.

In the case of the speed-limited turns, which begin at the speed limit of 250 knots IAS, there are two choices to execute the larger turns. They can be started on the ascending arc, or they can be started on a forced horizontal turn.

Compare, for example, the curve in figure 25(a) labeled 163°, which begins with a turning climb at the speed limit of 250 knots IAS with the turn labeled 175° which begins at the same speed with a forced level turn and initially zero thrust for initial deceleration to fly a tighter turn, and which finally reaches the 250 knot IAS speed limit again to start climbing when it has only 32° left to turn. Without solving the two point boundary value problem, we cannot prove which type of extremal is optimal. However, from the unconstrained results and the suboptimal results for nonturning paths, we suspect that the forced level turn is optimal.

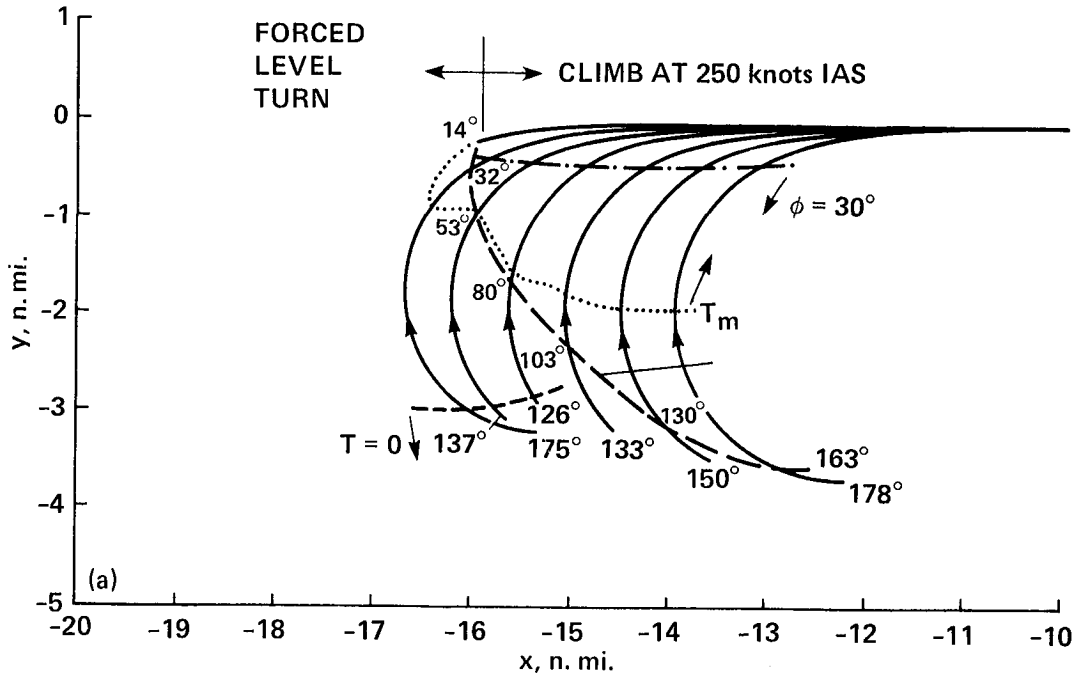

(a) Details of the turns.

Figure 25.- Intermediate-length speed-constrained terminal-area flightpaths with initial turns between 0° and 180° (initial speed 250 knots IAS).

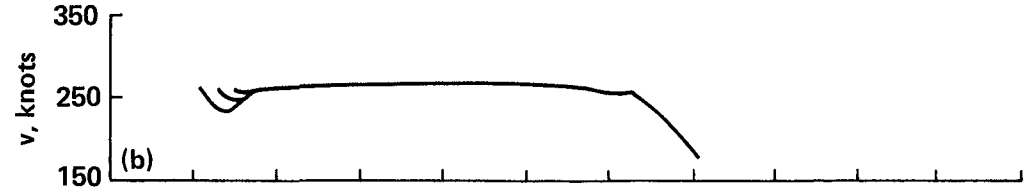

(b) Speed.

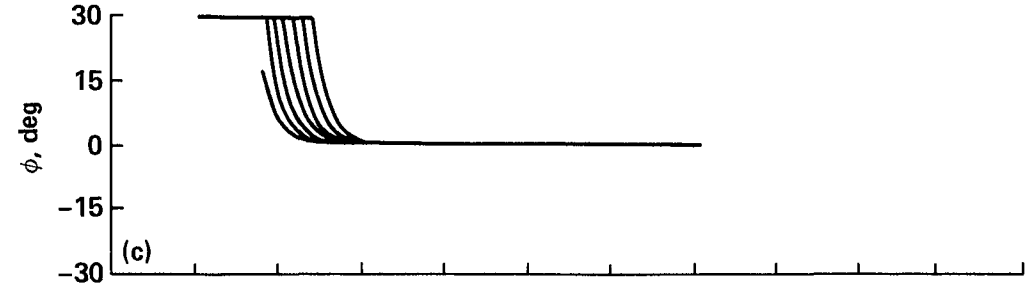

(c) Bank angle.

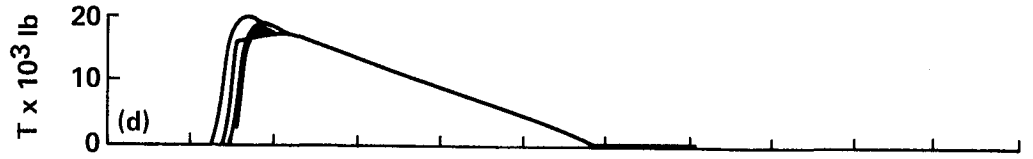

(d) Thrust.

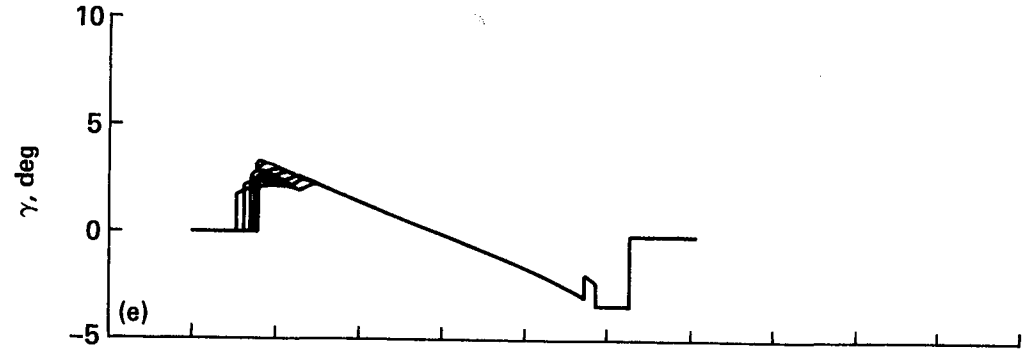

(e) Flightpath angle.

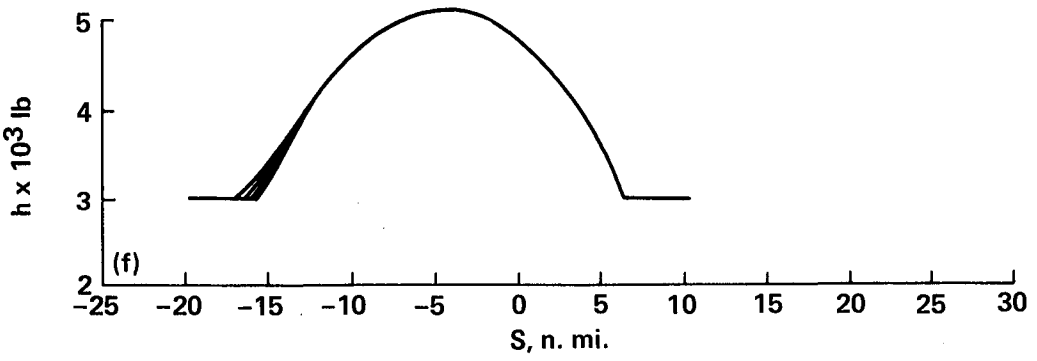

(f) Altitude profile.

Figure 25.- Concluded.

6. SUMMARY OF RESULTS AND CONCLUSIONS

The objectives of this work were to extend the work of reference 1 to include turns in optimal climbs and descents (sec. 2) and that of reference 8 to include altitude changes in optimal capture flightpaths (sec. 3). In particular, we wanted to discover the common characteristics of representative families of optimal flightpaths that are of practical interest and to identify the characteristics that provide most of the fuel savings. This is essential in order to devise suboptimal algorithms that can eventually be implemented on board. We were also interested in the extent the unconstrained optimal flightpaths violate the FAA-imposed 250-n. mi.-IAS constraint and the extra fuel consumption for implementing this constraint optimally.

The principal results of section 2 (turning climb-out and descent) are summarized below.

1. The results of section 2 are in qualitative and to some extent quantitative agreement with those of reference 1, as seen from figure 6; the quantitative differences are due to differences in aircraft modeling.

2. Climb-out turns are at level flight and are practically completed before the onset of climb. If altitudes below the initial altitude are permitted, the flightpath first dips at $\gamma_{min} = -4°$ while turning, as shown in figure 7(c).

3. In the descent, most of each turn is at level flight, with a small amount of turn during descent. If altitudes below the initial altitude are permitted, the flightpath dips during the initial small turn while descending, and then climbs for the remainder of the turn. For large turns, an additional unexpected final dip occurs, as shown in figure 10(c).

4. The altitude changes in climb-out and descent flightpaths are essentially nonturning with an almost constant (singular) flightpath angle γ of 4.4° on climb and -3.3° on descent, independent of the amount of turn (see table 1). The optimal thrust is $T = T_{max}$ on climb and $T = 0$ on descent, including on turns in both cases.

5. These characteristics of optimal climb and descent facilitate approximations. Thus, for on-board optimization of fuel-efficient turning descents and climb-outs, it is sufficient to use an existing climb-cruise-descent fuel-optimization algorithm and superimpose initial and final level turns from and to the airport. The extra fuel consumption for forcing level turns is much larger on climb (where $T = T_{max}$) than on descent (where $T = 0$). Thus, forcing the turns to be level by restricting γ within the range $-0.001 = \gamma_{min} \leq \gamma \leq \gamma_{max} = 0$ costs about 20 lb as compared with climbs in which an initial dip along $\gamma_{min} = -4°$ is permitted, independent of turn; for descent, the cost is only about 2 lb.

6. The main fuel-saving characteristic of optimal flightpaths is the completion of turns before climb. Thus, turning level with full bank angle instead of with optimal bank angle results only in the consumption of 4 lb of additional fuel on a 180° turn. But combining this turn with a climb at $\gamma = 3°$ wastes 285 lb of fuel (see fig. 12). That it is inefficient to start climbing at once, rather than turning and accelerating horizontally, surprised some experienced pilots.

7. Only on the later part of descent is the 250-knot-IAS constraint violated; its imposition (optimally, as a state-variable constraint) costs about 1 lb of fuel.

The optimal climb, however, is at an almost constant 294 knots IAS and the cost of imposing the 250-knot constraint is 36 lb of fuel, independent of the required heading change.

The principal results of section 3 (capture flights in the terminal area) are summarized below.

1. The optimal capture flightpaths computed can serve not only for missed approaches, but also as complete flightpaths between nearby airports in a metropolitan area. To estimate the fuel savings afforded by the optional flightpaths would entail elaborate piloted simulations, as was done for the case of reference 1. We believe the savings should be about the same, namely, about 5%.

2. The characteristics of the turns are the same as those in reference 8; for example, there is typically a deceleration on large turns to accomplish a tighter turn. But now, as expected, there is a climb to and a descent from a higher altitude (see fig. 15). The flightpath angle is singular also on the transition between climb and descent. The climbs and descents have the characteristics enumerated in items (2) to (4) under section 2 results above, except that the thrust is not always $T = T_{max}$ on climb. Except for the thrust for short flightpaths, the controls along turns at both ends of the flightpath are decoupled; this of course facilitates approximations.

3. Various approximations to optimal flightpaths were studied. An example is a nonturning 45 n. mi. long flightpath, which begins and ends at an altitude of 2,000 ft and a speed of 250 knots. The simplest approximation to this flightpath is flying at constant altitude and speed. This results in a 10% additional consumption of fuel. As a better approximation, if at level flight we accelerate with $T = T_{max}$ immediately to the best cruising speed and at the last moment decelerate with $T = 0$ from the cruising speed to the final speed, we reduce the extra fuel used to 6% above optimal. Using the suboptimal algorithm described in appendix B, which includes altitude changes, results in only 0.3% extra fuel over the optimal (see figs. 16-18).

When approximating turning optimal flightpaths, the efficiency of the near optimal algorithm is reduced somewhat. Using the near optimal algorithm for long and short paths, all with large turns, results in 0.44% and 2.24% additional fuel use, respectively.

4. The speed on climb portions of capture flightpaths exceeds the 250-knot-IAS constraint (see fig. 15(a)). Imposing the constraint results in a 3.7% increase in fuel use for nonturning flightpaths, that is, 20 to 50 lb for ranges of 30 to 50 n. mi. We did not make a comparison for the case of turning flightpaths, but we expect the increase in fuel consumption to be about the same.

Of course, not all possible flightpaths of interest were computed. None of our flightpaths exceeded the altitude of 10,000 ft because our drag and fuel-flow models were developed to be valid only up to that altitude. It would certainly be of interest to extend these models and to compute long-range airport-to-airport minimum-fuel flightpaths, including turns. Furthermore, families of capture flightpaths with end states different from ours could be added, for example, flightpaths that start and end at different altitudes. Of course, portions of the flightpaths presented in this report are also optimal. We did not compute very short (e.g., 2-n. mi.-long), highly turning flightpaths. Such flightpaths are rare, difficult to approximate, and moreover consume little fuel; for horizontal flight they are explored in reference 8.

Some of the results were unexpected, whereas others confirmed well-known results and practices. Of course, all results can be rationalized in retrospect on physical grounds, but only a quantitative optimization can confirm with confidence physical reasonings and intelligent guesses.

The fuel savings afforded by optimally flying the type of flightpaths studied here are, of course, small in relation to the fuel expenditure of long-distance airport-to-airport flightpaths. However, the cumulative saving is significant. Furthermore, with the present trend toward automation of air-traffic control, we feel it is economically worthwhile to incorporate, into future on-board flightpath management systems, fuel saving algorithms that approximate the optimal flightpaths. The development of such a suboptimal algorithm, in all its details, is a major task. However, NASA's considerable experience to date indicates that it is definitely feasible.

Ames Research Center
National Aeronautics and Space Administration
Moffett Field, California 94035, April 19, 1984

APPENDIX A

DRAG AND FUEL-FLOW EQUATIONS

Reference 16 explains the use of subroutines that calculate drag, thrust, and fuel flow from comprehensive table lookup data over the complete operating range of the Boeing 727-100 aircraft. For our method of calculating extremals, we need functional relationships for the limited range of 150- to 350-knot speeds and 0- to 10,000-ft altitudes, which are derived here.

Drag as a Function of Speed, Altitude, and Bank Angle

Over the range of speeds considered, flaps must be deployed for the lower speeds. However, we do not want to consider flaps as a control variable. Therefore, flaps are eliminated as an independent control by putting a limit on the angle of attack,

$$\alpha \leq \alpha_{max} = 8° \tag{A1}$$

and by automatically deploying the minimum amount of flaps so that $\alpha = 8°$ is never exceeded. Although the drag curves are shown in figure 26 for all altitudes, in

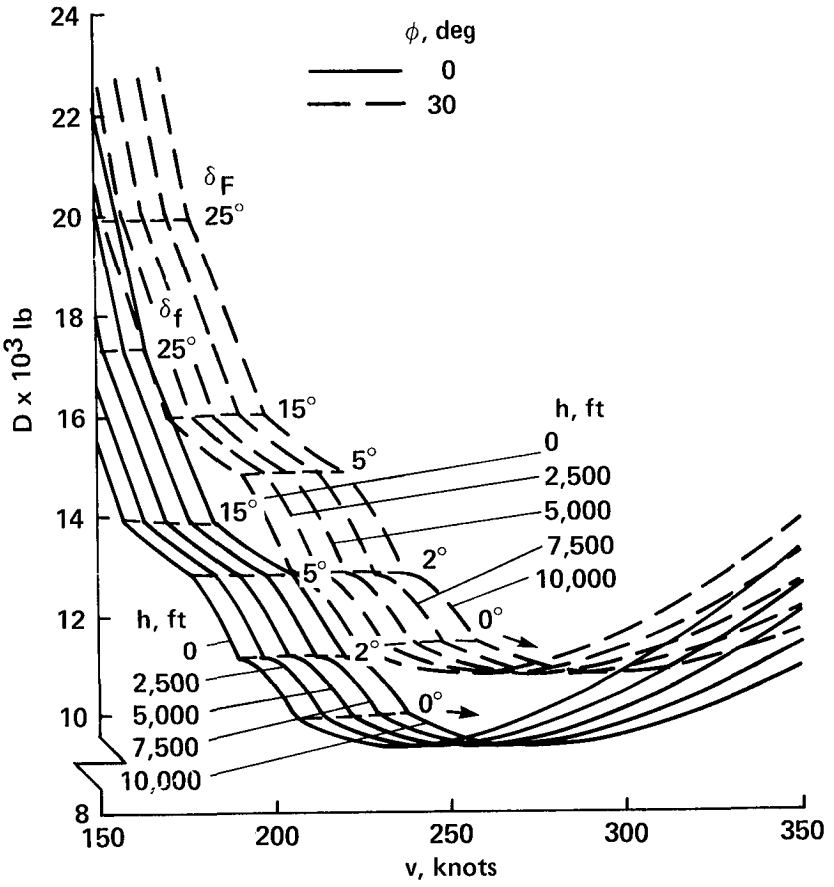

Figure 26.- Drag versus speed from table lookup.

practice flaps are deployed at low altitudes only. It turns out that the optimal results agree with this practice. Since we have the constraint,

$$L = W/\cos\ \phi \tag{A3}$$

assumed to be satisfied by automatically adjusting the angle of attack, the drag is bank-angle dependent, rather than α dependent.

$$D = D(v,h,\phi) \tag{A3}$$

It should be noted here that our flap schedule is different from that in reference 16, which deploys flaps as a function of indicated airspeed. Our flap program results show less drag at the lower speeds than the schedule of reference 1. However, neither method represents the real world completely, since, at present, flaps are controlled manually in steps, based on speed cues.

The calculation of the drag proceeds as follows. Given h and v, from the 1962 atmospheric model we obtain density ρ and Mach number M. Knowing the bank angle, we calculate the required lift coefficient to meet the constraint (eq. (A2)),

$$C_L = W/(0.5\ \rho S v^2\ \cos\ \phi) \tag{A4}$$

where S = area of the wings = 1,560 ft, W = weight of the aircraft = 150,000 lb, and ρ = density of air at the given altitude. Then, for $\alpha = 8°$ the subroutine CLIFT (ref. 1) computes the available lift coefficient $C_{L_{av}}(\alpha,h,M\ \delta_f)\big|_{\alpha=8°}$. Starting with zero flaps, the flaps are increased in 0.01° steps until

$$C_{L_{av}} \geq C_L \tag{A5}$$

This final flap value is then used in the subroutine CDRAG of reference 1 which determines the drag coefficient $C_D(M,C_L,\delta_f)$. This permits us to calculate the drag

$$D = 0.5\ \rho S v^2 C_D = D(h,v,\phi)\big|_{\alpha\leq 8°,L=W/\cos\phi} \tag{A6}$$

An example of the drag curves obtained by the above method, including the flaps required, is shown in figure 26. The bumpiness of the drag-versus-speed curves in the region where flaps are deployed is an artifact of linear interpolation of the drag polars which are given only for 0°, 2°, 5°, 15°, 25°, and 40° flap angles. Our model will be designed to smooth out these bumps.

It is our task (1) to determine an analytic relationship for drag that involves only ϕ, v, and h; (2) to determine approximate values for the parameters; and (3) to minimize the error between the analytic representation and the full table lookup of the fuel flow when using the standard 1962 atmosphere. In order to minimize the number of parameters required, we shall first develop an expression from the approximate theory of wings, and then determine parameters that fit the data.

The lift coefficient of a clean wing is

$$C_L = C_{L_\alpha}\alpha \tag{A7}$$

Adding flaps shifts the curve upward

$$C_L' = C_{L_0} + C_{L_\alpha}\alpha \tag{A8}$$

Without flaps the lift-drag polar is

$$C_D = C_{D_0} + \eta C_{L_\alpha}\alpha^2 = C_{D_0} + \eta C_L \alpha \tag{A9}$$

Assuming the same form when the drag polar is shifted owing to flaps adds a linear term in α:

$$C_D' = C_{D_0}' + \eta' C_L' \alpha = C_{D_0}' + \eta'\left(C_{L_0}\alpha + C_{L_\alpha}\alpha^2\right) \tag{A10}$$

From equation (A4) setting $C_L = C_L'$ and using equation (A8) we can solve for

$$\alpha = \left[W/(0.5\ \rho S v^2 \cos\phi) - C_{L_0}\right]/C_{L_\alpha} \tag{A11}$$

and using equation (A11) to replace α in the drag equation (A10) results in an equation for drag of the form

$$D = C_D'\ 0.5\ \rho S v^2 = b_0/\cos\phi + b_1 v^2 + b_2(1 + \tan^2\phi)/v^2 \tag{A12}$$

where the b's are functions of ρ, S, W, η', C_{L_0}, C_{L_α}, and C_{D_0}'.

This is the form of the functional relationship for a constant altitude and constant flap angle. In actuality, the flap changes with speed for constant altitude as shown in figure 26. The bank angle, which is one of the controls, appears twice in the above expression. The first approximation of the b's in equation (A12), which must be functions of altitude, as found as follows. We write for $\phi = 0$

$$D = k_1(1 + k_2 h) + k_3(1 + k_4 h)v^2 + k_5(1 + k_6 h)/v^2 \tag{A13}$$

Using the tabular data that are graphically represented in figure 26, for $h = 0$, $\phi = 0$ and for three different speeds of 150, 225, and 350 knots, we obtain three equations with three unknowns, k_1, k_3, and k_5. With these solved, we choose $h = 10{,}000$ ft and $\phi = 0$, and solve for k_2, k_4, and k_6. These six constants are a good first approximation to the drag equation. These constants are then used for the complete drag equation (A12),

$$D = k_1(1 + k_2 h)/\cos\phi + k_3(1 + k_4 h)v\ + k_5(1 + k_6 h)(1 + \tan^2\phi)/v^2$$

which using $\cos\phi = 1/(1 + \tan^2\phi)^{1/2} \approx 1/(1 + 0.5\tan^2\phi)$ is approximated as

$$D = k_1(1 + k_2 h) + k_3(1 + k_4 h)v^2 + k_5(1 + k_6 h)/v^2 + [k_1(1 + k_2 h)/2$$

$$+ k_5(1 + k_6 h)/v^2]\tan^2\phi \tag{A14}$$

For the purpose of an improved analytic approximation of the drag function, we generate 180 samples from equation (A14) and the corresponding values from the interpolation of the original data for all combinations of the following parameters:

$\phi = 0°, 10°, 20°, 30°$

h = 0, 2,500, 5,000, 7,500, 10,000 ft

v = 150, 175, 200, 225, 250, 275, 300, 325, 350 knots

and calculate the rms percent error between the table lookup values and the analytic drag equation. By means of an extremum-finding subroutine (ref. 17) the parameters are adjusted to minimize the rms percent error, which results in an rms error of 2.387%. This apparent error is primarily a result of the desirable smoothing of the drag curves in the flap deployment region. The polynomial fit agreed within 0.8% (max) with the drag in the $\delta_f = 0$ region. The values of the coefficients in equation (A14) are

$$k_1 = -0.4078\times10^{4} \qquad k_3 = 0.1146 \qquad k_5 = 0.3830\times10^{9}$$

$$k_2 = 0.2429\times10^{-4} \qquad k_4 = -0.2005\times10^{-4} \qquad k_6 = 0.4227\times10^{-4}$$

The resulting drag curves are shown in figure 27, which may be compared with the table lookup data in figure 26. For example, the node for $u = 0$ is at

$$v = 0.5\ k_1k_2/(k_3k_4) + \{0.25[(k_1k_2)/(k_3k_4)]^2 - k_5k_6/(k_3k_4)\}^{1/2} \qquad \text{(A15)}$$

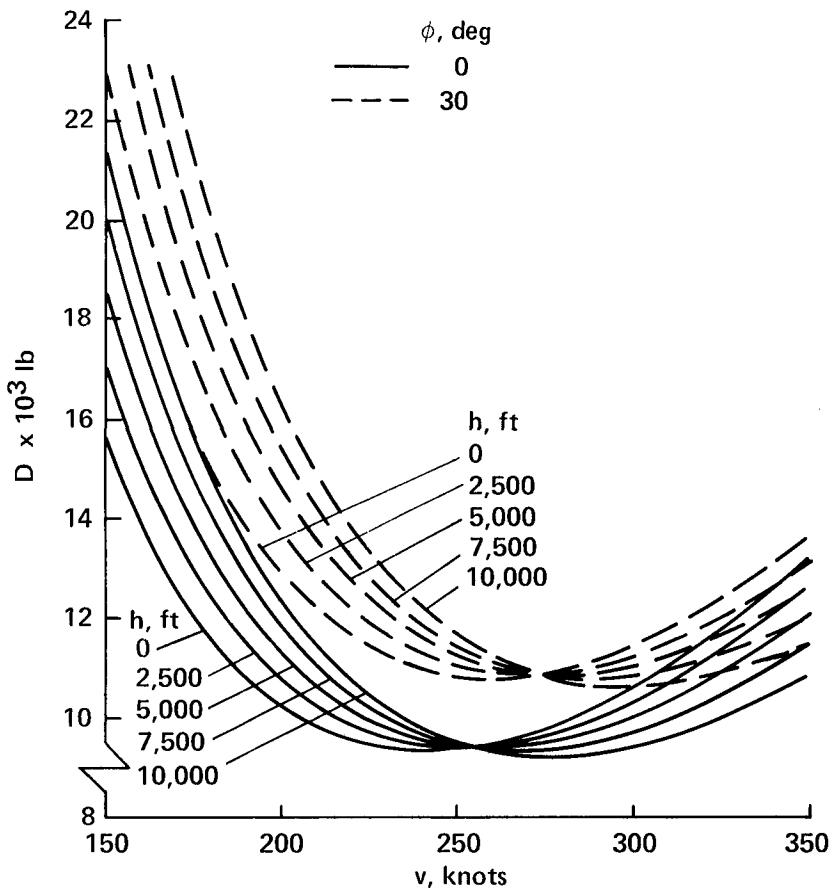

Figure 27.- Drag versus speed from algebraic equation.

The curves derived from the table lookup have a constant minimum (fig. 26) drag, which occurs at increasing speeds for increasing altitudes. This is not the case for the polynomial approximation. However, the nature of the increasing speed with altitude for minimum drag is preserved in the polynomial representation.

Fuel Flow as a Function of Thrust Speed and Altitude

Reference 1 presents fuel-flow data in tabular form,

$$\dot{f}_n = \dot{f}_n(\text{Mach}, T_n, h) \tag{A16}$$

where $\dot{f}_n$ is a normalized fuel flow rate,

$$\left.\begin{aligned} \dot{f}_n &= \dot{f}/(T\sqrt{\theta}) \\ \dot{f} &= \text{actual fuel flow rate} \end{aligned}\right\} \tag{A17}$$

and

$$T = \text{thrust for three engines} = \delta T_n \tag{A18}$$

where T_n is the normalized thrust for three engines,

$$\left.\begin{aligned} \sqrt{\theta} &= \text{square root of the temperature ratio} \\ \theta &= \text{the ratio of temperature at altitude } h \text{ to the temperature at zero altitude} \end{aligned}\right\} \tag{A19}$$

and

$$\delta = \text{pressure ratio} = \text{ratio of pressure at altitude } h \text{ to pressure at zero altitude} \tag{A20}$$

It is our task (1) to determine an analytical relationship for fuel flow that involves only T,v,h; (2) to determine approximate values for the parameters; and (3) to minimize the error between the analytic representation and the full table lookup of the fuel flow when using the standard 1962 atmosphere.

The $\dot{f}_n$ entries in the three-dimensional table used in reference 1 are normalized there in such a way that they are almost altitude-independent. For the first two steps of the task we are therefore using only the table for $h = 5{,}000$ ft. In figure 28, the $\dot{f}_n$ values multiplied by the normalized thrust T_n are plotted versus T_n over the range of Mach numbers of interest, because this quantity is the actual fuel flow normalized by atmospheric constants where, from equations (A17) and (A18),

$$T_n\dot{f}_n = T_n\dot{f}/(T\sqrt{\theta}) = \dot{f}/(\delta\sqrt{\theta}) \tag{A21}$$

The relationship between normalized fuel flow and normalized thrust is shown in figure 28; it was approximated as

$$\frac{\dot{f}}{\delta\sqrt{\theta}} = 0.45 + M + \frac{3.75 + 3.35M}{30{,}000} T_n + \frac{0.5(1 - M)}{30{,}000^2} T_n^2 \tag{A22}$$

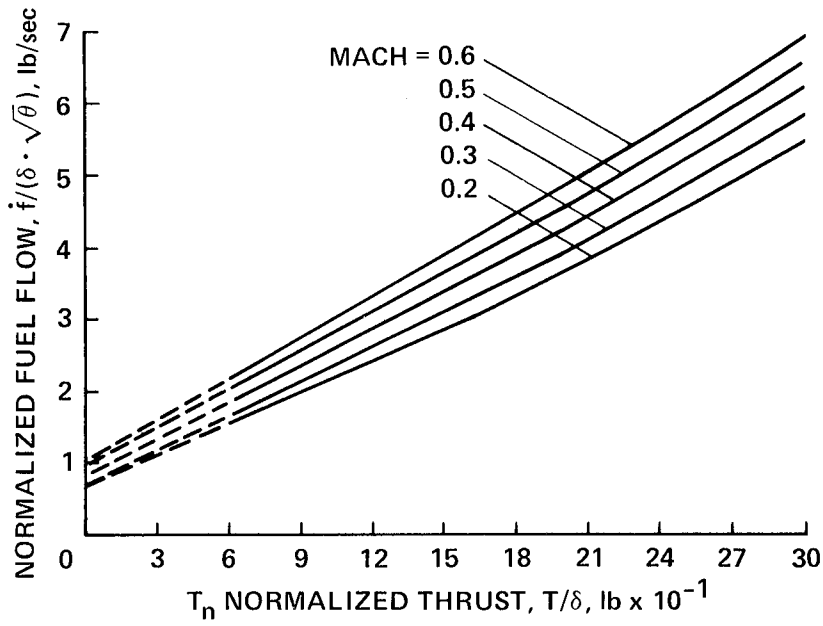

Figure 28.- Fuel-flow rate versus T_n for h = 5,000 ft.

Equation (A17), used in (A22), gives the actual fuel flow:

$$\dot{f} = \delta\sqrt{\theta}\left[0.45 + M + \frac{3.75 + 3.25M}{30{,}000}\frac{T}{\delta} + \frac{0.5(1 - M)}{30{,}000^2}\left(\frac{T}{\delta}\right)^2\right] \tag{A23}$$

Fuel flow is still a function of the pressure ratio, temperature ratio, and Mach number, which are all functions of altitude. The altitude dependence for the normal atmosphere is presented in table 3.

TABLE 3.- NORMAL ATMOSPHERE

Altitude, ft^3	Temp, K	$\sqrt{\theta}$	P, lb/ft^2	ρ, $slugs/ft^3 \times 10^4$	$\delta = P/P_0$	$\sigma = \rho/\rho_0$	$\sigma^{-1/2}$	Sound speed, ft/sec
0	288.15	1.0	2,116	23.77	1.0000	1.0000	1.0000	1,116.9
2,000	284.19	.99	1,968	22.41	.9298	.9428	1.0299	1,109.2
4,000	280.23	.99	1,828	21.11	.8637	.8881	1.0611	1,101.4
6,000	276.27	.98	1,696	19.87	.8014	.8359	1.0938	1,093.6
8,000	272.31	.97	1,572	18.08	.7428	.7860	1.1279	1,085.7
10,000	268.35	.97	1,455	17.55	.6877	.7385	1.1637	1,077.8

We can see from table 3 that the speed of sound decreases with altitude, so that the speed expressed in units of Mach number M increases with altitude,

$$M = v(1 + 0.363\times10^{-5}h)/1116.9 \tag{A24}$$

where v is given as true airspeed in feet per second. The pressure ratio can be expressed as

$$\delta = 1/(1 + 0.45h/10{,}000) \approx 1 - 0.31h/10{,}000 \tag{A25}$$

and the square root of the temperature ratio as

$$\sqrt{\theta} = 1 - 0.363\times10^{-5}h \tag{A26}$$

Using equations (A23)-(A26) allows us to obtain $\dot{f}$ when T, H, and v are given. We can rewrite equation (A23) as

$$\dot{f} = C_0(h,v) + C_1(h,v)T + C_2(h,v)T^2 \tag{A27}$$

where each of the C's is a function of altitude and speed. When equations (A24), (A25), and (A26) are used to replace M, δ, and $\sqrt{\theta}$ in equation (A23), and when all resulting higher-order terms except terms involving hv are neglected, all C's end up in the same form,

$$C_j = c_{4j+1}(1 + c_{4j+2}h) + c_{4j+3}(1 + c_{4j+4}h)v \; ; \qquad j = 0,1,2 \tag{A28}$$

The numerical values of the 12 parameters in equation (A28) were used as initial values in the extremum-finding subroutine (ref. 17) where the parameters c_1 to c_{12} are adjusted to minimize the rms error between table lookup values and the results of equations (A27) and (A28) for the 210 points given by all combinations of

T = 7,000, 9,500, 12,000, 14,500, 17,000, 22,000, 24,500 lb

v = 150, 200, 250, 300, 350 knots

h = 0, 2,000, 4,000, 6,000, 8,000, 10,000 ft

For this procedure, the actual fuel flow was calculated by using all appropriate fuel-flow tables, as well as the exact nominal atmospheric model. This resulted in an rms error of 0.039 lb/sec. The values are

$c_1 = 0.47537$ $\qquad$ $c_5 = 0.10823\times10^{-3}$ $\qquad$ $c_9 = 0.91747\times10^{-9}$

$c_2 = -0.24360\times10^{-4}$ $\qquad$ $c_6 = -0.80509\times10^{-5}$ $\qquad$ $c_{10} = 0.79644\times10^{-4}$

$c_3 = 0.17702\times10^{-2}$ $\qquad$ $c_7 = 0.15898\times10^{-6}$ $\qquad$ $c_{11} = -0.85521\times10^{-12}$

$c_4 = -0.28995\times10^{-4}$ $\qquad$ $c_8 = -0.12439\times10^{-4}$ $\qquad$ $c_{12} = -0.45624\times10^{-4}$

These data are known to be accurate for $T \geq 7{,}000$ lb. Additional data are available only for engine idle (T = 0). These data agreed reasonably well with the expression for T = 0 in equations (A27) and (A28). Hence, equations (A27) and (A28) will be used over the complete range of thrust. An example of the resulting fuel flow versus thrust function is shown in figure 29.

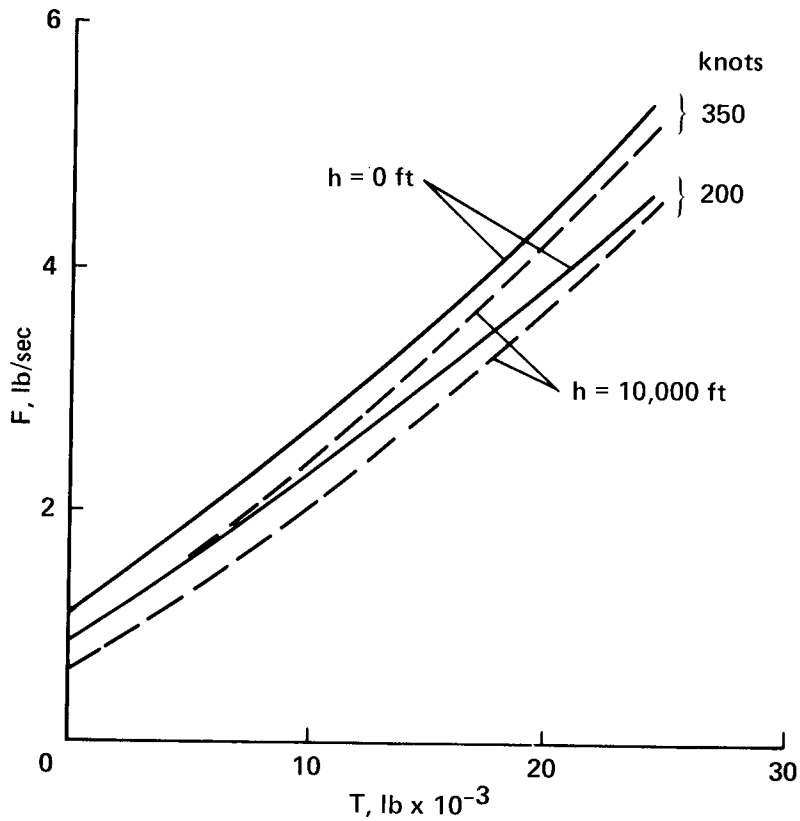

Figure 29.- Fuel-flow model of the B727-100.

APPENDIX B

SUBOPTIMAL ALGORITHM FOR THE SYNTHESIS OF INTERMEDIATE-LENGTH CAPTURE FLIGHTPATHS

The algorithm described here uses simple commands to abstract the essential features of the optimal capture trajectories and generate capture trajectories with specified terminal conditions. In contrast to reference 15, in which capture flightpaths were generated even for very short flightpaths (2-5 n. mi.) (which required complicated turning to solve the two-point boundary-value problem), the algorithm described here only solves intermediate-length flightpaths. Such flightpaths are the more common ones. The turning portions of the flightpaths are calculated in a way similar to that described in reference 15. In addition, the algorithm described here is not fully developed for flight, since it uses more data from the optimal path than would be available on board, where only the boundary conditions are known. A complete development would require that functional relationships be abstracted from the optimal solution for the climb and descent angles. In addition, the speeds and altitudes at which climb and descent would be initiated would have to be known, as well as the altitudes for the nonsteady cruise, as a function of the path length. This would not be a difficult task.

For the algorithm, data are required at six points of the optimal flightpath: the initial point, the point where the initial climb begins, the point where the initial climb ends and the thrust reduction begins, the point where the descent begins, the point where the descent ends, and the final point. Selected elements of the following data at each of the above points are required: position (x,y,z), heading, speed, and, for comparison with the suboptimal path, also the fuel used.

Straight-Line Flightpath

The suboptimal command sequence for nonturning flight was shown in figure 17 and is discussed here in greater detail. The aircraft accelerates horizontally until it reaches the speed for initiating the climb (point a in fig. 17). At this point the aircraft begins to climb at the average of the optimal climb angle, which is calculated from the positions at the beginning and end of the optimal maximum thrust climb. The maximum thrust climb ends at the altitude where in the optimal control the thrust reduction begins (point b). At this point, the thrust is reduced linearly with time until thrust equals drag (point c), which is then maintained. The best time interval for the linear thrust reduction as a function of the path length was found via simple trial and error. During this thrust reduction the climb is continued at the same flightpath angle until a certain altitude is reached (point d). This chosen altitude is the one at which the optimal flightpath begins the zero thrust descent.

The remaining path is found via backward integration and is described in backward time. The aircraft accelerates in level flight from the final speed at zero thrust until it reaches the optimal speed for initiating zero thrust climb (point e in fig. 17). At this point the aircraft begins to climb at the average of the optimal climb angle, which is calculated from the positions at the beginning and end of the optimal zero thrust descent. This climb continues to the altitude where the optimal descent begins (point f). The forward and backward integrated paths (points d and f) are now at the same altitude; however, the speed of the zero thrust climb (point f) turns out to be lower than the speed reached in the forward integration of

the path (point d). Therefore, a final level-flight zero-thrust acceleration in backward time follows until the speeds match (point g). Now the speeds and altitudes match, but the positions do not. In the forward integration, the thrust equaled the drag (point c); hence, it is natural to fly from point c to point g at constant speed. This completes the development of the straight-line flightpath.

Turns

Since, in contrast to the optimal turns, the suboptimal turns are accomplished at maximum bank angle, they are always completed before the climb begins. This applies for both the initial turn in the forward-time integration and the final turn in the backward-time integration.

To determine the directions and approximate magnitudes of the turns, the capture algorithm of reference 7 is used. This capture algorithm delivers circular turns with radii as a function of the entry speeds to the turns. Because this is only an approximation we calculate the paths of the true constant bank angle turns, using forward and backward integration of equations (1)-(5) for one-half the heading changes specified by the algorithm of reference 7. Then the algorithm of reference 7 is called again from the new endpoints, and the process is repeated until both remaining turns are less than 0.5°. From these new endpoints the remaining path is essentially a nonturning path.

There is one additional fuel-saving element incorporated in the suboptimal turn generation. If the initial turn is large, it is flown at zero thrust until the remaining turn is less than 120°; at that point full thrust is applied.

APPENDIX C

FUEL-FLOW AND DRAG DERIVATIVES USED IN THE TEXT

In the development of the singular-γ arc equations, we need certain time-derivatives and other derivates which we shall enumerate here. Let us assume that T and u are time variable.

$$F = [c_1(1 + c_2h) + c_3(1 + c_4h)v] + [c_5(1 + c_6h) + c_7(1 + c_8h)v]T + [c_9(1 + c_{10}h) + c_{11}(1 + c_{12}h)v]T^2 = C_0 + C_1T + C_2T^2 \tag{C1}$$

$$F_v = c_3(1 + c_4h) + c_7(1 + c_8h)T + c_{11}(1 + c_{12}h)T^2 = C_{0v} + C_{1v}T + C_{2v}T^2 \tag{C2}$$

$$\dot{F}_v = F_{vh}\dot{h} + F_{vT}\dot{T} = (c_3c_4 + c_7c_8T + c_{11}c_{12}T^2)\dot{h} + [c_7(1 + c_8h) + 2c_{11}(1 + c_{12}h)T]\dot{T} \tag{C3}$$

$$F_h = (c_1c_2 + c_3c_4v) + (c_5c_6 + c_7c_8v)T + (c_9c_{10} + c_{11}c_{12}v)T^2 = C_{0h} + C_{1h}T + C_{2h}T^2 \tag{C4}$$

$$\dot{F}_h = F_{vh}\dot{v} + F_{hT}\dot{T} = (c_3c_4 + c_7c_8T + c_{11}c_{12}T^2)\dot{v} + [c_5c_6 + c_7c_8v + 2(c_9c_{10} + c_{11}c_{12}v)T]\dot{T} \tag{C5}$$

$$\left.\begin{aligned} \tau &= -(C_1 + \lambda_v g/W)/(2C_2) \\ \dot{T}^* &= \tau_v\dot{v} + \tau_h\dot{h} + \tau_{\lambda_v}\dot{\lambda}_v \quad \text{if} \quad 0 < \tau < T_{max} \ ; \\ \dot{T}^* &= 0 \quad \text{if} \quad T^* = 0 \quad \text{or} \quad T^* = T_{max} \end{aligned}\right\} \tag{C6}$$

$$\tau_v = -[C_2C_{1v} - (C_1 + \lambda_v g/W)C_{2v}]/(2C_2^2) \tag{C7}$$

$$\tau_h = -[C_2C_{1h} - (C_1 + \lambda_v g/W)C_{2h}]/(2C_2^2) \tag{C8}$$

$$\tau_{\lambda_v} = -g/(2WC_2) \tag{C9}$$

$$D = k_1(1 + k_2h) + k_3(1 + k_4h)v^2 + k_5(1 + k_6h)/v^2 + [k_1(1 + k_2h)/2 + k_5(1 + k_6h)/v^2]u^2 = D_1 + D_2u^2 \tag{C10}$$

$$D_u = 2D_2u \tag{C11}$$

$$D_v = 2k_3(1 + k_4h)v - 2k_5(1 + k_6h)(1 + u^2)/v^3 = D_{1v} + D_{2v}u^2 \tag{C12}$$

$$\dot{D}_v = 2k_3(1 + k_4h)\dot{v} + 2k_3k_4\dot{h}v + 6k_5(1 + k_6h)(1 + u^2)\dot{v}/v^4 - 4k_5(1 + k_6h)u\dot{u}/v^3 - 2k_5k_6\dot{h}(1 + u^2)/v^3 \tag{C13}$$

$$D_h = k_1k_2 + k_3k_4v^2 + k_5k_6/v^2 + (k_1k_2/2 + k_5k_6/v^2)u^2 = D_{1h} + D_{2h}u^2 \tag{C14}$$

$$\dot{D}_h = 2k_3k_4v\dot{v} + (k_1k_2 + 2k_5k_6/v^2)u\dot{u} - 2k_5k_6(1 + u^2)\dot{v}/v^3 \tag{C15}$$

$$\dot{D} = D_h\dot{h} + D_u\dot{u} + D_v\dot{v} \tag{C16}$$

$$\left.\begin{aligned} \dot{u} &= u\left\{\left[\frac{1}{v}\left(1 - \frac{k_1(1 + k_2h)}{D_2}\right)\right]\dot{v} + \frac{\dot{\lambda}_\psi}{\lambda_\psi} - \frac{\dot{\lambda}_v}{\lambda_v} - \frac{D_{2h}}{D_2}\dot{h}\right\} \text{ if } |u| < u_m \\ \dot{u} &= 0 \ ; \qquad u = u_m \end{aligned}\right\} \tag{C17}$$

APPENDIX D

CONCAVE VELOCITY SET PROBLEM

Chattering Solution

If the velocity set is not convex then for some end conditions the optimal solution may not exist (ref. 18). The velocity set is defined as follows. Let $\dot{x} = f(x,u)$ be the differential equation describing the system (the aircraft in our case), where x is the state vector and u the control vector. For a fixed state x, the set of all possible vectors $f(x,u)$, or $\dot{x}$, obtained by using all possible controls u, is called the velocity set.

Figure 30(a) shows the projection of the velocity set on the $(\dot{\psi},\dot{v})$ plane. It shows that for deceleration, the velocity set is not convex in the region of zero thrust because of increased drag at nonzero bank angles. In this case, a relaxed controller (or chattering control, an idealized condition in which the control moves in zero time between its limits forming a square wave at infinite frequency) may result in better performance if maximum deceleration will improve performance. To make the velocity set convex we allow the possibility of a chattering bank angle and define a combined control, which enlarges the area of the velocity set:

$$u = \alpha u_s - (1 - \alpha)u_s = u_s(2\alpha - 1) \tag{D1}$$

where u_s is the magnitude of the tangent of the bank angle $u_s = |\tan \phi|$, $0 \le u_s \le u_m$, and α is the chatter parameter (fig. 30(b)), $0 \le \alpha \le 1$

α = per unit time the bank angle is at u_s

$1 - \alpha$ = per unit time the bank angle is at $-u_s$

then equation (4) changes to

$$\dot{\psi} = -gu_s(2\alpha - 1)/v \tag{D2}$$

and the Hamiltonian (eq. (12)) becomes (assuming $\eta = 0$, off the speed limit)

$$H = C_0 + C_1T + C_2T^2 - Cv \cos \psi + \lambda_h v\gamma - \lambda_\psi g u_s(2\alpha - 1)/v + \lambda_v g(T - D_1 - D_2u_s^2 - W\gamma)/W \tag{D3}$$

Note that the drag is only a function of u_s^2 and does not depend on the value of the chatter parameter α, because the control is either at u_s or $-u_s$. The optimal α and u_s are those that minimize H while using their permissible range. Then, removing terms not functions of α and u_s equation (D3) becomes

$$H(\alpha,u_s) = -\lambda_\psi g(2\alpha - 1)u_s/v - \lambda_v g D_2 u_s^2/W$$

from which α^* and u_s^* can be found

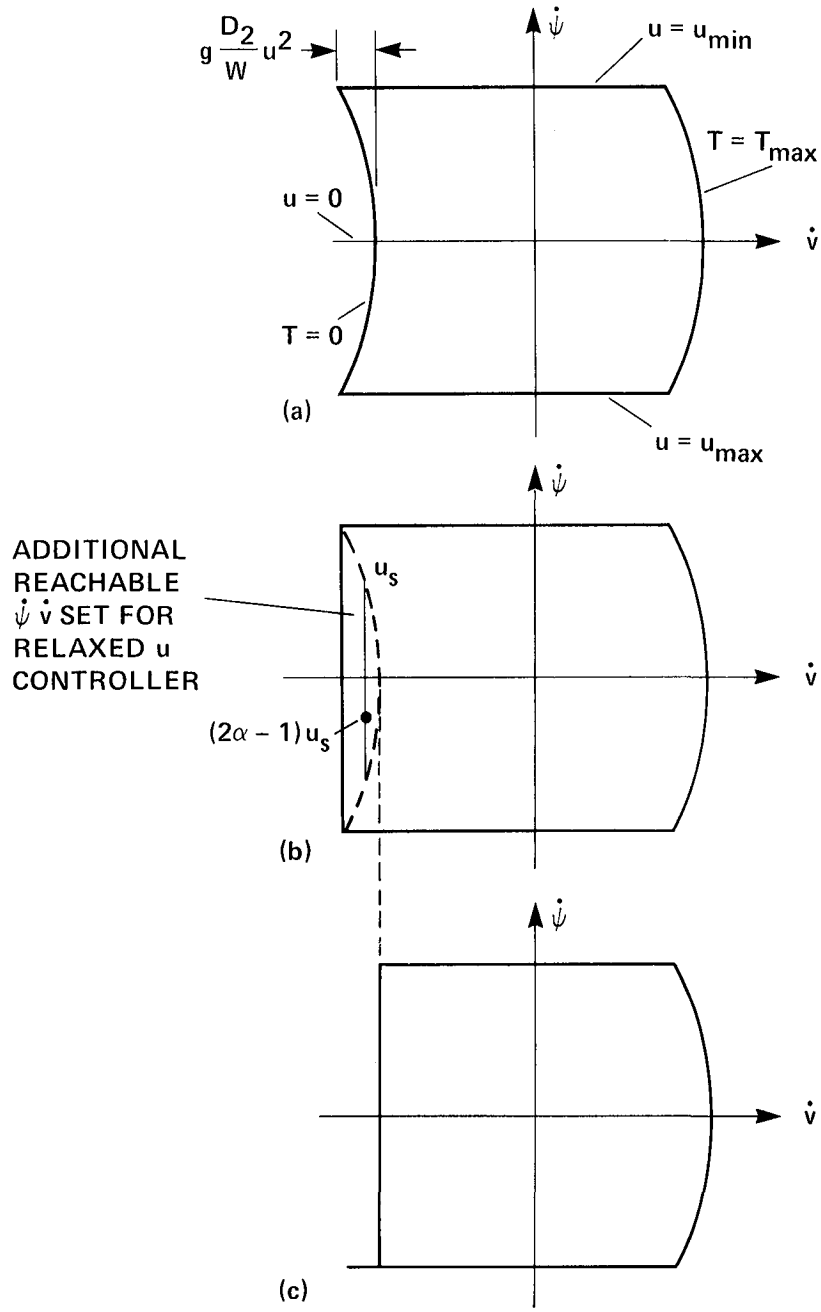

Figure 30.- Cross section through the velocity set $\dot{h}$, $\dot{v}$, $\dot{\psi}$, and F, given v and h and $\gamma = \gamma_{max}$. (a) Nonconvex set; (b) convex set that has increased velocity set volume compared to (a); (c) convex set that has decreased velocity set volume compared to (a).

$$\alpha^* = \begin{cases} 0 & \text{if} \quad \lambda_\psi < 0 \\ 1 & \text{if} \quad \lambda_\psi > 0 \end{cases} \tag{D4}$$

and equations (20) and (21) become

$$u_s^* = \begin{cases} \nu & \text{if} \quad \nu < u_m \quad \text{and} \quad \lambda_v < 0 \\ u_m & \text{if} \quad \nu \geq u_m \quad \text{and} \quad \lambda_v < 0 \end{cases} \tag{D5}$$

$$\nu = -[(2\alpha^* - 1)W\lambda_\psi]/[2\lambda_v D_2 v] \tag{D6}$$

We note that u_s^* is always positive as required. When α^* from equation (D4) and u_s^* from equations (D5) and (D6) are inserted into equation (D1), we can see that the combined control, u^*, has the same value as it had when equations (20) and (21) were used and equations (D2) and (D3) revert to the original equations (4) and (12). However, α is linear and we must also consider the singular-α solution. From equation (D3),

$$H_\alpha = -2g\lambda_\psi u_s/v = 0 \rightarrow \lambda_\psi = 0 \tag{D7a}$$

But from equations (20) and (D5), $u_s = 0$ when $\lambda_\psi = 0$. This is equivalent to the nonchattering straight descent and again is included in the earlier solutions, which do not require a chattering bank angle. Since the results for the convex set are the same as those for the original nonconvex set, we can solve the optimal descent problem as if the original velocity set were convex. For $\lambda_\psi \equiv 0$ minimization of H in equation (D3) gives

$$u_s = \begin{cases} 0 & \text{if} \quad \lambda_v < 0 \qquad \text{(D7b)} \\ u_m & \text{if} \quad \lambda_v > 0 \qquad \text{(D7c)} \end{cases}$$

Here, equation (D7b) implies $u = 0$ as from equations (20) and (21). When $\lambda_\psi \equiv 0$, a nonturning flight, the undetermined α^* in equation (D4) must be set at $\alpha^* = 1/2$ in order for equation (D7c) to be consistent with a nonturning flight.

Introducing Constraints

A different approach to make the velocity set convex is to apply appropriate constraints. This will cut off portions of the earlier velocity set. A reduced velocity set in general means reduced performance. We will, therefore, reduce the velocity set in such a way as to minimize the excised area. To do this, we impose an acceleration constraint, which limits deceleration to a constant value for each (v,h) such that it equals the maximum value which can be obtained at zero bank angle (fig. 30(c)). The resulting deceleration constraint is a mixed state and control constraint. From equation (5) with $T = 0$, $v = 0$ for the final turn after the descent we find the deceleration constraint that will keep the deceleration inside the curve of figure 30(c):

$$M = -g\left[D_1(v,h) + W\gamma_{max_0}\right]/W - \dot{v} \geq 0 \tag{D8}$$

where γ_{max_0} is the maximum flightpath angle for wings-level flight in descent. In the following development we only express the changes from the original set of equations, where we express the original equations as before and star (*) the new values. Then, from equations (12) and (D8), as an additional constraint,

$$H^* = H + \mu\left\{-g\left[D_1(v,h) + W\gamma_{max_0}\right]/W - \dot{v}\right\} \tag{D9}$$

Inserting equation (5) for $\dot{v}$ and simplifying gives

$$H^* = H + \mu\left\{-g\left[T - D_2(v,h)u^2 - W\left(\gamma - \gamma_{max_0}\right)\right]/W\right\} \tag{D10}$$

and the adjoint equations (13), (14), and (15) become

$$\dot{\lambda}_h^* = \dot{\lambda}_h - \mu g D_{2_h} u^2/W \tag{D11}$$

$$\dot{\lambda}_\psi^* = \dot{\lambda}_\psi \tag{D12}$$

$$\dot{\lambda}_v^* = \dot{\lambda}_v - \mu g D_{2_v} u^2/W \tag{D13}$$

On the deceleration bound we have $T - D_2(v,h)u^2 - W(\gamma - \gamma_{max_0}) = 0$; therefore,

$$\gamma = \gamma_{max_0} - D_2 u^2/W + T/W \tag{D14}$$

We are interested in the decelerating descent at $T = 0$; hence, γ is just decreased sufficiently from the maximum allowable for nonturning flight by flying a steeper descent to compensate for the additional drag term $D_2 u^2/W$ owing to a nonzero bank angle. Since the turn is not exactly horizontal, we must get off the speed-limited arc at somewhat above the desired final altitude.

From $H_\gamma^* = 0 = H_\gamma + \mu g$ we have

$$\mu = \begin{cases} \lambda_v - \lambda_h v/g > 0 & \text{on the deceleration constraint} \\ 0 & \text{off the deceleration constraint} \end{cases} \tag{D15}$$

The requirement that μ be greater than zero on the acceleration constraint is a necessary condition for optimality. Thrust control is determined by

$$H_T^* = H_T - \mu g/W$$

Hence, instead of equation (18) we now have

$$\tau = -[C_1(h,v) + (\lambda_v - \mu)g/W]/[2C_2(h,v)] \tag{D16}$$

and for bank angle control,

$$H_u^* = H_u + \mu 2gD_2(h,v)u/W$$

Thus, instead of equation (21), we now have

$$\nu = -\lambda_\psi W/[2(\lambda_v - \mu)D_2(h,v)v] \tag{D17}$$

Note in equations (D16) and (D17) $\lambda_v - \mu$ can be replaced via equation (D15) by

$$\lambda_v - \mu = \lambda_h v/g \tag{D18}$$

We are now in a position to compare the solutions for the convex set with those of the original set. The above constraints, which only apply to the descent, did not affect the performance (worse by less than 0.2 lb of fuel than the unconstrained optimal). Since the solutions for the larger but nonconvex set have a better performance we shall accept them. The acceleration constraint was only artificially introduced to satisfy the minimum principle rather than representing passenger or equipment requirements.

REFERENCES

1. Erzberger, H.: Optimum Climb and Descent Trajectories for Airline Missions. AGARDograph No. 251, July 1981.

2. Kreindler, E.; and Neuman, F.: Global Optimality of Extremals: An Example. NASA TM-81240, 1980. (Also Journal of Optimization Theory and Applications, vol. 37, no. 4, Aug. 1982.)

3. Neuman, F.; and Kreindler, E.: Minimum Fuel Turning Climbout and Descent Guidance of Transport Jets. NASA TM-84289, 1983.

4. Neuman, F.; and Kreindler, E.: Optimal Turning Climb-Out and Descent of Commercial Jet Aircraft. SAE Technical Paper 821468, Oct. 1982.

5. Erzberger, H.; and Lee, H. Q.: Terminal Area Guidance Algorithms for Automated Air Traffic Control. NASA TN D-6773, 1972.

6. Pecsvaradi, T.: Optimal Horizontal Guidance Law for Aircraft in the Terminal Area. IEEE Trans. Automat. Contr., vol. AC 17, no. 6, Dec. 1972.

7. McLean, J. D.: A New Algorithm for Horizontal Capture Trajectories. NASA TM-81186, 1980.

8. Kreindler, E.; and Neuman, F.: Minimum Fuel Horizontal Flightpaths in the Terminal Area. NASA TM-81313, 1981. (Also Journal of Guidance, Control, and Dynamics, vol. 5, no. 5, Sept.-Oct. 1982.)

9. Lee, H. Q.; and Neuman, F.: 4D Area Navigation System Description and Flight Test Results. NASA TN D-7874, 1975.

10. McLean, J. D.; and Erzberger, H.: Design of a Fuel-Efficient Guidance System for a STOL Aircraft. NASA TM-81256, 1981.

11. Erzberger, H.: Automation of On-Board Flightpath Management. NASA TM-84212, 1981. Also von Karman Lecture, 24th Israel Conference on Aviation and Astronautics, 1982.

12. Bryson, A. E.; and Ho, Y.: Applied Optimal Control. Blaisdel Publishing Co., Waltham, Mass., 1969.

13. Jacobson, D. H.; Lele, M. M.; and Speyer, J. L.: New Necessary Conditions of Optimality for Control Problems with State-Variable Inequality Constraints. J. Math. Anal. Appl., vol. 35, 1971, pp. 255-284.

14. Maurer, H.: On Optimal Control Problems with Bounded State Variables and Control Appearing Linearly. SIAM J. Control and Optimization, vol. 15, no. 3, May 1977, pp. 345-362.

15. Neuman, F.; and Erzberger, H.: Algorithm for Fuel Conservative Horizontal Capture Trajectories. NASA TM-81334, 1981.

16. Lee, H. Q.; and Erzberger, H.: Algorithm for Fixed-Range Optimal Trajectories. NASA TP-1565, 1980.

17. Jacob, H. G.: An Engineering Optimization Method with Application to STOL-Aircraft Approach and Landing Trajectories. NASA TN D-6978, 1972.

18. Lee, E. B.; and Markus, L.: Foundations of Optimal Control Theory. Wiley and Sons, New York, 1967.

1. Report No.	2. Government Accession No.	3. Recipient's Catalog No.
NASA TP-2326		

4. Title and Subtitle	5. Report Date
MINIMUM-FUEL, THREE-DIMENSIONAL FLIGHTPATH GUIDANCE OF TRANSPORT JETS	September 1984
	6. Performing Organization Code: ATP

7. Author(s)	8. Performing Organization Report No.
F. Neuman and E. Kreindler*	A-9533
	10. Work Unit No.: T-3309

9. Performing Organization Name and Address	11. Contract or Grant No.
NASA Ames Research Center Moffett Field, Calif. 94035	

12. Sponsoring Agency Name and Address	13. Type of Report and Period Covered
National Aeronautics and Space Administration Washington, D.C. 20546	Technical Paper
	14. Sponsoring Agency Code: 505-07-10

15. Supplementary Notes

*Department of E. E. Technion, Israel Institute of Technology, Haifa, Israel. Point of Contact: F. Neuman, Ames Research Center, M/S 210-9, Moffett Field, Calif. 94035. (415) 965-5451 or FTS 448-5451.

16. Abstract

This is a report on minimum-fuel, three-dimensional flightpaths for commercial jet aircraft. The theoretical development is divided into two sections. In both sections, the necessary conditions of optimal control, including singular arcs and state constraints, are used. One section treats the initial and final portions (below 10,000 ft) of long optimal flightpaths. Here all possible paths can be derived by generating fields of extremals. Another section treats the complete intermediate-length, three-dimensional terminal-area flightpaths. Here only representative sample flightpaths can be computed. The report provides sufficient detail to give the student of optimal control a complex example of a useful application of optimal control theory.

17. Key Words (Suggested by Author(s))	18. Distribution Statement
Optimal guidance Minimum fuel Transport jet aircraft	Unclassified - Unlimited Subject Category 08

19. Security Classif. (of this report)	20. Security Classif. (of this page)	21. No. of Pages	22. Price*
Unclassified	Unclassified	85	A05

*For sale by the National Technical Information Service, Springfield, Virginia 22161 NASA-Langley, 1984

National Aeronautics and
Space Administration

Washington, D.C.
20546

Official Business
Penalty for Private Use, $300

THIRD-CLASS BULK RATE

Postage and Fees Paid
National Aeronautics and
Space Administration
NASA-451

POSTMASTER: If Undeliverable (Section 158 Postal Manual) Do Not Return